MICROLENSING OF GRAVITATIONAL WAVES AS A NEW TOOL FOR ASTROPHYSICS

A Thesis

Submitted to the
Tata Institute of Fundamental Research, Mumbai
for the degree of Doctor of Philosophy

in Physics

by

UDDEEPTA DEKA

International Centre for Theoretical Sciences
Tata Institute of Fundamental Research
Mumbai

December, 2025

Uddeepta Deka: *Microlensing of gravitational waves as a new tool for astrophysics*

SUPERVISOR:
Parameswaran Ajith

Bengaluru, INDIA December 6, 2025

Dedicated to Ma

– my home, my guiding light
and the guru who shaped my deepest values.

DECLARATION

This thesis is a presentation of my original research work. Wherever contributions of others are involved, every effort is made to indicate this clearly, with due reference to the literature, and acknowledgement of collaborative research and discussions.

This work was done under the guidance of Professor Parameswaran Ajith, at the International Centre for Theoretical Sciences, Tata Institute of Fundamental Research, Bengaluru, INDIA.

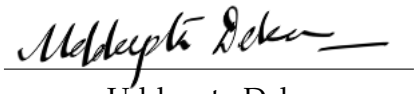

Uddeepta Deka

In my capacity as supervisor of the candidate's thesis, I certify that the above statements are true to the best of my knowledge.

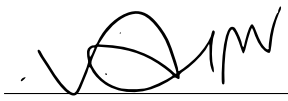

Parameswaran Ajith

Date: 6th Dec, 2025

Bengaluru, INDIA

Alone we can do so little,
together we can do so much.

— Helen Keller

ACKNOWLEDGEMENTS

To be honest, it is hard for me to imagine that my PhD journey is coming to an end. Looking back, I see myself navigating the highs and lows of becoming a researcher. There have been times when a lack of motivation set me back and I drifted off course. I must say that overcoming these would not have been possible without the incredible people who encouraged me and stood by me as unwavering pillars of support. And then there are those who showed immense trust in me and filled me with positivity whenever I needed most. Along the way, not only did I learn to conduct scientific research but I grew immensely on a personal level. I am privileged to write these few words of acknowledgement for everyone who laughed with me, made me realize my potential and reminded me why I started this journey in the first place.

There were moments when my own self-doubt screamed the loudest, but having my advisor (and colleague), Ajith, patiently walk me through complicated ideas made me feel like I actually belonged here. I am deeply honored to have worked with him. His ability for boiling down complex concepts into their simplest possible form inspired me to sharpen my own clarity of thought. Under his mentorship, I learned to set clear priorities, manage my time efficiently, and always start with back-of-the-envelope calculations before spending time and resources into a project. By trusting me to lead independent projects, he helped me grow into a confident researcher. Even his meticulous attention to detail, including plot colors and font choices, had shown me how thoughtful presentation can communicate science more effectively. I am also grateful to Ajith for providing crucial financial support whenever I needed it throughout my PhD.

Besides Ajith, two collaborators (and mentors) who have left a lasting impact on me are Shasvath and Arif. Shasvath's ability to put abstract ideas into concrete research projects, while Arif's skill for writing robust and elegant codes have inspired me. More than anything, I thank both of them for boosting my confidence, especially during the later part of my PhD.

I have come to realize that meaningful growth happens when you are in the right environment, surrounded by the right people – and the Astrophysics and Relativity group at ICTS gave me just that. It was a vibrant community of bright minds who encouraged me to challenge myself while also fostering a relaxed and supportive atmosphere that made the journey both fulfilling and fun. My understanding of gravitational waves developed largely through the many engaging discussions within the group – whether during Journal Clubs, paper discussions, seminars or group meetings. What made these interactions even more special was the presence of Bala, who often referred to himself as "the ringmaster" of the group. Seeing someone of his stature actively participate and offer thoughtful feedback was

truly inspiring. Being part of the group during his time is something I will always consider a privilege.

I am grateful to Prof. Rajaram Nityananda for his invaluable inputs on my projects. His years of experience in astronomy research brought in new perspectives into my work. My occasional conversations with Prayush on building better and faster waveforms, current challenges in waveform modeling and using better coding practices were always insightful. I would like to extend my gratitude to my fellow colleagues and postdocs in the group – Souvik, Mukesh, Aditya, Ankur, Akash, Alorika, Priyanka, Neha, Koustav, Prasad, Rajes, Anuj and Samanwaya – for all the stimulating discussions, collaborations, and countless memorable moments we shared. I have also been inspired in many ways by the former members of the group, including Soummyadip, Aditya V., Srashti, Krishnendu, Ajit Mehta, Akash Mishra, Kanhaiya, Vaishak and Shalabh. I truly enjoyed being part of this group and will always carry these experiences with me.

A heartfelt thanks to my collaborators – Apratim, Sumanta, Gopal and Soham – for their fresh ideas and the enthusiasm they brought into every discussion. Working with them was intellectually rewarding. Apratim played a pivotal role in mentoring me during my initial days at ICTS, and I am thankful to him for taking out time to make me understand the basics of microlensing. From Sumanta, I learned the value of analytical rigor. Discussions with Gopal and Soham brought clarity and helped refine my thinking.

I remember the countless times I sought help from Anup and Omkar – whether it was struggling with equations or getting stuck in Mathematica. I am deeply grateful to Mukesh, Souvik, Srashti, Soummyadip and Ankur for clarifying my never-ending doubts about data analysis and helping me solve computational challenges. Their willingness to help and assist, even during their busiest hours, truly meant a lot.

During my academic journey, I have been fortunate to be taught by some of the most exceptional teachers. Their courses helped immensely in preparing me for graduate school. I am especially grateful to Prof. Patrick Das Gupta for his courses on astrophysics and General Relativity, as well as for guiding my master's thesis project. I also want to thank Prof. Biman Nath for his introductory course on astrophysics, which laid a strong foundation for my further studies. I had fun attending (and later tutoring) the advanced Electrodynamics course by Loga (Loganayagam R.), the course on gravitational waves by Ajith and Bala, and Samriddhi's course on turbulence. I am also thankful to the course instructors at various ICTS schools, especially the gravitational wave summer schools, who gave me the chance to explore niche topics in depth while working as a teaching assistant.

I took my first formal steps into astrophysics under the guidance of Dr Sushan Konar, who introduced me to the world of compact objects. The work I did with her played a key role in sparking my interest in compact binaries and gravitational waves, for which I am very grateful. Before that, my decision to pursue physics as a career was shaped by my school teachers, especially Ranen sir and Riju ma'am. Virendra sir and Subhasish Mallick sir helped me build a strong foundation in mathematics – something that has been essential throughout my journey in physics. Nirmali ma'am's course on C++ laid the groundwork for my interest in scientific computing and has been central to much of the work I do today. I remain deeply thankful to

all my school teachers for their patience, encouragement, and for shaping me into someone who can approach unfamiliar problems with confidence.

I joined ICTS along with a bunch of equally enthusiastic people who, over time, became close friends. I have enjoyed both the academic and non-academic activities with them, which kept me sane during tough times. I will always cherish fond memories of playing badminton with Anup and Mukesh, my all-time companions at the sports complex. Competing with them and playing alongside them was an unforgettable experience. Souvik, with whom I shared the major time in the Narmada (N12) apartment, was always there to listen to my rants. His love for biryani was only matched by his passion for football – which eventually got me interested into the game too. Weekend music sessions and jamming with Tuneer and Omkar were something I always looked forward to. I got the courage to go for my first solo motorbike trip thanks to the long rides I took with Bhanu. Priyadarshi's taste in books often reignited my love for reading. Mahaveer's commitment to fitness encouraged me to take up martial arts classes and join several treks. Ankush and Harshit were my regular challengers in badminton and arcade games. I recollect the cycle rides with Shivam during the initial days at ICTS, which served as a great motivation for me to take up cycling as a hobby. I am extremely grateful to each one of them for their friendship, support and making this journey truly special. They have been the best batchmates I could have asked for.

Madhulika's push for conducting sports events and Loga's encouragement towards cultural activities was always a breath of fresh air during hectic times. Their efforts reminded me to take life a little less seriously and enjoy the moments in between work. I learned a great deal about movies through the movie club we started together with Nirnoy, Godwin and Tamoghna. I am grateful to Chandru, Santhiya, Ankur and Vinay for keeping the astroclub active – the night sky viewing sessions and outreach events brought a much-needed sense of refreshment and wonder. I am also thankful for the informal music circle we had, especially Tuneer, Soumi di, Basudeb, Debarshee da, Omkar, Alorika, Koustav, Mrinal, Neha, Prasad and Naveen. I truly enjoyed being part of our small band with Shubhadeep, Naveen, Anuj, Mayank and Izumi. It was one of the highlights of my time here.

Over the years, I have had the pleasure of sharing my office space with many wonderful colleagues – Rahul, Sparsh, Sahil, Vinay, Godwin, Mayank, Irshad and Avi. From having impromptu discussions ranging from physics to conversations about life in general, I genuinely appreciated the sense of camaraderie and ease we shared. I also had a great time engaging with colleagues from other research areas – Sharath, Manisha di, Joydeep, Santhosh, Prashant, Arnab, Basudeb, Saumav, Jitendra, Saikat and Saurav. These interactions not only helped broaden my understanding of physics but also enriched my experience here.

I cannot thank Prakhar enough for being my safe space – not just throughout this PhD journey, but long before it even began. Atulesh and Vineet had always been there whenever it mattered most, and I'm truly thankful for their steady friendship. I thank Sarita for the much needed support during my entrance exams. Shashank was the first to introduce me to ICTS, and I'm glad our friendship endured over the years. I am thankful to Anjali for being my companion in most of my outdoor adventures including hiking and biking. I had really

enjoyed planning and going for road trips with Divyajyoti, evening tea sessions with Sarada, and the incredible food cooked by Sumi, which made everything taste and feel like home.

None of this would have been possible without the quiet strength, relentless belief, and boundless love of my mother. Ma, thank you for holding me up when I was falling apart, for your faith, when mine wavered, and for being the reason I could keep going.

At the heart of an institution's smooth functioning lies the hard work and dedication of not just the academic staff but also the non-academic staff. As Ajith once said, " what sets ICTS apart from other institutions is its highly qualified and dedicated administrative and technical staff" – a sentiment I completely agree with. Whether it was processing reimbursements or timely disbursal of fellowships, the establishment team was always supportive. The IT team was a huge help too – from providing me with a laptop, repairing it whenever needed, to maintaining the extensive computing systems I rely on. I am also thankful to the academic team for their behind-the-scenes work in organizing high-quality academic seminars, and managing my coursework and academic formalities smoothly. My interest in outreach grew thanks to the continuous efforts of the outreach team and the programs committee. The housing team had made my stay here very comfortable by taking care of all the residential facilities. I have spent countless hours in the library exploring its fascinating collection of science, fiction and non-fiction books. I thank Devanath for maintaining the library and making it such a comforting space. I am truly grateful to the housekeeping, cafeteria, sports, medical, transport, security, maintenance, engineering, and gardening staff for creating such a welcoming and efficient work environment at ICTS.

I would like to thank Prof. Rajesh Gopakumar, Centre Director of ICTS, for his inspiring leadership. His vision and commitment to fostering a vibrant academic environment have made ICTS a truly special place to learn and grow. I am grateful for the opportunities and atmosphere he has helped create, which made my time here both enriching and memorable.

My academic visits have been valuable in helping me engage with researchers and exchange ideas. In this regard, I thank Prof. B.S. Sathyaprakash for hosting me at the Penn State University and Dr. Archisman Ghosh for hosting me at the Ghent University. I would also like to thank the Albert Einstein Institute at Potsdam for the opportunity to visit and interact with their research groups. I am thankful to Ajith and Prof. Rajesh Gopakumar for supporting these visits through travel grants.

I extend my sincere gratitude to my Thesis Monitoring Committee members – Prof. Tejaswi Venumadhav, Prof. Girish Kulkarni and Prof. Vijaykumar Krishnamurthy – for their invaluable insights and constructive feedback throughout my PhD.

Last but not the least, I am deeply grateful to the people of India for supporting the science that we do through public funding. It is their trust in higher education and their belief in the value of human curiosity that makes research like ours possible. I hope to give back by contributing meaningfully to both the scientific community and society at large. Thank you!

LIST OF PUBLICATIONS

Works related to this thesis:

[1] Uddeepta Deka, Sumanta Chakraborty, Shasvath J. Kapadia, Md Arif Shaikh, and Parameswaran Ajith. "Probing the charge of compact objects with gravitational microlensing of gravitational waves." In: *Phys. Rev. D* 111.6 (2025), p. 064028. DOI: 10.1103/PhysRevD.111.064028. arXiv: 2401.06553 [gr-qc].

[2] Uddeepta Deka, Apratim Ganguly, Soham Bhattacharya, and Parameswaran Ajith. "Investigating the efficacy of microlensing searches using point mass lens models." In preparation. 2025.

[3] Uddeepta Deka, Gopalkrishna Prabhu, Md Arif Shaikh, Shasvath J. Kapadia, Vijay Varma, and Scott E. Field. "Surrogate modeling of gravitational waves microlensed by spherically symmetric potentials." In: *Phys. Rev. D* 111.10 (2025), p. 104042. DOI: 10.1103/PhysRevD.111.104042. arXiv: 2501.02974 [gr-qc].

ABSTRACT

The observation of gravitational lensing of light and the detection of gravitational waves (GWs) stand as remarkable confirmations of Einstein's theory of General Relativity (GR), both of which provide powerful tools for probing the universe. Recent GW observations by LIGO and Virgo have probed the astrophysical properties of black holes and neutron stars, enabled stringent tests of GR in the strong-field regime and contributed to the independent measurement of the cosmological parameters, among others. With the advent of the next generation (XG) GW detectors, $\sim 10^5 - 10^6$ compact binary coalescence (CBC) events will be detected per year, a considerable number of which will be lensed.

Unlike the gravitational lensing of electromagnetic (EM) waves, lensing of GWs can exhibit lensing effects in the wave optics regime, where their wavelengths are comparable to the size of the lens. This phenomenon, known as GW *microlensing*, leads to characteristic frequency-dependent modulations in the observed waveform. Due to their much shorter wavelengths, such wave optics effects are virtually unobservable in EM waves.

Microlensing of GWs in the LVK frequency band occurs for lenses whose masses lie in the range $\sim 10^2 - 10^4 M_\odot$. Potential lenses in this mass window include (but are not limited to) intermediate-mass black holes (IMBHs) and other exotic compact objects such as primordial black holes, boson stars, and gravastars. Such wave optics effects enable the exploration of lensing effects at scales beyond the reach of optical or radio observations. The anticipated observations of gravitationally lensed GWs in the future observation runs will open up a plethora of unexplored avenues in astrophysics, cosmology, and fundamental physics.

In this thesis, we explore various aspects of developing GW microlensing observations as an astrophysical tool. We begin in Chapter 1 with an overview of GWs – their sources, detectors, and the broad scientific insights they offer. Chapter 2 introduces gravitational lensing. In this chapter, we discuss the theory behind the propagation of GWs as perturbations on a curved spacetime background, and highlight the physical regimes of wave-optics and geometric-optics. We also introduce the various lens models that are relevant to the microlensing scenarios considered in the later chapters. In Chapter 3, we explore the possibility of constraining the effective charge of compact objects using GW microlensing observations. In addition to the EM charge, this effective charge can arise from various alternative theories of gravity. Chapter 4 investigates the efficacy of the current microlensing searches that idealize the compact object lens as an isolated point mass. This is motivated by the expectation that such microlenses are likely to be a part of the lensing potential of their host galaxy, which will modify the lensing effects. Chapter 5 focuses on the development of efficient methods to compute microlensed GW waveforms using surrogate modeling techniques. These models generate fast and accurate microlensed waveforms, making them viable for parameter estimation. Finally, Chapter 6 summarizes the findings of this thesis and discusses future directions for research in this field.

CONTENTS

LIST OF FIGURES

LIST OF TABLES

1

GRAVITATIONAL WAVES

Gravitational waves (GWs) are disturbances in spacetime that propagate at the speed of light. The existence of GWs was first predicted by Einstein in 1916 [127] as a consequence of his theory of General Relativity (GR). The landmark direct detection [3] of GWs by the Advanced Laser Interferometer Gravitational-Wave Observatory (LIGO) [2] marked the beginning of GW astronomy, enabling the observation and study of astrophysical systems that were previously beyond our reach. In this chapter, we provide an overview of the theoretical foundations of GWs, describe their sources and the detectors. We also discuss the various scientific insights enabled by their observation.

The first indirect evidence for the existence of GWs came from the Hulse-Taylor binary star system (PSR 1913+16), whose observed orbital decay matched GR's predictions for energy loss via gravitational radiation [281, 305].

1.1 LINEARIZED THEORY OF GRAVITY

In regimes where gravitational fields are weak and typical velocities of matter sources are much smaller than the speed of light, Einstein's field equations can be linearized around flat spacetime. This approximation, known as the *linearized theory of gravity*, provides a powerful framework for understanding gravitational waves as small perturbations propagating on a Minkowski background. We begin by expressing the spacetime metric as

$$g_{\mu\nu} = \eta_{\mu\nu} + h_{\mu\nu}, \quad |h_{\mu\nu}| \ll 1 \,, \tag{1.1}$$

We work in units where $G = c = 1/(4\pi\epsilon_0) = 1$. Greek indices $(\mu, \nu, \dots)$ denote spacetime components, and Latin indices $(i, j, \dots)$ refer to spatial components. Throughout this thesis, we use the mostly-positive metric signature: $\eta_{\mu\nu} = \mathrm{diag}(-1, +1, +1, +1)$.

where $\eta_{\mu\nu}$ is the Minkowski metric and $h_{\mu\nu}$ represents the perturbation. By retaining only terms linear in $h_{\mu\nu}$, the Einstein equations simplify significantly, yielding a set of wave-like equations for the metric perturbations in vacuum.

Imposing the Lorenz gauge condition

$$\partial^\nu \bar{h}_{\mu\nu} = 0 \,, \tag{1.2}$$

where ∂^ν denotes partial derivatives with respect to the coordinate x^ν, while $\bar{h}_{\mu\nu}$ is the trace-reversed perturbation defined as

$$\bar{h}_{\mu\nu} = h_{\mu\nu} - \frac{1}{2}\eta_{\mu\nu}h, \quad h = \eta^{\alpha\beta}h_{\alpha\beta} \,, \tag{1.3}$$

the linearized Einstein equations in vacuum reduce to the familiar wave equations[1]

[1] *See Misner, Thorne, and Wheeler [226] for a detailed derivation.*

$$\Box \bar{h}_{\mu\nu} = 0 \,, \tag{1.4}$$

where $\Box \equiv -\partial_t^2 + \nabla^2$ is the flat spacetime d'Alembertian operator. The solutions to Eq. (1.4) are GWs which can be written as superposition of plane waves

$$\bar{h}_{\mu\nu}(t, \mathbf{x}) = \mathrm{Re} \int d^3k \, A_{\mu\nu}(\mathbf{k}) e^{i(\mathbf{k}\cdot\mathbf{x} - \omega t)} \,, \tag{1.5}$$

where the four-vector $k^\mu = (\omega, \mathbf{k})$, ω is the wave frequency and $\mathbf{k}$ is the wave vector with $|\mathbf{k}| = \omega$. The amplitude $A_{\mu\nu}(\mathbf{k})$ is a symmetric tensor that encodes the polarization states of the GW and is subject to the constraint $k^\nu A_{\mu\nu} = 0$, which follows from the Lorenz gauge condition (Eq. (1.2)).

In globally vacuum spacetimes, the Lorenz gauge does not fix the gauge completely.[2] This residual gauge freedom can be used to further impose the conditions

[2] *See Chapter 1 of Maggiore [208] for details.*

$$h_{00} = h_{0i} = 0 \text{ and } h^i_i = 0 \tag{1.6}$$

to completely fix all the local gauge freedom. The resultant metric perturbations contain only the physical degrees of freedom. For plane waves propagating along the direction $\hat{\mathbf{n}} \equiv \mathbf{k}/|\mathbf{k}|$, from Eqs. (1.2) and (1.6), we have

$$\partial^j h^{\mathrm{TT}}_{ij} = 0 \implies \hat{n}^j h^{\mathrm{TT}}_{ij} = 0 \,. \tag{1.7}$$

In the TT gauge, perturbations are denoted as $h^{TT}_{\mu\nu}$, and satisfy $\bar{h}^{TT}_{\mu\nu} = h^{TT}_{\mu\nu}$.

This implies that the non-zero components of h^{TT}_{ij} are in the plane transverse to $\hat{\mathbf{n}}$. Eqs. (1.6) and (1.7) constitute the *transverse-traceless* (TT) gauge conditions. While Eq. (1.6) imposes five constraints on the perturbed metric, Eq. (1.7) introduces three additional constraints, reducing the number of independent components of $h_{\mu\nu}$ from ten to two - the two physical polarization modes of GWs. Consider a monochromatic GW propagating in the z-direction, the non-zero components of the metric perturbation can be expressed as

$$h^{\mathrm{TT}}_{ab}(t, z) = \begin{pmatrix} h_+ & h_\times \\ h_\times & -h_+ \end{pmatrix}_{ab} \sin\left[\omega(t - z)\right] \,, \tag{1.8}$$

where $a, b = 1, 2$ are indices denoting the transverse (x, y) plane; h_+ and $h_\times$ are the two independent polarization states of the GW, known as the *plus* and *cross* polarizations, respectively. These two polarizations can be visualized as stretching and squeezing of a ring of test masses (maroon dots) in the transverse plane, as shown in Fig. 1.1. The plus polarization (h_+) stretches and compresses these particles along the axes, while the cross polarization ($h_\times$) induces distortions along the diagonal directions.

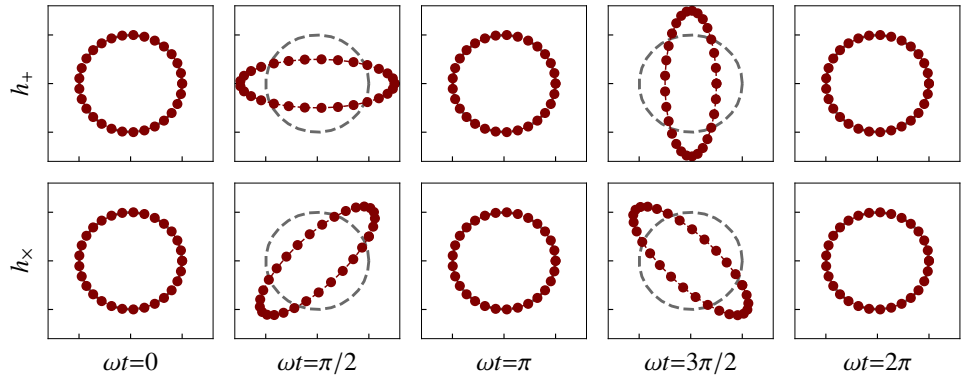

Figure 1.1: *Deformation of a ring of test masses (maroon dots) by a passing GW, showing the effect of two polarizations: h_+ (top panel) and $h_\times$ (bottom panel).*

1.2 GENERATION OF GRAVITATIONAL WAVES IN LINEARIZED THEORY

Consider a source of GWs whose gravitational field is sufficiently weak such that the background spacetime can be approximated as flat. In this case, the linearized theory of gravity (Sec. 1.1) remains valid, and the presence of matter can be included through a source term on the right hand side of Eq. (1.4) as

$$\Box \bar{h}_{\mu\nu} = -16\pi T_{\mu\nu} \,, \tag{1.9}$$

where $T_{\mu\nu}$ is the stress-energy tensor which describes the matter and energy content of the source. Note that the Lorenz gauge condition (Eq. (1.2)) is still valid. In addition, the flat-space energy-momentum conservation law guarantees

$$\partial^\nu T_{\mu\nu} = 0 \,. \tag{1.10}$$

Eq. (1.9) can be solved using a Green's function approach. The Green's function for the d'Alembertian operator in flat spacetime is given by[3]

$$G(t, \mathbf{x}; t', \mathbf{x}') = -\frac{\delta\left(t' - [t - |\mathbf{x} - \mathbf{x}'|]\right)}{4\pi|\mathbf{x} - \mathbf{x}'|} \,. \tag{1.11}$$

[3] *See, e.g., Jackson [178]*

It represents the field at point $(t, \mathbf{x})$ due to a unit point source located at $\mathbf{x}'$ and active at the retarded time $t' = t - |\mathbf{x} - \mathbf{x}'|$.

With this Green's function, the solution to Eq. (1.9) can be expressed as

$$\begin{aligned} &\bar{h}_{\mu\nu}(t, \mathbf{x}) = -16\pi \int d^4x'\, G(t, \mathbf{x}; t', \mathbf{x}')\, T_{\mu\nu}(t', \mathbf{x}') \\ \implies &\bar{h}_{\mu\nu}(t, \mathbf{x}) = 4 \int d^3x' \, \frac{T_{\mu\nu}(t - |\mathbf{x} - \mathbf{x}'|, \mathbf{x}')}{|\mathbf{x} - \mathbf{x}'|} \,. \end{aligned} \tag{1.12}$$

The metric perturbation $\bar{h}_{\mu\nu}$ includes gauge-dependent, radiative and non-radiative components. While a full TT gauge cannot generally be imposed, the perturbation can be uniquely decomposed. Only the radiative part satisfies

the TT gauge conditions and represents GWs, while the non-TT parts are governed by Poisson equations and are non-radiative.[4]

[4] See Flanagan and Hughes [144] for a discussion.

Given a plane wave solution $h_{\mu\nu}$ (or equivalently $\bar{h}_{\mu\nu}$) in the Lorenz gauge propagating along $\hat{\mathbf{n}}$, the corresponding TT components outside the source can be extracted with the help of the tensor

$$\Lambda_{ij,kl}(\hat{\mathbf{n}}) = P_{ik}P_{jl} - \frac{1}{2}P_{ij}P_{kl} \,, \tag{1.13}$$

where $P_{ij}(\hat{\mathbf{n}}) \equiv \delta_{ij} - \hat{n}_i\hat{n}_j$ is the projection operator onto the plane orthogonal to $\hat{\mathbf{n}}$. The TT part of the metric perturbation is then given by

$$h^{\rm TT}_{ij}(t,\mathbf{x}) = \Lambda_{ij,kl}(\hat{\mathbf{n}})h_{kl}(t,\mathbf{x}) = \Lambda_{ij,kl}(\hat{\mathbf{n}})\bar{h}_{kl}(t,\mathbf{x}) \,. \tag{1.14}$$

Since we are interested in $h^{\rm TT}_{ij}$ at large distances r from the source (i.e., in the wave zone where detectors are located), we approximate $|\mathbf{x}-\mathbf{x}'| \approx r$. Furthermore, if the internal motions of the source are non-relativistic, we can use the approximation $T_{\mu\nu}(t-|\mathbf{x}-\mathbf{x}'|,\mathbf{x}') \approx T_{\mu\nu}(t-r,\mathbf{x}')$. Applying Eq. (1.14) to Eq. (1.12) along with the simplifications above, we can write the TT components of the metric perturbation as

$$h^{\rm TT}_{ij}(t,\mathbf{x}) = \frac{4}{r}\Lambda_{ij,kl}(\hat{\mathbf{n}})\int d^3x'\, T_{kl}(t-r,\mathbf{x}') \,, \tag{1.15}$$

which corresponds to the leading-order term in a multipole expansion of the radiation field. For slow moving sources, $T^{00} \approx \rho$, the mass density. Using Eq. (1.10) and assuming the source to be spatially localized, we find

$$\int d^3x'\, T_{ij} = \frac{1}{2}\frac{d^2 I_{ij}}{dt^2} \,, \tag{1.16}$$

where the second mass moment tensor I_{ij} is defined as

$$I_{ij} = \int d^3x'\, x'_i x'_j \rho(t,\mathbf{x}') \,. \tag{1.17}$$

Since only the traceless part of I_{ij} contributes to Eq. (1.15), we define the *quadrupole moment* tensor:

$$\mathcal{I}_{ij} = I_{ij} - \frac{1}{3}\delta_{ij}I^k_k \,. \tag{1.18}$$

Combining Eqs. (1.15), (1.16) and (1.18), the leading-order TT metric perturbation is given by

$$h^{\rm TT}_{ij}(t,\mathbf{x}) = \frac{2G}{c^4 r}\Lambda_{ij,kl}(\hat{\mathbf{n}})\ddot{\mathcal{I}}_{kl}(t-r/c) \,, \tag{1.19}$$

where $\ddot{\mathcal{I}}_{kl}$ is the second time derivative of the quadrupole moment tensor and we have reinstated G and c for physical clarity. This expression shows

that GWs are generated by the acceleration of mass distributions, and their strength decreases with distance as $1/r$. The GW energy flux — the energy dE crossing an area element dA on a sphere of radius r during a time interval dt — is given by[5]

$$\frac{dE}{dt\,dA} = -\frac{c^3}{32\pi G}\langle \dot{h}^{\mathrm{TT}}_{ij}\dot{h}^{ij}_{\mathrm{TT}}\rangle = -\frac{c^3}{16\pi G}\langle \dot{h}^2_+ + \dot{h}^2_\times\rangle\ , \tag{1.20}$$

where $\langle\cdots\rangle$ represents a temporal average over several characteristic periods of the GW. The GW luminosity in the quadrupole approximation is then[6]

$$L_{\mathrm{GW}} \equiv -\frac{dE}{dt} = \frac{G}{5c^5}\langle \dddot{\mathcal{I}}_{ij}\dddot{\mathcal{I}}^{ij}\rangle\ , \tag{1.21}$$

where the time derivatives are evaluated at the retarted time $t - r/c$.

The quadrupole approximation is valid for weak-field, slow-motion systems where the typical internal velocity $v \ll c$. For highly relativistic or strongly gravitating sources, this approximation breaks down. Relativistic corrections due to large v/c can be systematically incorporated using the *post-Newtonian* (PN) formalism – an expansion in powers of v/c. Meanwhile, strong-field effects arising from nonlinearities in the gravitational interaction (i.e., large G) are addressed by the *post-Minkowskian* (PM) formalism – an expansion in powers of G.[7]

[5] *See Chapters 1 and 3 of Maggiore [208] for details.*

[6] *This formula was first derived by Einstein [128] in 1918 and is often referred to as the quadrupole formula.*

[7] *Refer to Blanchet [78] for a comprehensive review of the state-of-the-art post-Newtonian calculations.*

1.3 SOURCES OF GRAVITATIONAL WAVES

As discussed in Sec. 1.2, GWs are generated by time-varying quadrupole moments of mass distributions. However, terrestrial sources are far too weak to be detectable. Detectable GWs typically originate from astrophysical systems involving massive, compact objects undergoing rapid, asymmetric accelerations. The characteristic frequency of such waves is determined by the system's dynamical timescale.

	TRANSIENT	PERSISTENT
MODELED	Compact binary coalescence	Continuous
UNMODELED	Burst	Stochastic

Table 1.1: *Categories of possible GW sources.*

Table 1.1 summarizes the broad categories of GW sources based on their duration and whether their waveforms can be reliably modeled. In the following subsections, we discuss each of these sources in more detail.

1.3.1 *Compact binary coalescences*

This is the class of GW signals that has been routinely detected by the current ground-based observatories. Compact binary coalescences (CBCs) involve two compact objects, such as black holes (BBH), neutron stars (BNS), or a combination thereof, in a close binary system that loses energy via GW emission and eventually merges.

The *inspiral* phase, during which the orbit shrinks gradually due to radiation losses, is accurately modeled using the PN formalism. During this stage, both the amplitude and frequency of the waveform increase as the two bodies spiral closer. The system evolves through a sequence of quasi-circular orbits until the binary either reaches the innermost stable circular orbit (ISCO) or the two bodies make contact. At this point, the binary enters the *merger* phase, forming a single, highly distorted remnant. This phase marks the peak of GW emission and is modeled using full numerical relativity (NR), which solves Einstein's equations without approximations[8] . The final *ringdown* phase describes the relaxation of the remnant - typically a Kerr black hole - via damped oscillations known as quasi-normal modes (QNMs), radiating away residual distortions[9] . The spectrum of these QNMs can be computed using black hole perturbation theory (BHPT)[10] . In the case of neutron star mergers, however, the post-merger dynamics are far more complex and sensitive to the underlying microphysics (e.g. the equation of state of dense nuclear matter). Accurately modeling this phase requires detailed numerical simulations that incorporate relativistic hydrodynamics and nuclear physics. The top panel of Fig. 1.2 shows these phases of the binary coalescence process for a BBH.

[8] *For an in-depth review of NR methods applied to compact binary systems, see Baumgarte and Shapiro [68].*

[9] *Refer to Kokkotas and Schmidt [192] for a comprehensive overview of the theory of QNMs.*

[10] *Vishveshwara [299] in 1970 demonstrated that GWs scattered off a black hole have characteristic waveforms, which led to the discovery of QNMs.*

We now use results from Sec. 1.2 to estimate the GW strain amplitude from a compact binary system in the quadrupole approximation. Consider two masses m_1 and m_2 in a quasi-circular orbit located at a distance r from the observer. At Newtonian order, the orbital angular frequency Ω is given by Kepler's third law

$$\Omega = \sqrt{\frac{GM}{R^3}} \,, \tag{1.22}$$

where $M \equiv m_1 + m_2$ is the total mass of the system and R is the orbital radius. For this system, assuming that the motion is in the $x-y$ plane, the non-vanishing components of the quadrupole moment tensor evaluated at the retarted time $t_{\rm ret} \equiv t - r/c$ are

$$\mathcal{I}_{11} = \frac{1}{2}\mu R^2 \left[1 + \cos(2\Omega t_{\rm ret})\right] , \tag{1.23a}$$

$$\mathcal{I}_{22} = \frac{1}{2}\mu R^2 \left[1 - \cos(2\Omega t_{\rm ret})\right] , \text{ and} \tag{1.23b}$$

$$\mathcal{I}_{12} = \frac{1}{2}\mu R^2 \sin(2\Omega t_{\rm ret}) \,, \tag{1.23c}$$

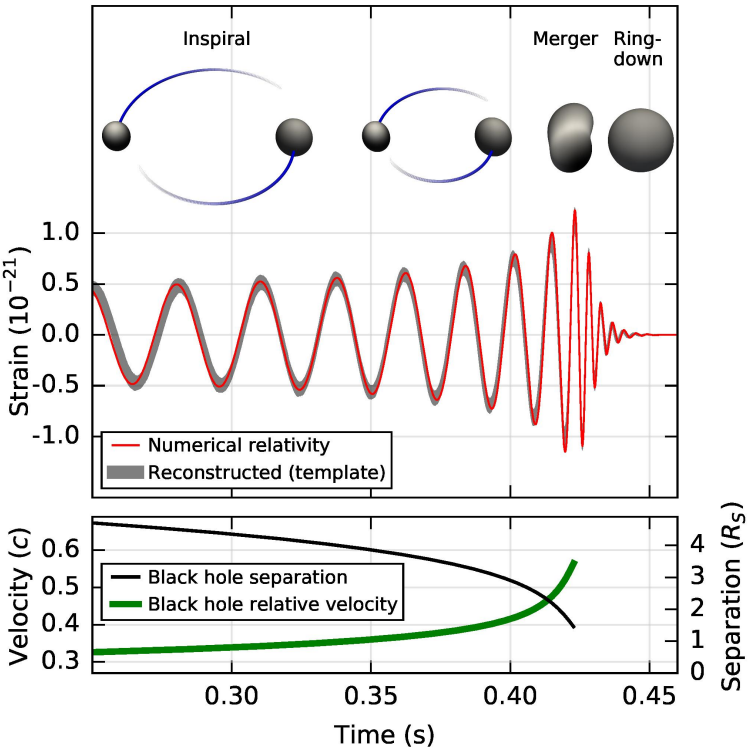

Figure 1.2: *Top: Time evolution of a binary black hole (BBH) coalescence illustrating the inspiral, merger and ringdown phases. Middle: simulated GW strain amplitude from GW150914 as predicted by numerical relativity (red) and reconstructed from observed data using a waveform template (gray). Bottom: relative velocity (in units of c) and separation (in Schwarzschild radii of the total mass) of the black holes over time. Credits: Abbott et al. [3]*

where $\mu \equiv m_1 m_2 / M$ is the reduced mass of the system. Let the normal of the orbital plane be inclined at an angle ι with respect to the line of sight. The GW strain predicted by the quadrupole formula (Eq. (1.19)), is then given by[11]

$$h_{ij}^{\mathrm{TT}} = h \begin{pmatrix} \frac{1+\cos^2\iota}{2}\cos(2\Omega t_{\mathrm{ret}}) & \cos\iota\,\sin(2\Omega t_{\mathrm{ret}}) & 0 \\ \cos\iota\,\sin(2\Omega t_{\mathrm{ret}}) & -\frac{1+\cos^2\iota}{2}\cos(2\Omega t_{\mathrm{ret}}) & 0 \\ 0 & 0 & 0 \end{pmatrix}, \tag{1.24}$$

with the amplitude

$$h = \frac{4G\mu R^2\Omega^2}{c^4 r} = \frac{4G^{5/3}\mu M^{2/3}\Omega^{2/3}}{c^4 r}\,. \tag{1.25}$$

Here, G and c are explicitly included to emphasize that h is dimensionless. From Eq. (1.24) we see that the GW frequency is twice the orbital frequency in the Newtonian order, that is, $f = 2f_{\mathrm{orb}} \equiv \Omega/\pi$. For a binary with $m_1 = m_2 = 30M_\odot$ at a distance of 400 Mpc, the strain amplitude at the peak orbital frequency of 100 Hz is $h \approx 10^{-21}$. Such binaries are detectable by the current ground-based detectors. Similarly, supermassive black hole (SMBH) binaries (with component masses $\sim 10^7 M_\odot$ each) with orbital periods of a few hours at ~ 1 Gpc distance can be detected by the planned space-based Laser Interferometer Space Antenna (LISA). The middle panel of Fig. 1.2 displays the strain amplitude of GW150914, the first detected BBH event. The red curve

[11] *Refer to Chapter 3 of Creighton and Anderson [114] for a detailed derivation.*

shows the numerical relativity prediction, while the gray curve represents the signal reconstructed from observed data using a waveform template.

The GW luminosity can be computed from Eq. (1.21) by substituting the quadrupole moment tensor components given in Eq. (1.23), yielding[12]

$$L_{\rm GW} = \frac{32}{5}\frac{G}{c^5}\mu^2 R^4 \Omega^6 = \frac{32}{5}\frac{c^5}{G}\eta^2 \left(\frac{v}{c}\right)^{10} , \tag{1.26}$$

where $\eta \equiv \mu/M$ is the symmetric mass ratio and $v \equiv R\Omega$ is the characteristic orbital velocity. The energy carried away by GWs results in a loss of orbital energy, $E_{\rm orb} = \mu v^2/2$, leading to a gradual inspiral of the binary[13] . Equating the GW luminosity to the rate of change of orbital energy gives the evolution of the orbital velocity as

$$\frac{d}{dt}\left(\frac{v}{c}\right) = \frac{32}{5}\frac{\eta c^3}{GM}\left(\frac{v}{c}\right)^9 . \tag{1.27}$$

Using the Newtonian relation $v = \sqrt{GM/R}$, we can also express the evolution of the orbital separation R in terms of the dimensionless ratio R/R_S, where $R_S \equiv GM/c^2$ is the Schwarzschild radius of the total mass M

$$\frac{d}{dt}\left(\frac{R}{R_S}\right) = -\frac{64}{5}\left(\frac{G\mu}{R_S^2 c}\right)\left(\frac{R}{R_S}\right)^{-3} . \tag{1.28}$$

The evolution of the orbital velocity and separation as the binary spirals in and eventually merges is shown in the bottom panel of Fig. 1.2. Moreover, Eq. (1.27) can be recast in terms of the GW frequency using the relation $v = (\pi G M f)^{1/3}$ leading to the frequency evolution equation

$$\frac{df}{dt} = \frac{96}{5}\pi^{8/3}\left(\frac{G\mathcal{M}_c}{c^3}\right)^{5/3} f^{11/3} , \tag{1.29}$$

where $\mathcal{M}_c \equiv \eta^{3/5} M$ is the chirp mass of the binary system. The frequency increases rapidly as the binary approaches merger, leading to the characteristic chirp signal. Note that with the inclusion of higher PN corrections, the evolution equations become more complex, but the qualitative features of the inspiral remain unchanged.

The detection and analysis of CBC signals require accurate modeling of the full *inspiral-merger-ringdown* (IMR) waveform. With increasing detector sensitivity, minimizing systematic biases from waveform inaccuracies becomes essential. Modern waveform models, such as those in the *phenomenological* (Phenom) [44] and *effective-one-body* (EOB) [85] families, use semi-analytical techniques that combine inputs from PN theory, NR, and BHPT to describe the entire coalescence. In parallel, data-driven *surrogate* models [141] are built by interpolating over a set of NR waveforms and offer highly accurate and

[12] *The corresponding expression for elliptic Keplerian orbits is due to Peters and Mathews [248].*

[13] *We assume that the energy radiated per orbit is small compared to the total orbital energy E_{orb}, allowing the binary to be treated as evolving through a sequence of approximately Keplerian orbits.*

computationally efficient waveform generation for specific regions of the parameter space.

Throughout this thesis, we will be concerned with CBC signals only.

1.3.2 *Continuous waves*

Continuous gravitational waves (CWs) are long-lasting, nearly monochromatic signals. Unlike the transient CBC signals, CWs persist over observational timescales, making their detection a problem of long-term signal accumulation and coherence tracking. CW signals are typically modeled as nearly monochromatic sinusoids but require accounting for phase variations over long timescales.

A rotating neutron star in our galaxy can emit detectable continuous GWs if it has non-zero ellipticity, that is, a deviation from perfect axisymmetry,[14] such as a crustal deformation or internal deformations caused by non-axisymmetric trapped magnetic fields or fluid oscillations or exotic states of matter. A non-axisymmetric neutron star can be modeled as a triaxial ellipsoid. The characteristic strain amplitude of CWs from such a source at a distance r is given by [1]

$$h = \frac{4\pi^2 G I_3 f^2}{c^4 r}\epsilon \,, \tag{1.30}$$

[14] *Even an axisymmetric neutron star can emit GWs if its symmetry axis is misaligned with its spin axis; see Zimmermann and Szedenits [316].*

where $\epsilon \equiv (I_1 - I_2)/I_3$ is the ellipticity, I_3 is the principal moment of inertia about the rotation axis, I_1 and I_2 are the other two principal moments of inertia, and f is the GW frequency (which is twice the rotation frequency). For a typical neutron star of radius 10 km and a mass of $1.4M_\odot$ rotating at 0.5 kHz with an ellipticity of $\epsilon \sim 10^{-6}$ at a galactic distance of 10 kpc, Eq. (1.30) gives a strain amplitude

$$h \simeq 10^{-25}\left(\frac{\epsilon}{10^{-6}}\right)\left(\frac{I_3}{10^{38}\,\mathrm{kg\,m^2}}\right)\left(\frac{10\,\mathrm{kpc}}{r}\right)\left(\frac{f}{1\,\mathrm{kHz}}\right)^2 . \tag{1.31}$$

which is much smaller than the CBC strain amplitude.

Known pulsars provide 'targeted search' opportunities [18, 33] since their sky positions and rotational frequencies are well determined from electromagnetic observations. There are also 'all-sky searches' [9, 32, 283] that target unknown neutron star sources across a broad parameter space, demanding significant computational effort. 'Directed searches' [12, 28] target known sky locations (e.g., supernova remnants like Cassiopeia A [306]) where a neutron star is suspected but its spin frequency is unknown. By fixing the sky position, these searches reduce computational cost and can achieve greater sensitivity than all-sky searches. Despite no confirmed detections so far, upper

limits from CW searches have placed meaningful constraints on neutron star deformations and internal physics.

1.3.3 *Bursts*

Neutron stars and black holes can form from the collapse of massive stars or accreting white dwarfs. If the collapse is not perfectly spherical (often due to rapid rotation) it can emit GWs violently within a very short duration, carrying away some of the system's energy and angular momentum. These transient GW signals, commonly referred to as *bursts*, are expected from a wide variety of poorly-modeled or complex astrophysical scenarios. Examples include core-collapse supernovae, neutron star quakes, magnetar flares, cosmic string cusps, highly eccentric compact binary encounters or other unanticipated sources. Since the exact waveform of such events is not known a priori, burst searches in GW data rely on minimally modeled or unmodeled algorithms that look for coherent excess power across detectors without requiring detailed templates.

The characteristic strain amplitude h of GWs emitted by a source at distance r, releasing energy E over a duration T with dominant frequency f, can be estimated as [263]

$$h \sim \frac{1}{\pi f r}\sqrt{\frac{GE}{c^3 T}}\,. \tag{1.32}$$

As an example, consider a galactic supernova explosion that emits gravitational radiation with emitted energy equivalent of $10^{-7}M_\odot$ centered at a frequency of 1 kHz and lasting for 1 ms. The resulting strain amplitude received at a distance of 10 kpc would be

$$h \sim 6\times 10^{-21}\left(\frac{E}{10^{-7}M_\odot c^2}\right)^{1/2}\left(\frac{T}{1\,\mathrm{ms}}\right)^{-1/2}\left(\frac{1\,\mathrm{kHz}}{f}\right)\left(\frac{10\,\mathrm{kpc}}{r}\right)\,. \tag{1.33}$$

While the amplitudes are within the reach of current detectors, no confirmed detections have been made. Nonetheless, upper limits from burst searches - especially for nearby galaxies - are beginning to probe interesting astrophysical regimes [16, 23, 24].

1.3.4 *Stochastic background*

The stochastic gravitational wave background (SGWB) is a random superposition of numerous unresolved GW signals from a variety of sources, both astrophysical and cosmological. Unlike transient or continuous signals, the SGWB is characterized by its statistical properties rather than individual

waveforms. It is often described in terms of the dimensionless energy density parameter $\Omega_{\rm GW}(f)$, defined as

$$\Omega_{\rm GW}(f) \equiv \frac{1}{\rho_c}\frac{d\rho_{\rm GW}}{d\ln f}\,, \tag{1.34}$$

where $\rho_c = 3c^2H_0^2/(8\pi G)$ is the critical energy density of the universe, H_0 is the Hubble constant, and $\rho_{\rm GW}$ is the GW energy density per logarithmic frequency interval.

Astrophysical contributions to the SGWB arise from unresolved populations of CBCs, core-collapse supernovae, rotating neutron stars, stellar core collapses, superradiance of axion clouds around black holes etc. Cosmological contributions to the SGWB originate from processes in the early universe, such as inflation, phase transitions, cosmic strings, and pre-Big Bang scenarios. These sources can produce GWs across a wide range of frequencies, with some extending to the nanohertz regime probed by pulsar timing arrays (PTAs) or the millihertz band targeted by space-based detectors like LISA.

Detection of the SGWB relies on cross-correlating data from multiple detectors to extract the weak stochastic signal from uncorrelated instrumental noise[15] . The sensitivity of this method depends on the overlap reduction function, which encodes the relative orientation and separation of the detectors. Assuming the SGWB is a Gaussian, isotropic, unpolarized, and stationary random process, current observations from ground-based detectors have placed upper limits on the energy density spectrum $\Omega_{\rm GW}(f) \lesssim 10^{-9}$ in the frequency band accessible to the detector network [31]. PTAs have recently reported evidence for a nanohertz SGWB, potentially of astrophysical origin [42].

[15] *Allen and Romano [47] is a key early paper that explains how to use cross-correlation to detect the SGWB.*

1.4 OVERVIEW OF THE GRAVITATIONAL WAVE DETECTORS

GW detectors are broadly classified into two categories: beam detectors and resonant mass detectors. Beam detectors - including both ground-based and space-based instruments - operate on the principle of laser interferometry to measure differential changes in arm lengths caused by passing GWs. In contrast, resonant mass detectors, such as bar and spherical detectors, rely on the mechanical response of massive bodies to incident gravitational waves.

1.4.1 *Resonant mass detectors*

Resonant bar detectors consist of large, cryogenically cooled metal bars that vibrate when a GW excites their fundamental longitudinal mode. These tiny oscillations, typically at kHz frequencies, are converted into electrical signals using sensitive transducers. However, bar detectors are inherently narrowband, limiting their sensitivity to a small frequency range around their resonance.

Resonant spherical detectors improve upon this by offering broader directional sensitivity and isotropic sky coverage.

However, with the advent of laser interferometers that offer broad-band sensitivity, significantly improved strain resolution, and superior source localization capabilities, resonant mass detectors have become largely obsolete.[16] Interferometric detectors can monitor a wide frequency range simultaneously and are better suited for detecting a variety of transient and continuous signals from astrophysical sources. As a result, resonant detectors have been phased out from active use, though they played a foundational role in the early development of the field and in demonstrating the feasibility of GW detection.

[16] *The resonant bar detector concept was first introduced by Weber [303]. However, no resonant bar or spherical detectors are currently operational.*

1.4.2 *Beam Detectors*

Laser interferometers are the most sensitive and widely used GW detectors. These detectors employ two long, perpendicular arms with a laser beam split and sent down each arm. The beams reflect off highly isolated mirrors (test masses) placed at the ends of the arms and recombine at the beam splitter producing an interference pattern at the output. A passing GW induces differential length changes in the arms, producing a measurable time-varying interference pattern that encodes the GW signal.

The fundamental observable in such detectors is the dimensionless strain amplitude

$$h = \frac{\Delta L}{L} \,, \tag{1.35}$$

where ΔL is the GW-induced change in arm length, and L is the nominal arm length. For an interferometer with kilometer-scale arms using infrared lasers ($\lambda_{\text{laser}} \sim 1\,\mu\text{m}$), GW strain of the order $h \sim \lambda_{\text{laser}}/L = 10^{-9}$ can, in principle, be detected. To enhance sensitivity, Fabry-Pérot cavities with low-transmittivity mirrors are used in each arm, causing the laser to bounce $\sim 10^3$ times - effectively increasing the optical path. This improves strain sensitivity to $h \sim 10^{-12}$. Fig. 1.3 shows the schematic optical layout of the Advanced LIGO detector. A stabilized laser passes through an input mode cleaner before entering the main interferometer, where it is split into two 4 km perpendicular arms. Multiple reflections in the Fabry-Pérot cavities extend the effective arm length.

To further improve the sensitivity, *shot noise* - random quantum fluctuations in the number of detected photons - must be reduced. This can be achieved using high-power lasers and highly sensitive photodetectors. The effective power inside the interferometer can be increased by adding a *power recycling mirror* between the laser and the beam splitter. This mirror reflects light

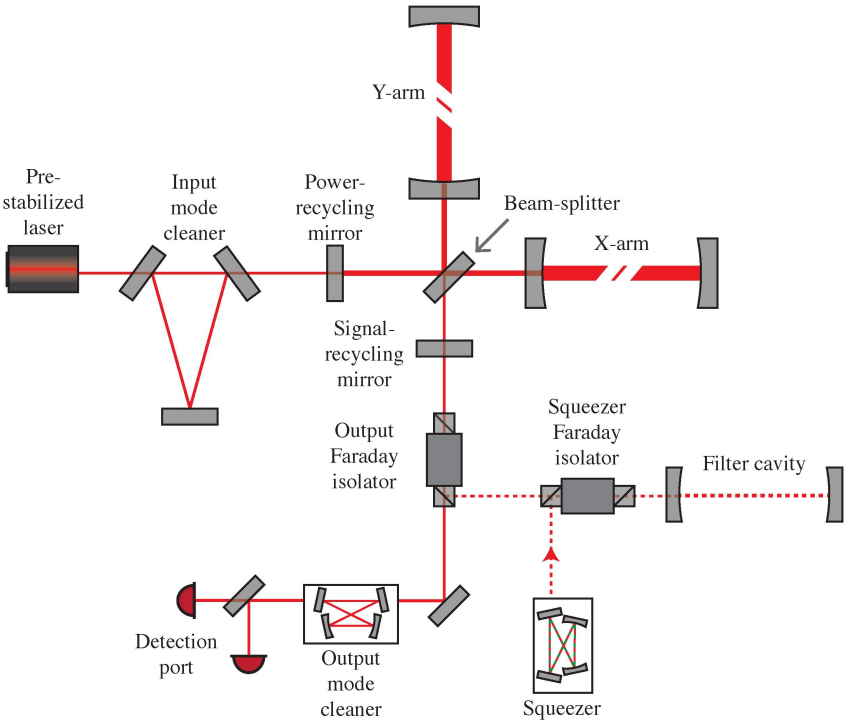

Figure 1.3: *Simplified optical layout of the Advanced LIGO detectors in the fourth observing run (O4). Credits: Cahillane and Mansell [86].*

that would otherwise leave the interferometer back into the arms, where it constructively interferes with incoming light. The resulting resonant buildup of optical power enhances the detector's strain sensitivity, allowing it to reach levels as low as $h \sim 10^{-20}$.

However, at high laser powers, quantum fluctuations in light intensity apply varying forces on the mirrors, leading to *radiation pressure noise*. This effect can be reduced by using heavier mirrors, which are less affected by these tiny forces. The two main quantum noise sources - shot noise and radiation pressure noise - are constrained by the Heisenberg uncertainty principle. Shot noise decreases with laser power, while radiation pressure noise increases, resulting in a trade-off that defines the *standard quantum limit* (SQL) for strain sensitivity. To surpass the SQL, *squeezed light* is injected into the interferometer. Squeezing redistributes quantum uncertainty to reduce noise without increasing laser power. For optimal performance across a wide frequency band, *frequency-dependent squeezing* is used. This requires a *filter cavity* that rotates the squeezing angle as a function of frequency - reducing shot noise at high frequencies and radiation pressure noise at low frequencies.

The output beam then passes through a *Faraday isolator*, which prevents light from re-entering the interferometer. It then passes through an *output mode cleaner*, which removes unwanted light modes before the signal reaches the detectors. For more details, see Capote et al. [87].

Apart from the noise sources mentioned earlier, the interferometer is also sensitive to *seismic noise* and *Newtonian noise* at low frequencies. *Thermal noise* from the optics and suspension systems become dominant at intermediate

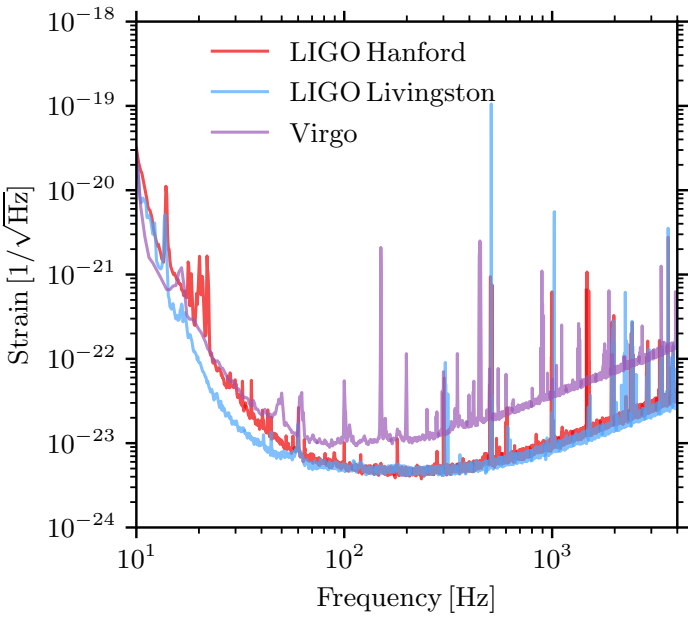

Figure 1.4: *Amplitude spectral density (ASD) of the total strain noise for the LIGO-Hanford (red), LIGO-Livingston (blue) and Virgo (violet) detectors, representative of their best sensitivities during the third observing run(O3). Adapted from Abbott et al. [26]*

frequencies. These disturbances are mitigated through advanced seismic isolation systems, multi-stage suspensions, and, in some upcoming detectors, cryogenic cooling of the optical components.

Current generation of interferometers, such as the Advanced LIGO in the USA, and the Advanced Virgo [38] in Italy are capable of measuring strain amplitudes $\sim 10^{-22}$ or even smaller. Fig. 1.4 shows the *amplitude spectral density* (ASD) of the strain sensitivity for the two LIGO detectors (Hanford and Livingston) and the Virgo detector during the third observing run. The ASD quantifies the detector's noise level as a function of frequency, with lower values indicating better sensitivity.

1.4.3 *Detector response functions of ground-based interferometers*

The sensitivity of a GW detector depends not only on the strain amplitude but also on its orientation and position relative to the source. The *detector response functions*, also known as *antenna pattern functions*, quantify how the detector responds to GWs from different sky positions and polarizations.

For a GW propagating along $\hat{\mathbf{n}}$ direction, the TT strain tensor $h_{ij}^{\mathrm{TT}}(t)$ (see Eq. (1.19)) can be written as a linear combination of the two polarizations, $h_+(t)$ and $h_\times(t)$ as

$$h_{ij}^{\mathrm{TT}}(t) = h_+(t)\, e_{ij}^{+}(\hat{\mathbf{n}}) + h_\times(t)\, e_{ij}^{\times}(\hat{\mathbf{n}}) \,, \tag{1.36}$$

where e_{ij}^{+} and $e_{ij}^{\times}$ are the polarization basis tensors orthogonal to the propagation direction. A laser interferometric detector responds to the GW through the contraction of the TT metric perturbation with the detector tensor D^{ij}, which

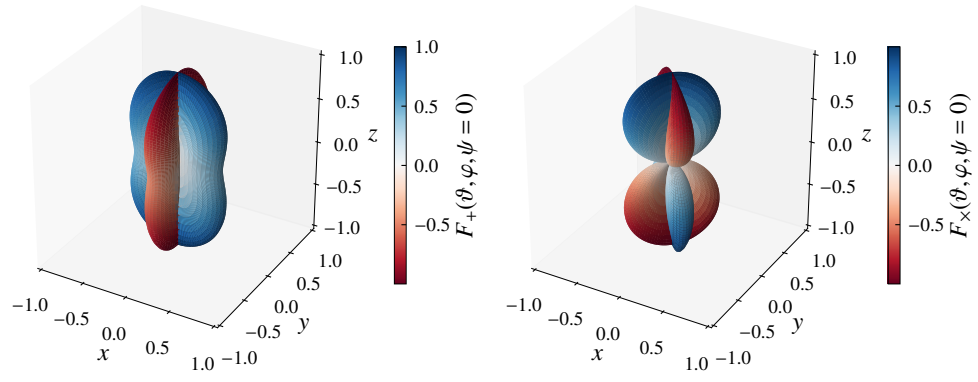

Figure 1.5: *Normalized detector response functions for an interferometric ground-based detector with orthogonal arms along the x- and y-axes.*

encodes the geometry and orientation of the detector arms. The measured strain is given by

$$h(t) = D^{ij} h_{ij}^{\mathrm{TT}}(t) = F_+(\hat{\mathbf{n}})\, h_+(t) + F_\times(\hat{\mathbf{n}})\, h_\times(t)\ , \tag{1.37}$$

where $F_+ \equiv D^{ij} e_{ij}^{+}$ and $F_\times \equiv D^{ij} e_{ij}^{\times}$ are the detector's response functions to the $+$ and $\times$ polarizations, respectively. These functions are independent of the signal frequency in the long-wavelength approximation, but depend on the direction of the source $\hat{\mathbf{n}}$ and the polarization angle ψ, which defines the rotation of the polarization axes about $\hat{\mathbf{n}}$.

To make this dependence explicit, we introduce the angles (ϑ, φ) to specify the source location in a detector-centered (Earth-fixed) spherical coordinate system: ϑ is the polar angle measured from the detector's zenith (the z-axis), and φ is the azimuthal angle measured in the x–y plane. The antenna pattern functions then take the form [208]

$$F_+(\vartheta, \varphi, \psi) = \frac{1}{2}(1 + \cos^2\vartheta)\cos 2\varphi \cos 2\psi - \cos\vartheta \sin 2\varphi \sin 2\psi\ , \tag{1.38a}$$

$$F_\times(\vartheta, \varphi, \psi) = \frac{1}{2}(1 + \cos^2\vartheta)\cos 2\varphi \sin 2\psi + \cos\vartheta \sin 2\varphi \cos 2\psi\ . \tag{1.38b}$$

Fig. 1.5 shows the antenna pattern functions for $\psi = 0$. While GW interferometers exhibit broad sky coverage, they also possess blind spots - directions from which signals cannot be detected effectively. Importantly, a single detector cannot localize a GW source on the sky, as it lacks directional sensitivity. To overcome this, a network of detectors is essential. The observed signal depends on four unknowns: $h_+, h_\times, \vartheta$ and φ. Resolving all four parameters requires at least three non-aligned detectors.

1.4.4 *Current and future gravitational wave detectors*

The current LIGO-Virgo-KAGRA (LVK)[17] detector network has detected ~ 90 CBC events across its first three observing runs (O1, O2 and O3) [10, 25, 26, 37], with independent reanalyses identifying additional candidates [221, 241,

[17] *KAmioka GRAvitational wave detector (KAGRA) [45] is a detector in Japan.*

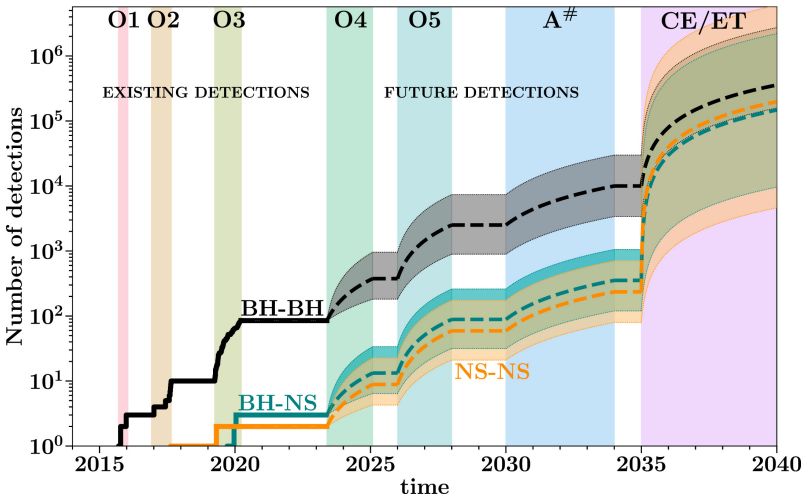

Figure 1.6: *Current and projected number of GW detections with future ground-based detectors. Adapted from Broekgaarden, Banagiri, and Payne [83].*

244, 300]. The ongoing fourth observing run (O4) has already expanded the catalog of candidate CBC events by $\sim$ 200, with more detections expected as the run progresses[18] . Operating in the $\sim$ 10 Hz $-$ 10 kHz band, these detectors are primarily sensitive to stellar-mass compact binaries. The addition of the planned LIGO-Aundha detector [290], in India, to the network is expected to significantly enhance the sky localization of GW events, improve polarization disentanglement, increase the detection rate and yield better parameter estimation (PE) due to improved sky coverage and duty cycle [261].

[18] *Public alerts from O4 can be viewed at GraceDB*

Next-generation ground-based detectors (often referred to as 'XG' or '3G' detectors) such as the Einstein Telescope (ET) [254] in Europe and the Cosmic Explorer (CE) [17] in the USA aim to achieve an order-of-magnitude improvement in strain sensitivity and extend the accessible frequency band to lower frequencies ($\sim$ 1 Hz). LIGO Voyager [40], a proposed upgrade to the Advanced LIGO detectors, can potentially serve as a test bed for technologies required for ET and CE. Additionally, the Neutron Star Extreme Matter Observatory (NEMO) [39] proposed in Australia, is a detector optimized for neutron star science with target sensitivity comparable to ET and CE above 2 kHz. These advancements will enable high *signal-to-noise ratio* (SNR) detections out to cosmological distances, probing the population of compact objects throughout the universe and offering a window into previously inaccessible aspects of fundamental physics [132, 209]. Fig. 1.6 shows the current and projected number of detections with the ground-based detectors. Voyager ($A^{\#}$) is expected to detect $\sim$ 100 times more sources as compared to the current detectors, while ET and CE are expected to push the detection rate to an astonishing $\sim 10^5 - 10^6$ events per year.

Refer to Bailes et al. [54] for a review on the future GW detectors and science prospects.

Space-based detectors, such as the LISA [49], will operate in the millihertz frequency band ($\sim$ 0.1 mHz $-$ 100 mHz), targeting intermediate-mass and SMBH binaries ($10^2 - 10^7 M_\odot$), extreme mass-ratio inspirals (EMRIs, binaries with mass ratios as small as $\sim 10^{-6}$), and a variety of cosmological sources out to redshifts $z \sim 20$ or more. LISA will also enable multiband observa-

tions by detecting early inspiral stages of stellar-mass binaries much before they enter the detectable band of the ground-based detectors. Additionally it will uncover new population of galactic binaries including white dwarf binaries allowing a population census and mapping the structure of the Milky Way [269]. Several complementary missions are in planning and development, including the Chinese-led TianQin [202] and Taiji [171] constellations. Both are based on LISA-like designs with modified orbital and instrumental parameters. Looking beyond, next-generation space-based observatories aim to extend sensitivity above and below LISA's band. In particular, DECihertz Interferometer Gravitational wave Observatory (DECIGO) [187], a proposed Japanese mission, targets the range of $0.1 - 10\,\mathrm{Hz}$ and is designed to probe primordial GWs.

PTAs [182, 195, 211, 212] are sensitive to $\sim 1\,\mathrm{nHz} - 1\,\mu\mathrm{Hz}$ GWs. They measure correlated variations in the timings of highly stable millisecond pulsars caused due to spacetime distortions from passing GWs. These variations follow a characteristic angular correlation across the sky known as the Hellings-Downs curve [165]. Monitoring an array of pulsars across the sky allows PTAs to probe the nanohertz GW background, primarily from SMBH binaries. Future PTAs plan on improving the sensitivity by deploying better receivers on telescopes. Further, the advent of Square Kilometer Array (SKA) is expected to greatly expand the pulsar population and enhance timing precision [181].

Together, ground-based detectors, space-based missions and PTAs provide a complementary and comprehensive coverage of the GW spectrum – from nHz to kHz frequencies. This multi-band approach will not only expand the catalog of GW events but also deepen our understanding of astrophysics, cosmology and fundamental physics.

Although future detectors promise major scientific gains, they also introduce significant challenges. The large number of high-SNR detections will substantially increase the computational cost of PE including hierarchical inference of population parameters, and will necessitate more flexible population models. Accurate waveform modeling will become even more crucial, particularly for systems exhibiting precession, eccentricity and higher modes [257]. For long-duration signals, strategies such as reduced data rates [227] or heterodyning [109, 315] can help manage computational demands. While machine learning has demonstrated rapid parameter inference for signal durations of a few seconds [115], the increasing data volume will require efficient data compression and scalable, reliable computational platforms (e.g. Inference-as-a-Service [157]). Enhanced sensitivity will also amplify subtle noise features, such as glitches, making their modeling and subtraction essential. In future detectors, noise may need to be estimated concurrently with signals [252],

particularly for space-based observatories where 'off-source' data may not exist.

1.5 SCIENCE WITH GRAVITATIONAL WAVES

A decade since the very first detection of GWs (GW150914) [3] from the merger of two black holes with masses $\sim 36\,M_\odot$ and $\sim 29\,M_\odot$ observed on September 14, 2015, GW astronomy has grown into a powerful tool for exploring the universe. It provides direct access to the dynamics of strong-field gravity and enables detailed studies of compact object populations. While the majority of detections till O3 are BBH mergers, the catalog also includes two BNS (GW170817 [6] and GW190425 [15])[19] and two neutron star - black hole (NSBH, GW200105 and GW200115 [27]) mergers. The following sections highlight some of the ways in which GWs serve as unique probes of fundamental physics, astrophysics and cosmology.

[19] *The nature of GW190425 remains uncertain owing to large chirp-masses; either or both components may be black holes.*

1.5.1 *Fundamental physics*

GW detections have enabled testing the nature of gravity in the strong-field, highly dynamical regime. Remarkably, GW150914 alone has placed an upper bound on the graviton mass of $m_g < 1.2 \times 10^{-22}\,\mathrm{eV}/c^2$ [4], improving previous constraints obtained from Solar System and binary pulsar tests.[20] On August 17, 2017, the first BNS merger, GW170817, with associated EM counterparts, confirmed upto an unprecedented accuracy that GWs propagate at the speed of light to within one part in 10^{15} [7]. This result effectively rules out parameter spaces of large class of modified gravity models that predict significant deviations between the speeds of gravity and that of light. This detection has also constrained the number of space-time dimensions [13, 246]. Theory agnostic tests have been extensively applied [14, 29, 30], with no statistically significant departure from GR observed. Future detectors will be able to extend these tests across a wide range of curvature and length scales, enhancing sensitivity to potential deviations from GR [147, 314]. The ringdown signal of GW150914 has been used to test the black hole area theorem [173], finding consistency with GR. GW observations also allow putting constraints on additional polarization modes predicted by alternative theories of gravity [19, 174].

[20] *Bounds on the graviton mass have improved by an order of magnitude [29], with further gains expected from 3G detectors.*

GW observations offer new ways to investigate the nature of dark matter (DM). One possibility is that DM is partly composed of primordial black holes (PBHs) of masses $\sim 0.1 - 100\,M_\odot$ [74, 106, 262]. GW detections of binaries with sub-solar mass components or an unexpected excess in specific mass ranges could indicate the presence of PBHs [11]. Observing sources at very high redshift would further support this scenario [194]. GWs also test particle

DM models beyond the Standard Model. In such cases, BBHs in dense DM environments may experience dynamical friction and accretion, altering their inspiral dynamics and leaving detectable imprints on the GW signal [89, 126, 203].

Compact binary mergers also allow us to test the nature of compact objects. In particular, they provide insights into the equation of state (EOS) of dense matter at supranuclear densities, probing regimes inaccessible to laboratory experiments. Matter effects leave imprints on the waveform during tidal disruption in NSBH systems and the merger and post-merger phases of BNS events [55, 196]. GW170817 ruled out several stiff EOS models and constrained the radii of the neutron star components to be within $9 - 13\,\mathrm{km}$ [6, 214]. 3G detectors are expected to improve these constraints to within a few hundred metres and may allow measurements of central densities and pressures inside neutron stars [264]. Additionally, GWs can help identify exotic compact objects (ECOs) that differ from black holes due to their non-zero tidal deformability [183]. Signatures in the ringdown phase or the presence of GW "echoes" may provide evidence for non-standard compact object interiors [71].

1.5.2 *Astrophysics*

The detection of GW170817 marked the dawn of GW multi-messenger astronomy, being the first event observed with EM counterparts across the spectrum, including a gamma-ray burst (GRB170817a) and a kilonova [8]. It provided the first direct confirmation that BNS mergers are progenitors of short gamma-ray bursts (GRBs) [7, 150], enabled the first unambiguous detection of a kilonova [51, 112, 113, 133, 273, 292], and offered compelling evidence that BNS mergers are a primary site for the synthesis of heavy elements via *r*-process nucleosynthesis [123, 185, 186, 249, 302].

GWs provide a unique window into the origin and evolution of compact object binaries. They enable detailed survey of black hole demographics, including their mass and spin distributions. Uncertainties in the BBH mass distribution directly affect the inferred merger rates, which currently range between $16 - 61\,\mathrm{Gpc}^{-3}\mathrm{yr}^{-1}$ at the present epoch. However, there is strong evidence suggesting that the merger rate increases with redshift [35]. GWs also probe the binary formation channels. Broadly, BBHs can originate either from an isolated binary evolution or dynamical formation through interactions in dense stellar environments.[21]

Events such as GW190814 - the merger of a $\sim 23\,M_\odot$ black hole with a compact object of mass $\sim 2.6\,M_\odot$ - challenge our understanding of the so-called "lower mass gap" between neutron stars and black holes, traditionally expected to lie between $\sim 2 - 5\,M_\odot$ [21]. Similarly, GW190521 resulted in the formation of the first observed intermediate-mass black hole (IMBH, black

[21] *For a comprehensive review on the formation channels of single and binary black holes, see Mapelli [213].*

holes in the mass range $10^2 - 10^4\, M_\odot$) with a remnant mass of $\sim 142 M_\odot$ [20]. The primary component of this system, with a mass of $\sim 85\, M_\odot$, falls within the predicted "pair-instability mass gap", implying a possible hierarchical coalescence of smaller black holes or a stellar merger between a massive evolved star and a main-sequence companion [22].

These discoveries highlight the transformative potential of GW observations in astrophysics. As detector sensitivities improve and event catalogs grow, we anticipate uncovering eccentricity and precession in compact object mergers, refining models of stellar evolution, and probing environments previously inaccessible to traditional EM astronomy.

1.5.3 *Cosmology*

GWs offer an independent measurement of cosmological parameters. From the GW signal alone, it is possible to infer the *luminosity distance* to the source, without relying on a cosmic distance ladder. This concept, originally proposed by Schutz [266], was spectacularly realized with GW170817. The combination of the GW-inferred distance and the redshift obtained from its EM counterparts enabled a direct measurement of the Hubble constant, inaugurating the use of GWs as *standard sirens* [5].

Even in the absence of EM counterparts, statistical association with galaxy catalogs allows for cosmological inference by cross-matching the localization volumes of GW events with galaxy redshift surveys [34, 154]. With a sufficient number of such events, this method becomes increasingly powerful and can yield competitive constraints on cosmological parameters.

GW measurements also have the potential to address the current tension in Hubble constant measurements between the local distance ladder and cosmic microwave background (CMB) inference. By providing an independent distance-redshift relation, GWs can help determine whether this tension arises from unknown systematics or signals new physics [137].

Beyond the Hubble constant, GWs can be used to probe deviations from GR on cosmological scales through modified GW propagation effects [142, 210]. Additionally, cross-correlating the spatial distribution of GW events with galaxy surveys - leveraging the fact that compact binaries trace the underlying large-scale structure - can provide constraints on the matter density, bias of GW host environments, and the growth of cosmic structure [230, 231].

As the number of detected events increases and localization accuracy improves, especially with next-generation GW detectors, GW cosmology is expected to become a cornerstone of precision cosmology.

2

GRAVITATIONAL LENSING

The 1919 observation of the bending of star-light around the Sun during a total solar eclipse marked the first experimental confirmation of GR [124], measuring a deflection twice as large as predicted by Newtonian gravity. This bending of light - referred to as *gravitational lensing* - occurs when the curvature of spacetime around massive objects, or *lenses*, alters the path of the incident radiation. Over the past century, gravitational lensing of EM radiation has established itself as a powerful tool in astrophysics and cosmology, with applications ranging from mapping the dark matter distribution in galaxy clusters [107], constraining compact dark matter [297], discovering exoplanets [148], observing distant galaxies and clusters [190, 287], to measuring the Hubble constant [258, 288].

Analogous to EM radiation, GWs also experience lensing when they propagate near massive compact objects or mass distributions. However, GW lensing exhibits distinct features depending on the ratio between the GW wavelength, $\lambda_{\rm GW}$, and the characteristic gravitational length scale of the lens. When the wavelength is significantly smaller than the gravitational radius of the lens, i.e., $\lambda_{\rm GW} \ll GM_{\rm L}/c^2$,[1] lensing can be described using the geometric-optics approximation [80, 265]. Furthermore, if the angular separation between the source and the lens in the sky plane is sufficiently small, multiple lensed copies of the signal can form [120, 134, 135, 151, 162, 200, 301]. These copies will arrive at the detectors at different times - ranging from minutes to months for galaxy-scale lenses and days to years for cluster-scale lenses[2] . This phenomena is referred to as *strong lensing*, and has a similar phenomenology as EM lensing. While the phase evolution of the lensed signals remains nearly identical, they can exhibit relative magnifications and constant phase shifts, which encode information about the lensing geometry.

On the other hand, if $\lambda_{\rm GW} \sim GM_{\rm L}/c^2$, wave-optics effects become significant and a single frequency-modulated, diffracted signal is produced [119, 233, 234, 279][3] . This regime is referred to as *microlensing*. It is almost impossible to observe diffraction effects due to lensing in EM waves, owing to their small wavelengths. Gravitational microlensing of GWs in the LVK frequency band occurs for microlenses (or compact objects) whose masses lie in the range $M_{\rm L} \in\sim \left[10^2 - 10^4\right] M_\odot$. Examples of candidate microlenses include, but are not limited to, IMBHs [197] and other exotic compact objects such as boson stars [199] and gravastars [218]. Such wave-optics signatures enable the exploration of lensing effects at scales beyond the reach of optical

[1] *$M_{\rm L}$ is the mass of the lens.*

[2] *GWs are temporally well-resolved but lack spatial resolution. Hence, the primary GW lensing observables are relative magnifications and time delays between the signal copies.*

[3] *Note that there could also be wave-optics effects due to interference since GWs from compact binaries are coherent. See, e.g. Leung et al. [198].*

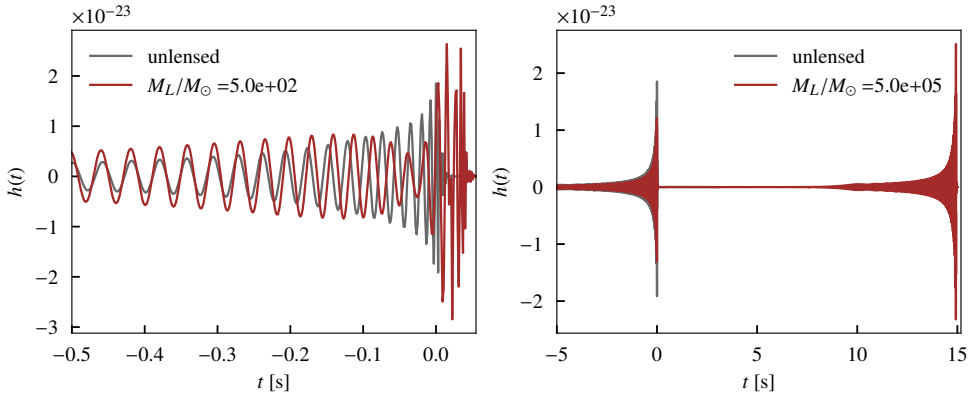

Figure 2.1: *Comparison of lensed and unlensed GW waveforms lensed by a point mass lens in the wave-optics regime (left) and the geometric-optics regime (right).*

or radio telescopes, offering a unique avenue for discovering previously unobserved lens populations. However, detection rates with current ground-based detectors remain highly uncertain due to uncertainty in the abundance and mass distribution of such lenses [104, 197, 268]. Beyond probing compact object population, diffraction effects play a crucial role in modeling signals originating near the *critical curve(s)* of a lens such as a galaxy.

Fig. 2.1 illustrates gravitational lensing of GWs in the wave-optics (left panel) and geometric-optics (right panel) regimes due to a *point mass lens* (see Sec. 2.4.1 for details) of mass $5 \times 10^2\, M_\odot$ and $5 \times 10^5\, M_\odot$, respectively. The unlensed waveforms (strain amplitude $h(t)$) are shown in grey and the lensed waveforms in brown. In the left panel, characteristic diffraction-induced modulations caused by microlensing are visible while multiple signals arriving at different times with relative magnifications are evident in the right panel.

In addition to microlensing and strong lensing, GWs can also undergo *weak lensing* due to the large-scale structures in the Universe [117]. In this regime, cumulative deflection by numerous low-amplitude potentials (e.g. galaxies, groups and filaments) introduces subtle distortions in the observed signal. Although these distortions leave the intrinsic shape of the waveform essentially unchanged, they introduce a small bias in the inferred luminosity distance [169, 243]. These effects become particularly relevant at high redshifts, $z \gtrsim 1$. For current ground-based detectors which typically observe binary mergers at $z \lesssim 0.8$, weak lensing noise remains subdominant compared to instrumental and calibration errors [168]. However, 3G detectors will be sensitive to sources beyond $z = 10$, making weak lensing a significant contributor to distance uncertainty.

While no confirmed detections of strong lensing or microlensing have been reported in the LVK data to date [36, 160][4] , a small yet significant fraction ($\sim 0.1 - 1\%$) [242, 309] of GW events detected by future ground-based detectors are expected to be strongly lensed. This increase is primarily driven by the extended detection horizon and improved sensitivity of future observatories, which boost the likelihood of intervening lensing structures. These anticipated lensing observations will open up a plethora of new opportunities, including

[4] *The current non-observation of lensed events is consistent with the low expected lensing rate of $\lesssim 0.05\%$ for current detector sensitivities. See, e.g., Ng et al. [239] and Wierda et al. [307]*

novel tests of GR [105, 108, 136, 143, 152, 153, 232, 236] and providing fresh insights into a number of key questions in astrophysics [67, 207, 272] and cosmology [66, 161, 179, 180]. In the coming years, gravitational lensing of GWs is expected to evolve into a cornerstone observational channel, complementing traditional EM lensing and advancing the frontier of multi-messenger astrophysics.

In this chapter, we present a brief overview of the propagation of GWs in the presence of a lens. We then look at the theory of wave-optics lensing before moving on to the geometric-optics approximation. Finally, we introduce the lens models relevant for this thesis.

2.1 PROPAGATION OF GRAVITATIONAL WAVES IN GENERAL SPACETIMES

In Sec. 1.1 we obtained the equations governing propagation of gravitational perturbations on a Minkowski background (see, Eq. (1.4)). However, in realistic settings, these perturbations traverse curved spacetimes. This necessitates a more general treatment in which the perturbation $h_{\mu\nu}$ is defined on a non-flat background metric $\bar{g}_{\mu\nu}$. The full spacetime metric is then written as

$$g_{\mu\nu}(t,\mathbf{r}) = \bar{g}_{\mu\nu}(t,\mathbf{r}) + h_{\mu\nu}(t,\mathbf{r}) \ . \tag{2.1}$$

Such a clear separation between the spacetime background and the GW perturbations is valid under the following assumptions:

1. the amplitude of perturbation is small, i.e., $|h_{\mu\nu}| \ll 1$, and
2. the characteristic length scale of the perturbation - which is the reduced GW wavelength, $\lambda\!\!\!^{-} \equiv \lambda_{\rm GW}/(2\pi)$ - is much smaller than the typical curvature scale $L_{\rm B}$ of the background as measured in a local inertial frame, i.e., $\lambda\!\!\!^{-} \ll L_{\rm B}$.

This hierarchy of scales justifies a perturbative expansion of the Einstein equations, where the background evolves on large scales and the GW modes represent high-frequency perturbations superposed on it. In this regime, the background determines the geometric optics behavior of wave propagation, while the GWs follow transport equations along null geodesics.

To proceed, we define the trace-reversed metric perturbation analogous to Eq. (1.3) as

$$\bar{h}_{\mu\nu} \equiv h_{\mu\nu} - \frac{1}{2}\bar{g}_{\mu\nu}h, \quad h = \bar{g}^{\mu\nu}h_{\mu\nu} \ , \tag{2.2}$$

and impose the Lorenz gauge as well as the transverse traceless condition

$$\bar{\nabla}^{\nu}\bar{h}_{\mu\nu} = 0, \bar{h}^{\mu}_{\mu} = 0 \ , \tag{2.3}$$

where $\bar{\nabla}$ denotes the covariant derivative operator defined with respect to the background metric. Under these conditions, the linearized Einstein equations in curved spacetime take the form [226]

$$\bar{g}^{\alpha\beta}\bar{\nabla}_\alpha\bar{\nabla}_\beta\bar{h}_{\mu\nu} = 0 \,. \tag{2.4}$$

Here we retain terms of order $\mathcal{O}(|h_{\mu\nu}|\lambda\!\!\!^{-2})$ while neglecting terms of order $\mathcal{O}(|h_{\mu\nu}|L_{\rm B}^{-2})$ and higher. This yields a wave equation for the perturbation $\bar{h}_{\mu\nu}$ on the curved background, the solution to which can be written as [60]

$$\bar{h}_{\mu\nu}(t,\mathbf{r}) = A_{\mu\nu}(t,\mathbf{r})\exp\left[i\theta(t,\mathbf{r})\right] \,, \tag{2.5}$$

where we have assumed that the amplitude $A_{\mu\nu}$ is slowly varying (on a scale $l \lesssim L_{\rm B}$) while the phase θ varies rapidly (on a length scale $\lambda\!\!\!^{-}$)[5] .

[5] *This is referred to as the short-wave (WKB) approximation or the Eikonal approximation.*

2.2 DIFFRACTION EFFECTS IN GRAVITATIONAL LENSING

Consider GWs propagating through a *static, weak-field spacetime* of a gravitational lens described by the metric

$$ds^2 \equiv \bar{g}_{\mu\nu}\,dx^\mu\,dx^\nu = -\left(1+\frac{2U}{c^2}\right)c^2dt^2 + \left(1-\frac{2U}{c^2}\right)d\mathbf{r}^2 \,, \tag{2.6}$$

where $U(\mathbf{r}) \ll c^2$ is the Newtonian potential associated with the lens. In this background, the trace-reversed metric perturbation $\bar{h}_{\mu\nu}$ given in Eq. (2.5) can be expressed as

$$\bar{h}_{\mu\nu}(t,\mathbf{r}) = \mathcal{A}(t,\mathbf{r})\exp\left[i\theta(t,\mathbf{r})\right]e_{\mu\nu} = \phi(t,\mathbf{r})\,e_{\mu\nu} \,, \tag{2.7}$$

where $e_{\mu\nu}$ is the normalized polarization tensor, and the scalar function $\phi \equiv \mathcal{A}\exp[i\theta]$ captures the leading order behaviour of the perturbation. It can be shown that the polarization tensor is parallel-transported along the null geodesics [226]. Since the parallel-transport induces changes of order U/c^2 in $e_{\mu\nu}$, and given that $U/c^2 \ll 1$, these changes are negligible in the weak-field lensing regime. We therefore treat $e_{\mu\nu}$ as constant along the GW trajectory. Under this assumption, the propagation equation, Eq. (2.4), reduces to a scalar wave equation for ϕ, given by

$$\partial_\mu\left(\sqrt{-\bar{g}}\bar{g}^{\mu\nu}\partial_\nu\phi(t,\mathbf{r})\right) = 0 \,, \tag{2.8}$$

where $\bar{g} \equiv \det(\bar{g}_{\mu\nu})$. For the weak-field metric in Eq. (2.6), the scalar wave equation above takes the form

$$\nabla^2\phi(t,\mathbf{r}) - \left[1-4U(t,\mathbf{r})\right]\partial_t^2\phi = 0 \,, \tag{2.9}$$

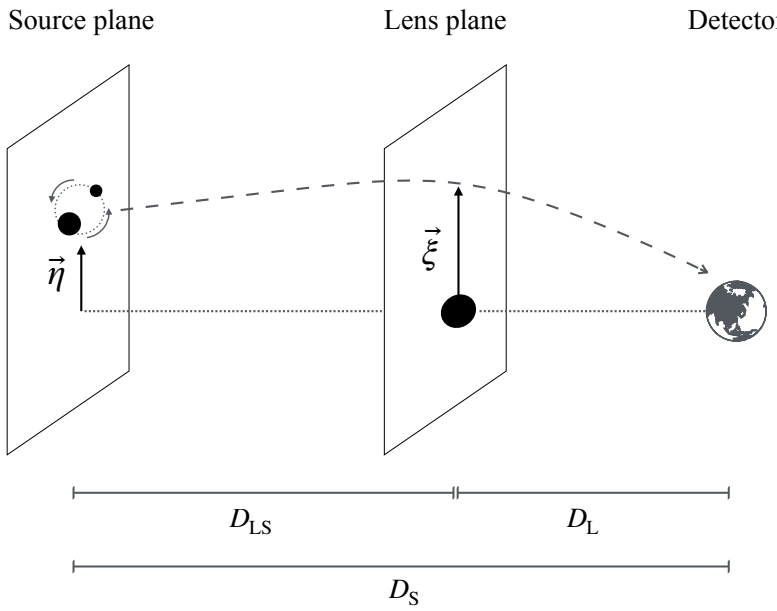

Figure 2.2: *Lensing geometry for a source (a compact binary merger) at redshift $z_{\rm S}$, the lens (a compact object within thin lens approximation) at redshift $z_{\rm L}$, and the ground-based detector. The dotted line denotes the optical axis while the dashed line denotes the deflected path of the incoming signal.*

with ∇^2 denoting the flat-space Laplacian operator. Here we have supressed the factors of c for notational clarity. Expressing $\phi(t, \mathbf{r})$ as a Fourier integral

$$\phi(t, \mathbf{r}) = \int_{-\infty}^{\infty} \tilde{\phi}(\omega, \mathbf{r}) e^{-i\omega t}\, d\omega \ , \tag{2.10}$$

and substituting into Eq. (2.9) results in the frequency-domain equation

$$\left(\nabla^2 + \omega^2\right) \tilde{\phi}(\omega, \mathbf{r}) = 4\omega^2\, U(\mathbf{r})\, \tilde{\phi}(\omega, \mathbf{r}) \ . \tag{2.11}$$

Fig. 2.2 illustrates the geometry of gravitational lensing involving a GW source located at redshift $z_{\rm S}$, a lens at redshift $z_{\rm L}$ and a detector. The corresponding angular diameter distances from the observer are $D_{\rm S}$ and $D_{\rm L}$ for the source and the lens, respectively, while $D_{\rm LS}$ is the angular diameter distance between the lens and the source.

We adopt the *thin lens approximation*, which assumes that the physical extent of the lens along the optical axis[6] is much smaller than its distances from both the source and the observer. Under this approximation, all lensing effects are localized to a two-dimensional lens plane perpendicular to the optical axis. As seen in Fig. 2.2, the transverse position vectors $\boldsymbol{\eta}$ and $\boldsymbol{\xi}$ represent coordinates in the source and the lens planes, respectively.

[6] *Optical axis is the line connecting the observer to the center of the lens*

The central quantity of interest is the *lensing magnification function* or *amplification factor* defined as

$$\mathcal{F}(\omega, \boldsymbol{\eta}) \equiv \frac{\tilde{\phi}^{\rm L}_{\rm det}(\omega, \boldsymbol{\eta})}{\tilde{\phi}^{0}_{\rm det}(\omega, \boldsymbol{\eta})} \ , \tag{2.12}$$

where $\tilde{\phi}^{\rm L}_{\rm det}$ is the Fourier-domain waveform observed at the detector in the presence of lensing, whereas $\tilde{\phi}^{0}_{\rm det}$ is the corresponding waveform in the absence

of any lens (i.e., for $U = 0$). Both quantities are solutions to the scalar wave equation in the weak field regime as given by Eq. (2.11). This magnification function can be computed using either the *Kirchhoff diffraction integral* [81, 265] or the *path integral approach* [198, 234] giving

$$\mathcal{F}(\omega, \boldsymbol{\eta}) = \frac{D_S}{D_L D_{LS}} \frac{\omega}{2\pi i c} \int d^2\boldsymbol{\xi} \, \exp\left[i\omega t_d(\boldsymbol{\xi}, \boldsymbol{\eta})\right] \, , \tag{2.13}$$

normalized such that $|\mathcal{F}| = 1$ in the unlensed case. Here t_d is the arrival time of the GW at the detector from the source position $\boldsymbol{\eta}$ and going through $\boldsymbol{\xi}$ on the lens plane, given by [265]

$$c t_d(\boldsymbol{\xi}, \boldsymbol{\eta}) = \frac{D_L D_S}{2 D_{LS}} \left(\frac{\boldsymbol{\xi}}{D_L} - \frac{\boldsymbol{\eta}}{D_S} \right)^2 - \hat{\Psi}(\boldsymbol{\xi}) + \hat{\phi}_m(\boldsymbol{\eta}) \, , \tag{2.14}$$

where the first term denotes the *geometric time delay* which is obtained from the path difference between the deflected and the undeflected rays. The second term is the *gravitational time delay* or *Shapiro delay* and is represented by the *deflection potential* $\hat{\Psi}$. This is solely determined by the lens model. The third term, $\hat{\phi}_m$, can be chosen such that the minimum value of the arrival time is zero.

The difference between the directions of the incoming and outgoing rays before and after undergoing lensing is given by the *deflection angle* $\hat{\boldsymbol{\alpha}}$. Assuming that this deflection angle is small, we can invoke the *Born approximation*, which allows us to evaluate the deflection along the unperturbed path of the ray. Under this approximation, the deflection angle is given by

$$\hat{\boldsymbol{\alpha}}(\boldsymbol{\xi}) = \frac{2}{c^2} \int_{-\infty}^{\infty} dz \frac{\partial U(\boldsymbol{\xi}, z)}{\partial \boldsymbol{\xi}} \, , \tag{2.15}$$

where the lens is assumed to be at $z = 0$, with z being the optical axis coordinate, perpendicular to the lens plane. We can then compute the deflection potential by solving

$$\frac{\partial \hat{\Psi}(\boldsymbol{\xi})}{\partial \boldsymbol{\xi}} = \hat{\boldsymbol{\alpha}}(\boldsymbol{\xi}) \, . \tag{2.16}$$

Though the background metric in Eq. (2.6) does not explicitly include cosmic expansion, the results are applicable to cosmological scenarios because GW wavelengths are much smaller than the horizon scale [60]. In such cases the magnification function becomes

$$\mathcal{F}(\omega, \boldsymbol{\eta}) = \frac{D_S}{D_L D_{LS}} \frac{\omega(1 + z_L)}{2\pi i c} \int d^2\boldsymbol{\xi} \, \exp\left[i\omega t_d(\boldsymbol{\xi}, \boldsymbol{\eta})\right] \, . \tag{2.17}$$

To proceed further, it is convenient to define the dimensionless vectors:

$$\mathbf{x} \equiv \frac{\boldsymbol{\xi}}{\xi_0}, \, \mathbf{y} \equiv \frac{D_\mathrm{L}}{D_\mathrm{S}} \frac{\boldsymbol{\eta}}{\xi_0} \, , \tag{2.18}$$

where ξ_0 is a characteristic lensing length scale, often set to be the *Einstein radius* of the lens. The *source position* $\mathbf{y}$ and the *impact parameter* $\mathbf{x}$ are measured from the optical axis. Moreover, we also introduce the dimensionless frequency

$$w \equiv \frac{D_\mathrm{S}}{c D_\mathrm{L} D_\mathrm{LS}} \xi_0^2 \, (1 + z_\mathrm{L}) \, \omega \, , \tag{2.19}$$

as well as the dimensionless time delay

$$T(\mathbf{x}, \mathbf{y}) \equiv \frac{c D_\mathrm{L} D_\mathrm{LS}}{D_\mathrm{S} \xi_0^2 (1 + z_\mathrm{L})} \, t_\mathrm{d} \left(\xi_0 \mathbf{x}, \boldsymbol{\eta}(\mathbf{y}) \right) = \frac{1}{2} |\mathbf{x} - \mathbf{y}|^2 - \Psi(\mathbf{x}) + \phi_m(\mathbf{y}) \, , \tag{2.20}$$

where

$$\Psi(\mathbf{x}) = \frac{D_\mathrm{L} D_\mathrm{LS}}{D_\mathrm{S} \xi_0^2} \hat{\Psi}(\xi_0 \mathbf{x}) \, , \tag{2.21}$$

is the *scaled deflection potential* or the *lensing potential*, and ϕ_m is the dimensionless counterpart of $\hat{\phi}_m$ given by $\phi_m(\mathbf{y}) = (D_\mathrm{L} D_\mathrm{LS} / D_\mathrm{S}) \xi_0^{-2} \hat{\phi}_m(\boldsymbol{\eta}(\mathbf{y}))$. In terms of these dimensionless quantities, the magnification function now becomes

$$\mathcal{F}(w, \mathbf{y}) = \frac{w}{2\pi i} \int d^2\mathbf{x} \exp \left[i w T(\mathbf{x}, \mathbf{y}) \right] \, . \tag{2.22}$$

The frequency-domain lensed GW waveform, $\widetilde{h}^\mathrm{L}$, can then be obtained from the unlensed waveform, $\widetilde{h}$, as (see, Eqs. (2.12) and (2.7))

$$\widetilde{h}^\mathrm{L}_{\mu\nu}(\omega, \mathbf{y}) = \mathcal{F} \left(\omega(w) \, , \mathbf{y} \right) \times \widetilde{h}_{\mu\nu}(\omega) \, . \tag{2.23}$$

In the case of axially symmetric lenses, where $\Psi(\mathbf{x})$ depends only on $x = |\mathbf{x}|$, the magnification function can be further simplified and expressed in terms of the Bessel function of zeroth-order, J_0, as [234]

$$\mathcal{F}(w, y) = -iw \, e^{iwy^2/2} \int_0^\infty dx \, x \, J_0(wxy) \exp \left[iw \left(\frac{x^2}{2} - \Psi(x) + \phi_m(y) \right) \right] \tag{2.24}$$

where $y = |\mathbf{y}|$.

Thus, obtaining lensed GW waveforms boils down to computing $\mathcal{F}(w)$ for a given lens model. Closed-form analytic solutions exist only for simple lenses (see Sec. 2.4 for details) while for any general lens configuration, Eqs. (2.22) and (2.24) are computationally expensive. This is primarily due to the integrand being highly oscillatory, particularly for large values of w. In Chapters 3 and 5, we introduce two numerical approaches to efficiently compute $\mathcal{F}(w)$.

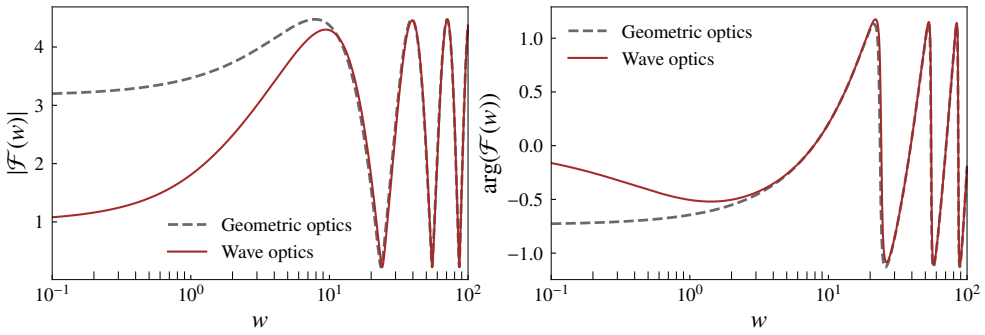

Figure 2.3: *Comparison of magnification function in the full wave-optics and the geometric-optics limit. Lensing is due to a point mass lens with source located at $y = 0.1$.*

2.3 THE GEOMETRIC-OPTICS APPROXIMATION

In the geometric-optics limit, $w \gg 1/T$, the integrand in Eq. (2.22) becomes highly oscillatory. The dominant contribution to $\mathcal{F}(w)$, in this regime, comes from the stationary points of $T(\mathbf{x}, \mathbf{y})$ (see, Eq. (2.20))[7] . These stationary points correspond to *image positions* on the lens plane and can be determined by invoking *Fermat's principle*, which is stated in mathematical form as

[7] $T(\mathbf{x}, \mathbf{y})$ *can be identified as the* Fermat potential.

$$\frac{\partial T(\mathbf{x}, \mathbf{y})}{\partial \mathbf{x}} = 0 \implies \mathbf{y} = \mathbf{x} - \boldsymbol{\alpha}(\mathbf{x}) \,, \tag{2.25}$$

where the *scaled deflection angle* $\boldsymbol{\alpha}$ is given by

$$\boldsymbol{\alpha}(\mathbf{x}) \equiv \frac{D_{\rm L} D_{\rm LS}}{D_{\rm S}\, \xi_0} \hat{\boldsymbol{\alpha}}(\xi_0 \mathbf{x}) = \frac{\partial \Psi(\mathbf{x})}{\partial \mathbf{x}} \,. \tag{2.26}$$

Eq. (2.25) defines the *lens equation* and its solutions $\mathbf{x}(\mathbf{y})$ give the location of the images.

We then expand $T(\mathbf{x}, \mathbf{y})$ in a Taylor series around the j-th image position $\mathbf{x}_j$ as

$$T(\mathbf{x}, \mathbf{y}) = T(\mathbf{x}_j, \mathbf{y}) + \frac{1}{2} \sum_{a,b} \frac{\partial^2 T(\mathbf{x}_j, \mathbf{y})}{\partial x_a \partial x_b} \tilde{x}_a \tilde{x}_b + \mathcal{O}(\tilde{x}^3) \,, \tag{2.27}$$

where $\tilde{\mathbf{x}} = \mathbf{x} - \mathbf{x}_j$ and $a, b = 1, 2$ are indices representing lens plane coordinates x_1, x_2. We assume that all images satisfy $w|\boldsymbol{\partial}^2 T|^3 \gg |\boldsymbol{\partial}^3 T|^2$, $w|\boldsymbol{\partial}^2 T|^2 \gg |\boldsymbol{\partial}^4 T|$, ... and so on. We can then neglect the third and higher order terms in the expansion. Substituting Eq. (2.27) for $T(\mathbf{x}, \mathbf{y})$ in Eq. (2.22), we get

$$\mathcal{F}_{\rm GO}(w, \mathbf{y}) = \sum_j |\mu(\mathbf{x}_j, \mathbf{y})|^{1/2} \exp\left[i w T(\mathbf{x}_j, \mathbf{y}) - i\pi n_j \right] \,, \tag{2.28}$$

where $\mu(\mathbf{x}_j, \mathbf{y})$ is the *magnification* of the j-th image obtained from

$$\mu(\mathbf{x}_j, \mathbf{y}) = \det\left[H(\mathbf{x}_j, \mathbf{y}) \right]^{-1} , \text{ where } H_{ab}(\mathbf{x}_j, \mathbf{y}) = \frac{\partial^2 T(\mathbf{x}_j, \mathbf{y})}{\partial x_a \partial x_b} \tag{2.29}$$

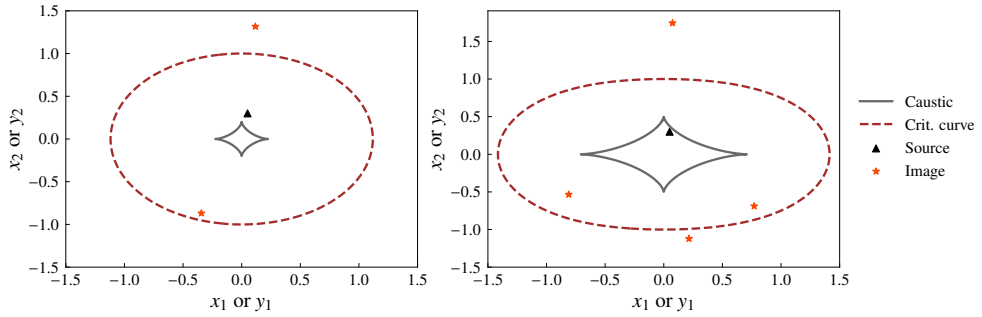

Figure 2.4: *Critical curves (dashed) and caustics (solid) for a point mass lens perturbed by an external shear, $\gamma = 0.1$ (left) and $\gamma = 0.25$ (right).*

is the Hessian matrix of the time delay surface and n_j is the *Morse index* which takes values $0, 1/2$ or 1 depending on whether $\mathbf{x}_j$ is a minimum, saddle or maximum point of $T(\mathbf{x}, \mathbf{y})$, respectively.

Fig. 2.3 compares the amplitude (left panel) and phase (right panel) of the magnification function $\mathcal{F}(w)$ in wave-optics with its geometric-optics approximation $\mathcal{F}_{\rm GO}(w)$. The lens is modeled as a point mass (see Sec. 2.4.1) with the source[8] located at $y = 0.1$. At low frequencies (small w), the geometric-optics approximation breaks down, but it converges to the geometric-optics result as w increases. Corrections to the geometric-optics limit at large w regime (i.e., in powers of $1/w$) can be obtained by including higher order terms in the expansion of the time delay in Eq. (2.27) [278]. In the opposite limit, as $w \to 0$, $\mathcal{F}(w)$ approaches unity. This is because, in this regime, $\lambda_{\rm GW} \ll M_{\rm L}$ and the wave propagates essentially unperturbed by the lens. Corrections to $\mathcal{F}_{\rm GO}(w)$ in the low-w region (i.e., in powers of w) can be obtained by expanding the exponential in powers of $\Psi(\mathbf{x})$ [280].

[8] *For our purposes, we shall always consider the source to be a non-extended or point source.*

In geometric-optics, the magnification map $\mu(\mathbf{x}, \mathbf{y})$ is unbounded when $\det[H(\mathbf{x}, \mathbf{y})] = 0$. The set of points in the lens plane ($\mathbf{x}$-plane) satisfying this condition defines the *critical curve*. The corresponding set of points in the source plane ($\mathbf{y}$-plane), mapped via Eq. (2.25), forms the *caustic*. When a source lies near a caustic, some of its images lie close to a critical curve and exhibit formally infinite magnification. This divergence is an artifact of the geometric-optics approximation. In such cases, the magnification function is decomposed into a diffraction part, from images near critical curves, and a geometric part, from the remaining images.

Fig. 2.4 shows the critical curves (dashed lines) and caustics (solid lines) for a *point mass lens perturbed by an external shear* (see Sec. 2.4.5). The external shear, denoted by γ, models the tidal influence of nearby masses. As γ increases from 0.1 (left panel) to 0.25 (right panel), the diamond-shaped caustic expands and eventually encloses the source. This leads to a transition in the number of images - from two images when the source is outside the caustic to four when it lies within. Thus, caustics delineate regions of different image multiplicity.

2.4 LENS MODELS

In this section, we introduce the lens models relevant for this thesis, namely, isolated point mass lens (PML), point mass lens with charge (PMQ) singular isothermal sphere (SIS), Navarro-Frenk-White lens (NFW) and point mass lens perturbed by external potential (PMX).[9] All models except the last are axially symmetric. For such lenses, the lensing configuration requires that the source and the images lie on the same radial line. Consequently, the lensing behaviour depends only on the scalar source position $y \equiv |\mathbf{y}|$, reducing the problem by one-dimension.

[9] *A catalog of various lens models are available in Keeton [188].*

2.4.1 *Isolated point mass lens*

This is the simplest gravitational lens model that is analytically tractable. Isolated point mass lens (PML) describes stars and compact objects such as black holes, neutron stars and other exotic objects, which have a Schwarzschild spacetime exterior. The Schwarzschild metric in standard spherical coordinates $(t, R, \vartheta, \varphi)$ is given by

$$ds^2 = -\left(1 - \frac{R_s}{R}\right) c^2 dt^2 + \left(1 - \frac{R_s}{R}\right)^{-1} dR^2 + R^2 d\Omega^2 \,, \tag{2.30}$$

where $R_s \equiv 2GM_\mathrm{L}/c^2$ is the Schwarzschild radius of a lens of mass M_L, and $d\Omega^2 \equiv d\vartheta^2 + \sin^2\vartheta d\varphi^2$ is the metric on the 2-sphere. To express the metric in isotropic coordinates $(t, r, \vartheta, \varphi)$ we perform a coordinate transformation defined by

$$R(r) = r\left(1 + \frac{R_s}{4r}\right)^2 \,. \tag{2.31}$$

In these coordinates, the Schwarzschild metric becomes

$$ds^2 = -\left(\frac{1 - R_s/4r}{1 + R_s/4r}\right)^2 c^2 dt^2 + \left(1 + \frac{R_s}{4r}\right)^4 d\mathbf{r}^2 \,, \tag{2.32}$$

where $d\mathbf{r}^2 \equiv dr^2 + r^2 d\Omega^2$. In the weak-field limit, that is, keeping terms only upto $\mathcal{O}(G)$, the isotropic Schwarzschild metric simplifies to

$$ds^2 = -\left(1 - \frac{R_s}{r}\right) c^2 dt^2 + \left(1 + \frac{R_s}{r}\right) d\mathbf{r}^2 + \mathcal{O}(G^2) \,. \tag{2.33}$$

Comparing Eq. (2.33) with Eq. (2.6), we identify the effective Newtonian potential as

$$U(r) = -\frac{GM_\mathrm{L}}{r} = -\frac{GM_\mathrm{L}}{\sqrt{\xi^2 + z^2}} \,, \tag{2.34}$$

where we have written the radial coordinate $r = \sqrt{\xi^2 + z^2}$, with $\boldsymbol{\xi}$ being the transverse position in the lens plane, and $\xi \equiv |\boldsymbol{\xi}|$.

With this potential in hand, the deflection angle can be computed using Eq. (2.15) as[10]

$$\hat{\boldsymbol{\alpha}}(\boldsymbol{\xi}) = -\frac{2GM_{\rm L}}{c^2}\int_{-\infty}^{\infty} dz\, \frac{\partial}{\partial \boldsymbol{\xi}} \frac{1}{\sqrt{\xi^2 + z^2}} = \frac{4GM_{\rm L}}{c^2}\frac{\boldsymbol{\xi}}{\xi^2}\,. \tag{2.35}$$

[10] *This deflection angle predicted by GR in the weak-field is a factor of two larger than that predicted by Newtonian gravity. For a derivation see, e.g., Appendix A of Bartelmann [65]. The full deflection angle in the strong-field of Schwarzschild spacetime is discussed in Weinberg [304].*

Using Eq. (2.26), the scaled deflection angle is then given by

$$\boldsymbol{\alpha}(\mathbf{x}) = \frac{4GM_{\rm L}D_{\rm L}D_{\rm LS}}{c^2 D_{\rm S}\,\xi_0^2}\frac{\mathbf{x}}{x^2} = \frac{\mathbf{x}}{x^2}\,, \tag{2.36}$$

where $x \equiv |\mathbf{x}|$, and in the second equality we have chosen the length scale ξ_0 to be the Einstein radius of the lens,

$$\xi_0 = R_E \equiv \sqrt{\frac{4GM_{\rm L}D_{\rm L}D_{\rm LS}}{c^2 D_{\rm S}}}\,. \tag{2.37}$$

The corresponding lensing potential $\Psi(x)$, related to the scaled deflection angle by Eq. (2.26), is then

$$\Psi(x) = \ln(x)\,. \tag{2.38}$$

As mentioned earlier, for axially symmetric lenses, including PML, all lensing quantities depend only on the radial coordinate, and hence are effectively one-dimensional. The dimensionless time delay map is given by Eq. (2.20) as

$$T(x,y) = \frac{1}{2}(x-y)^2 - \ln(x) + \phi_m(y)\,, \tag{2.39}$$

where

$$\phi_m(y) = \frac{(x_+ - y)^2}{2} - \ln x_+, \text{ with} \tag{2.40a}$$

$$x_+ = \frac{y + \sqrt{y^2+4}}{2}\,, \tag{2.40b}$$

are the arrival time of the global minima image, and its location for a given source position y, respectively. With these ingredients, the integral in Eq. (2.22) for PML can be analytically computed [247] and is given by

$$\begin{aligned}\mathcal{F}(w,y) = &\exp\left[\frac{\pi w}{4} + i\frac{w}{2}\left(\ln\left(\frac{w}{2}\right) - 2\phi_m(y)\right)\right] \\ &\times \Gamma\left(1 - \frac{i}{2}w\right)\, {}_1F_1\left(\frac{i}{2}w, 1; \frac{i}{2}wy^2\right)\,,\end{aligned} \tag{2.41}$$

where Γ denotes the standard gamma function, ${}_1F_1$ is Kummer's confluent hypergeometric function of the first kind. The dimensionless frequency w can be expressed in terms of the redshifted lens mass $M_{\rm Lz} \equiv M_{\rm L}(1+z_{\rm L})$,

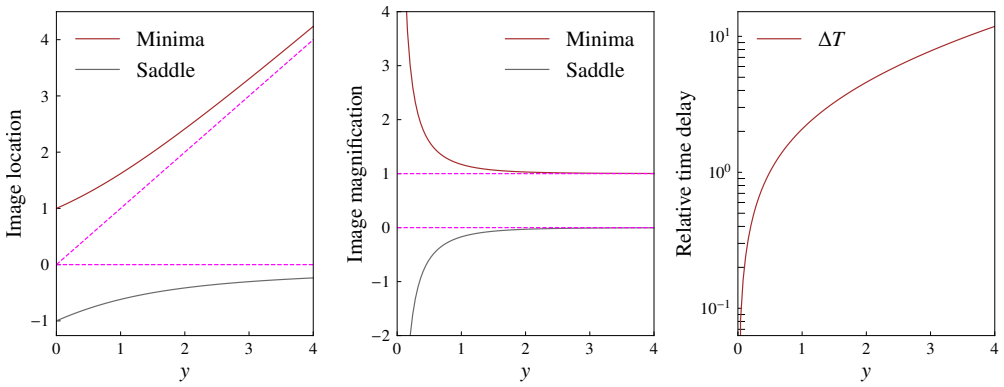

Figure 2.5: *Locations (left), magnifications (center) and the relative time delay between the images (right) as a function of the source location for PML.*

by substituting ξ_0 from Eq. (2.37) into the definition in Eq. (2.19), yielding $w = (4GM_{\rm Lz}/c^3)\,\omega$.

In addition to the minima image at x_+, the lens equation in Eq. (2.25) also gives a saddle image. Solving the one-dimensional lens equation

$$y = x - \frac{1}{x}\,, \tag{2.42}$$

gives the second solution at

$$x_- = \frac{y - \sqrt{y^2+4}}{2}\,. \tag{2.43}$$

As seen from the left panel in Fig. 2.5, the minima image traces the source as it moves away from the lens, while the saddle image moves closer towards the lens. At $y = 0$, the image appears to form a ring of radius $x = 1$, which is known as the *Einstein ring*. The corresponding magnifications of these images with respect to the unlensed signal are obtained using Eq. (2.29) as

$$\mu_\pm = \frac{1}{2} \pm \frac{y^2+2}{2y\sqrt{y^2+4}}\,, \tag{2.44}$$

where μ_+ corresponds to the minima and μ_- to the saddle image. These are plotted on the center panel in Fig. 2.5. As the source moves far away from the lens ($y \to \infty$), the magnifications asymptote to $\mu_+ \to 1$ and $\mu_- \to 0$, indicating that the minima image becomes indistinguishable from the unlensed source, while the saddle image becomes highly demagnified and contributes negligibly to the observed signal. At the Einstein radius ($x = 1$), the magnifications diverge. Thus, it forms a critical curve. The corresponding caustic is at $y = 0$.

The lensing time delay of the saddle image with respect to the minima image can be found to be

$$\Delta T = \frac{1}{2} y\sqrt{y^2+4} + \ln\left(\frac{\sqrt{y^2+4}+y}{\sqrt{y^2+4}-y}\right)\,, \tag{2.45}$$

which is plotted on the right panel in Fig. 2.5.

In the geometric-optics limit, from Eq. (2.28), we have

$$\mathcal{F}_{\rm GO}(w,y) = |\mu_+|^{1/2} - i|\mu_-|^{1/2} \exp\left(iw\Delta T\right) \ . \tag{2.46}$$

The comparison between the wave-optics magnification function (Eq. (2.41)) and the geometric-optics magnification function (Eq. (2.46)) for PML is shown in Fig. 2.3.

2.4.2 *Point mass lens with charge*

In this section, we determine the various lensing quantities associated with a *charged point mass lens* (PMQ). The lens is modeled as a non-rotating, charged compact object described by the Reissner-Nordström (RN) metric, parameterized by its mass $M_{\rm L}$, and charge Q. The spacetime metric in spherical coordinates $(t, R, \vartheta, \varphi)$ is given by

$$ds^2 = -\left(1 - \frac{R_s}{R} + \frac{R_Q^2}{R^2}\right)c^2dt^2 + \left(1 - \frac{R_s}{R} + \frac{R_Q^2}{R^2}\right)^{-1} dR^2 + R^2 d\Omega^2 \ , \tag{2.47}$$

where $d\Omega^2 \equiv d\vartheta^2 + \sin^2\vartheta\, d\varphi^2$ is the element of the solid angle on a 2-sphere, $R_s \equiv GM_{\rm L}/c^2$ is the Schwarzschild radius of the lens, $R_Q \equiv \sqrt{Q^2G/(4\pi\epsilon_0 c^4)}$ is the characteristic length scale associated with the charge term, and ϵ_0 is the permittivity of free space.

To arrive at the metric in isotropic coordinates $(t, r, \vartheta, \varphi)$, we perform the following coordinate transformation

$$R(r) = r\left(1 + \frac{R_s}{2r} - \frac{R_Q^2}{4r^2} + \frac{R_s^2}{16r^2}\right) \ . \tag{2.48}$$

Under this transformation, the RN metric becomes

$$\begin{aligned} ds^2 = &-\left[1 - \left(\frac{R_s}{4r}\right)^2 + \left(\frac{R_Q}{2r}\right)^2\right]^2 \left[\left(1 + \frac{R_s}{4r}\right)^2 - \left(\frac{R_Q}{2r}\right)^2\right]^{-2} c^2dt^2 \\ &+ \left[\left(1 + \frac{R_s}{4r}\right)^2 - \left(\frac{R_Q}{2r}\right)^2\right]^2 d\mathbf{r}^2 \ , \end{aligned} \tag{2.49}$$

where $d\mathbf{r}^2 \equiv dr^2 + r^2 d\Omega^2$. Since, we are interested in the weak-field limit, we expand the factors in the above metric in powers of G and keep terms upto $\mathcal{O}(G)$. This simplifies the isotropic RN metric to

$$ds^2 = -\left(1 - \frac{R_s}{r} + \frac{R_Q^2}{r^2}\right)c^2dt^2 + \left(1 + \frac{R_s}{r} - \frac{R_Q^2}{2r^2}\right)d\mathbf{r}^2 + \mathcal{O}(G^2) \ , \tag{2.50}$$

which is of the form

$$ds^2 = -\left(1+\frac{2V(r)}{c^2}\right)c^2dt^2 + \left(1-\frac{2\widetilde{V}(r)}{c^2}\right)d\mathbf{r}^2 + \mathcal{O}(G^2)\,, \tag{2.51}$$

where

$$V(r) = -\left(\frac{R_s}{r}-\frac{R_Q^2}{r^2}\right)\frac{c^2}{2}, \text{ and } \widetilde{V}(r) = -\left(\frac{R_s}{r}-\frac{R_Q^2}{2r^2}\right)\frac{c^2}{2}\,. \tag{2.52}$$

In order to determine the effective Newtonian potential, we begin by computing the *gravitational refractive index* n, which contains information about the coordinate speed of propagation. For massless particles such as gravitons, the spacetime interval satisfies $ds^2 = 0$. The refractive index in the weak-field isotropic RN metric is then obtained as

$$n \equiv \frac{c}{d\mathbf{r}/dt} = \sqrt{\frac{1-2\widetilde{V}(r)/c^2}{1+2V(r)/c^2}} \approx 1 - \frac{V(r)+\widetilde{V}(r)}{c^2}\,. \tag{2.53}$$

Similarly, the refractive index for the general static weak-field metric in Eq. (2.6) can be computed to get $n \approx 1-(2U/c^2)$. Equating this with Eq. (2.53) gives the effective Newtonian potential as

$$U(r) = \frac{V(r)+\widetilde{V}(r)}{2} = -\frac{GM_{\rm L}}{r} + \frac{3Q^2G}{32\pi\epsilon_0c^2r^2}\,, \tag{2.54}$$

We are now in a position to compute the deflection angle for the PMQ lens. Using Eq (2.15), and plugging $r=\sqrt{\xi^2+z^2}$, the deflection angle is found to be,[11]

$$\hat{\boldsymbol{\alpha}}(\boldsymbol{\xi}) = \left(\frac{4GM_{\rm L}}{c^2\xi} - \frac{3GQ^2}{16\epsilon_0c^4\xi^2}\right)\frac{\boldsymbol{\xi}}{\xi}\,. \tag{2.55}$$

[11] *The weak field deflection angle obtained here, accurate to $\mathcal{O}(G)$, is in agreement with the result of Eiroa, Romero, and Torres [129], who computed the full deflection angle in the strong-field regime.*

The scaled deflection angle is computed using Eq. (2.26) as

$$\begin{aligned}\boldsymbol{\alpha}(\mathbf{x}) &= \frac{4GM_{\rm L}D_{\rm L}D_{\rm LS}}{c^2D_{\rm S}\xi_0^2}\left[\frac{1}{x} - \frac{3Q^2}{64\epsilon_0c^2\xi_0M_{\rm L}}\frac{1}{x^2}\right]\frac{\mathbf{x}}{x}\\ \implies \boldsymbol{\alpha}(\mathbf{x}) &= \frac{\mathbf{x}}{x^2} - \widetilde{Q}\frac{\mathbf{x}}{x^3}\,.\end{aligned} \tag{2.56}$$

where we set ξ_0 to be the Einstein radius of the PML as given in Eq.(2.37), and introduce the dimensionless *effective charge*

$$\widetilde{Q} \equiv \frac{3Q^2}{64\epsilon_0c^2\xi_0M_{\rm L}}\,. \tag{2.57}$$

The first term in Eq. (2.56) can be identified with the PML result (Eq. (2.36)) and the second term is the correction due to the presence of the charge

parameter Q. Note that the effect of the charge is suppressed by the Einstein radius ξ_0.

Using the two-dimensional deflection angle, the corresponding lensing potential, Ψ is obtained from Eq. (2.26) as

$$\Psi(x) = \ln(x) + \frac{\widetilde{Q}}{x} \,. \tag{2.58}$$

The lensing potential depends only on the radial coordinate $x \equiv |\mathbf{x}|$ on the lens plane, reflecting the axial symmetry of the system. As expected, in the limit $\widetilde{Q} \to 0$, we reproduce the PML results.

The image locations can be obtained by solving the lens equation given in Eq. (2.25). For PMQ lens, this becomes

$$\mathbf{y} = \mathbf{x} - \left(1 - \frac{\widetilde{Q}}{x}\right) \frac{\mathbf{x}}{x^2} \,. \tag{2.59}$$

Chapter 3 provides further details about the image locations. Unlike PML, PMQ doesn't have a closed-form expression for the magnification function, which necessitates its numerical evaluation.

2.4.3 *Singular isothermal sphere*

The *singular isothermal sphere* (SIS) is a widely used model for the mass distribution of galaxies acting as gravitational lenses. It assumes a spherically symmetric system in which the constituent particles (e.g., stars or dark matter) behave like an ideal gas in thermal and hydrostatic equilibrium, and follow an isotropic, Maxwellian velocity distribution. The resulting mass density profile falls off as [235]

$$\rho(r) = \frac{\sigma_v^2}{2\pi G r^2} \,, \tag{2.60}$$

where σ_v is the one-dimensional velocity dispersion along the line of sight and r is the distance from the center of the lens. Since, $\rho(r) \propto r^{-2}$, mass $M(r) \propto r$, which gives the rotational velocity of test particles in circular orbits as

$$v_{\rm rot}^2(r) = \frac{GM(r)}{r} = 2\sigma_v^2 \,, \tag{2.61}$$

which is a constant. Therefore, although the density profile is singular at $r = 0$, it is remarkable in reproducing the flat rotation curves of spiral galaxies, and hence is thought to be a good model for galaxy lenses.

The Newtonian potential for the SIS model can be obtained by solving the *Poisson's equation*

$$\nabla^2 U(\mathbf{r}) = 4\pi G\rho(\mathbf{r}) \implies \frac{1}{r^2}\frac{\partial}{\partial r}\left(r^2\frac{\partial U(r)}{\partial r}\right) = \frac{2\sigma_v^2}{r^2} \tag{2.62a}$$

$$\implies U(r) = 2\sigma_v^2 \ln\left(\frac{r}{r_0}\right) , \tag{2.62b}$$

where r_0 is an arbitrary reference radius.

We can obtain the two-dimensional projected surface mass density by integrating the three-dimensional density profile, given in Eq. (2.60), along the line of sight, z, giving

$$\Sigma(\xi) = 2\int_0^\infty \rho\left(\sqrt{\xi^2+z^2}\right) dz = \frac{\sigma_v^2}{2G\xi} \tag{2.63a}$$

$$\implies \Sigma(x) = \frac{\sigma_v^2}{2G\xi_0 x} , \tag{2.63b}$$

where we have used $x = \xi/\xi_0$.

The length scale ξ_0 can be chosen as the Einstein radius for SIS

$$\xi_0 = R_E = 4\pi\left(\frac{\sigma_v}{c}\right)^2 \frac{D_\mathrm{L} D_\mathrm{LS}}{D_\mathrm{S}} . \tag{2.64}$$

With this choice, and defining the critical surface mass density as

$$\Sigma_\mathrm{cr} \equiv \frac{c^2}{4\pi G}\frac{D_\mathrm{S}}{D_\mathrm{L} D_\mathrm{LS}} , \tag{2.65}$$

the surface mass density in Eq. (2.63) becomes

$$\Sigma(x) = \frac{1}{2x}\Sigma_\mathrm{cr} . \tag{2.66}$$

The dimensionless surface mass density or the *convergence* can then be obtained as

$$\kappa(x) \equiv \frac{\Sigma(x)}{\Sigma_\mathrm{cr}} = \frac{1}{2x} . \tag{2.67}$$

We define the characteristic mass scale of the SIS lens as the mass contained within ξ_0, and is given by

$$M_\mathrm{L} = \frac{4\pi^2\sigma_v^4}{c^2 G}\frac{D_\mathrm{L} D_\mathrm{LS}}{D_\mathrm{S}} . \tag{2.68}$$

The deflection angle for the SIS lens can be computed using Eq. (2.15):

$$\hat{\boldsymbol{\alpha}}(\boldsymbol{\xi}) = 4\pi\left(\frac{\sigma_v}{c}\right)^2 \frac{\boldsymbol{\xi}}{\xi} . \tag{2.69}$$

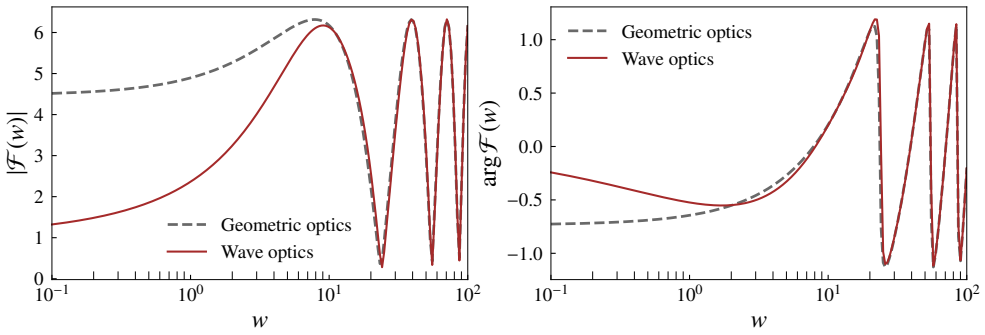

Figure 2.6: *Comparison of magnification function in the full wave-optics and the geometric-optics limit for a singular isothermal sphere lens with source located at* $y = 0.1$.

The scaled deflection angle from Eq. (2.26) is then

$$\boldsymbol{\alpha}(\mathbf{x}) = \frac{\mathbf{x}}{x} , \tag{2.70}$$

and the lensing potential is

$$\Psi(x) = x . \tag{2.71}$$

The lens equation for the SIS model is then

$$y = x - \frac{x}{|x|} , \tag{2.72}$$

which, for $y < 1$, yields two images - a minima image at $x_+ = y + 1$ and a saddle image at $x_- = y - 1$. For $y \geq 1$, only one image exists at $x_+ = y + 1$. The corresponding magnifications are

$$\mu_\pm = 1 \pm \frac{1}{y}, \tag{2.73}$$

where μ_- exists only for $y < 1$. In this region, the two images arrive at a time delay of

$$\Delta T = T(x_-, y) - T(x_+, y) = 2y , \tag{2.74}$$

in dimensionless units. The corresponding dimensionless frequency is obtained from Eqs. (2.19), (2.64) and (2.68) as

$$w = \left(4\pi \frac{\sigma_v^2}{c^2}\right)^2 \frac{D_\mathrm{L} D_\mathrm{LS}}{D_\mathrm{S}} (1 + z_\mathrm{L}) \frac{\omega}{c} = \frac{4GM_\mathrm{Lz}}{c^3} \omega . \tag{2.75}$$

With this, in the geometric-optics limit, the magnification function can be written as

$$\mathcal{F}_\mathrm{GO}(w, y) = \begin{cases} |\mu_+|^{1/2} - i|\mu_-|^{1/2} \exp\left[iw\Delta T\right], & y < 1 \\ |\mu_+|^{1/2}, & y \geq 1 \end{cases} \tag{2.76}$$

In the wave-optics regime, the magnification function for the SIS lens can be expressed as a series expansion [217]:

$$\mathcal{F}(w,y) = \exp\left(\frac{i}{2}wy^2\right)\sum_{n=0}^{\infty}\frac{1}{n!}\Gamma\left(1+\frac{n}{2}\right)(2w)^{n/2} \times \exp\left(\frac{3\pi i n}{4}\right)\,{}_1F_1\left(1+\frac{n}{2},1;-\frac{i}{2}wy^2\right)\,. \tag{2.77}$$

Here, Γ is the gamma function and ${}_1F_1$ is the confluent hypergeometric function of the first kind. Fig. 2.6 shows the comparison between the magnification functions evaluated using the wave-optics series expansion truncated at $n = 200$ terms, with that obtained from the geometric-optics approximation.

2.4.4 *Navarro-Frenk-White lens*

The *Navarro-Frenk-White* (NFW) profile is a model for describing the density distribution of dark matter halos, as inferred from large-scale cosmological N-body simulations [237, 238]. Unlike the SIS model, which assumes a singular r^{-2} density profile, the NFW profile captures the gradual transition from a steep inner cusp to a shallower outer slope, providing a more realistic description of dark matter halos that act as gravitational lenses.

The three-dimensional density profile of the NFW halo is given by

$$\rho(r) = \frac{\rho_s}{(r/r_s)\,(1+r/r_s)^2}\,, \tag{2.78}$$

where r is the radial distance from the halo center, r_s is the scale radius, and ρ_s is the characteristic density. The total mass diverges logarithmically at large radii, so the profile is typically truncated at the radius r_{200}, defined as the radius within which the mean density is 200 times the critical density of the Universe.

Setting $x = \xi/r_s$, the projected surface mass density can be found from $\rho(r)$ as [64]

$$\Sigma(x) = 2\int_0^{\infty}\rho(\sqrt{\xi^2+z^2})dz = \frac{2\rho_s r_s}{x^2-1}f(x)\,, \tag{2.79}$$

where

$$f(x) = \begin{cases} 1-\frac{2}{\sqrt{1-x^2}}\operatorname{arctanh}\sqrt{\frac{1-x}{1+x}}, & x<1 \\ 1-\frac{2}{\sqrt{x^2-1}}\arctan\sqrt{\frac{x-1}{x+1}}, & x>1 \\ 0, & x=1 \end{cases} \tag{2.80}$$

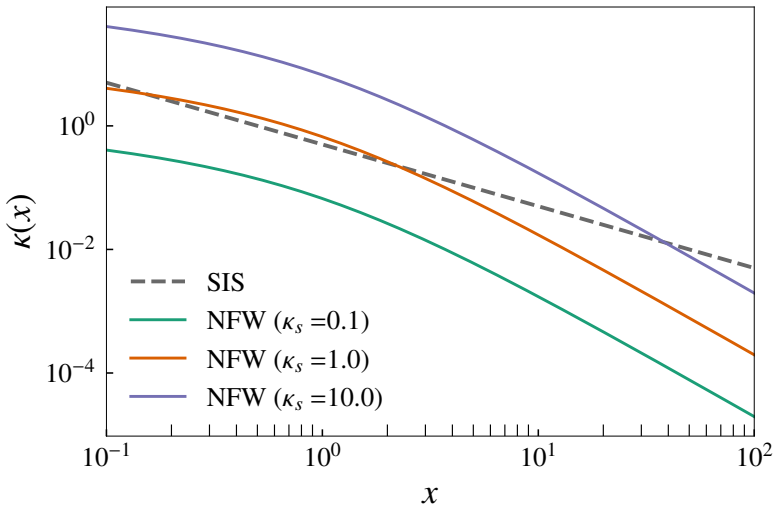

Figure 2.7: *Convergence κ as a function of the dimensionless radial coordinate x in the lens plane for SIS and NFW lenses.*

Introducing the dimensionless normalization parameter $\kappa_s \equiv \rho_s r_s / \Sigma_{\rm cr}$, the convergence for an NFW profile takes the form

$$\kappa(x) = 2\kappa_s \frac{f(x)}{x^2 - 1}\,, \tag{2.81}$$

where $\Sigma_{\rm cr}$ is the critical surface mass density defined in Eq. (2.65). Fig. 2.7 illustrates a comparison of the convergence profiles for the SIS and NFW models over a range of κ_s values. The distinct radial behavior reflects the inherent difference in their three-dimensional mass density slopes.

In this thesis, the NFW profile will not be treated as a lensing potential itself but rather as a macroscopic mass distribution from which microlens populations are sampled (see Chapter 4 for further details).

2.4.5 *Point mass lens perturbed by external potential*

In realistic astrophysical scenarios, a point mass lens (such as a compact object) is rarely truly isolated. Instead, it is often embedded within a larger-scale mass distribution, such as a galaxy or a cluster, which can exert additional tidal forces and contribute a smoothly varying gravitational potential. To account for these environmental effects, the lensing potential is commonly augmented by including a constant external shear, γ, and a uniform convergence, κ.

The external shear $\gamma = (\gamma_1, \gamma_2)$ characterizes the quadrupolar tidal gravitational field due to the external mass distribution, while the convergence κ respresents the local isotropic modification to the projected mass density. The external potential can be written as a Taylor expansion about the position of the PML [70, 99, 191]:

$$\Psi_{\rm ext}(\mathbf{x}) = \Psi_0 + \mathbf{a}\cdot\mathbf{x} + \frac{1}{2}\kappa x^2 + \frac{1}{2}\gamma_1(x_1^2 - x_2^2) + \gamma_2 x_1 x_2 + \mathcal{O}(x^3) \tag{2.82}$$

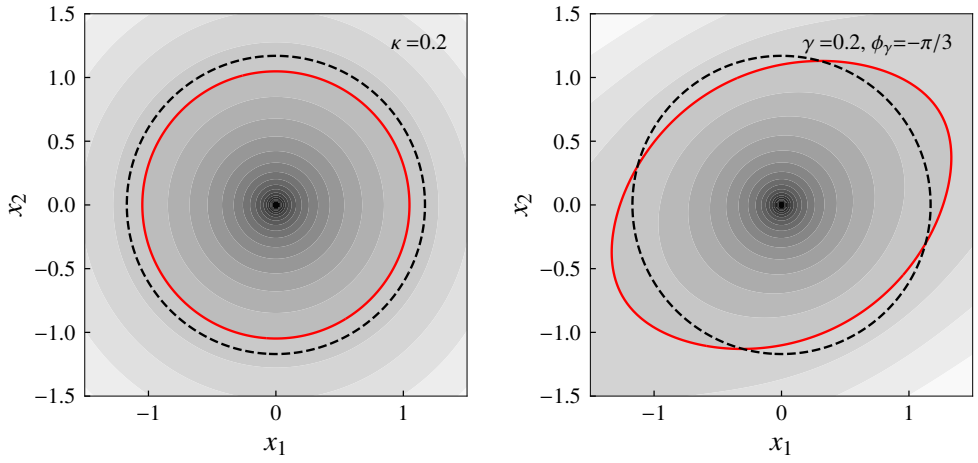

Figure 2.8: *Effects of external convergence κ and shear γ on the lensing potential of a PML. The dashed black line denotes a reference isopotential contour of the PML, while the red lines show corresponding isocontours in the presence of κ (left) or γ (right).*

where Ψ_0 is a constant (irrelevant for lensing observables), and $\mathbf{a}$ is a constant vector which can be absorbed into a redefinition of the source position. The quadratic terms represent the lowest-order nontrivial effects. The shear vector $\boldsymbol{\gamma}$ can be equivalently written in terms of its magnitude $\gamma = \sqrt{\gamma_1^2 + \gamma_2^2}$ and orientation φ_γ as $\gamma_1 = \gamma \cos 2\varphi_\gamma$, $\gamma_2 = \gamma \sin 2\varphi_\gamma$. The total lensing potential for the *point mass in an external perturbation* (PMX) then reads

$$\Psi(\mathbf{x}) = \ln(x) + \frac{1}{2}\kappa x^2 + \frac{1}{2}\gamma \cos 2\varphi_\gamma (x_1^2 - x_2^2) + \gamma \sin 2\varphi_\gamma x_1 x_2 \,. \tag{2.83}$$

Lens equation for this model becomes

$$\mathbf{y} = \mathbf{x} - \frac{\mathbf{x}}{x^2} - \kappa \mathbf{x} - \boldsymbol{\Gamma} \cdot \mathbf{x} \tag{2.84}$$

where $\boldsymbol{\Gamma}$ is the shear matrix defined as

$$\boldsymbol{\Gamma} = \gamma \begin{pmatrix} \cos 2\varphi_\gamma & \sin 2\varphi_\gamma \\ \sin 2\varphi_\gamma & -\cos 2\varphi_\gamma \end{pmatrix} \tag{2.85}$$

Fig. 2.8 illustrates the influence of κ and γ on the lensing potential of a PML. In the left panel, increasing κ induces an isotropic compression of the potential contours, effectively enhancing the focusing strength of the lens. In contrast, the right panel shows that the shear γ introduces anisotropic distortions, stretching the potential along specific axes determined by the shear orientation. The dashed black line denotes a reference isopotential contour of the isolated PML, while the red lines show the corresponding isocontours in the presence of κ or γ, highlighting the deformation.

The constant convergence and shear approximation is valid when the scale of variation of the external mass distribution is much larger than the typical Fresnel zone radius of the PML, which is of the order $\sim R_E/\sqrt{w}$ [311], where R_E is the Einstein radius of the lens and w is the dimensionless frequency.

Table 2.1 summarizes the analytic forms of the lensing potentials $\Psi(\mathbf{x})$ for the lens models discussed in this Chapter. These potentials determine the deflection and time delay properties of each lens, and serve as the key input for computing the lensing magnification function in both wave- and geometric-optics regimes.

LENS MODEL	LENSING POTENTIAL	RELEVANT CHAPTER(S)
PML	$\ln(x)$	Chapters 3, 4 & 5
PMQ	$\ln(x) + \frac{\widetilde{Q}}{x}$	Chapter 3
SIS	x	Chapters 4 & 5
PMX	$\ln(x) + \frac{1}{2}\kappa x^2 + \frac{1}{2}\gamma_1(x_1^2 - x_2^2) + \gamma_2 x_1 x_2$	Chapter 4

Table 2.1: *Summary of lensing potentials corresponding to different lens models with references to the chapters where each model is applied.*

3

PROBING THE CHARGE OF COMPACT OBJECTS USING MICROLENSING

Microlensing produces characteristic frequency-dependent modulations in the unlensed GW signal (see, e.g., Fig. 2.1). These diffraction signatures can potentially be used to probe the properties of the compact object acting as the lens. Most existing searches for microlensing signatures in GW events assume a point mass lens (PML) model [36, 66, 160], where the observed modulations depend solely on the (redshifted) mass of the lens and the source position (see Sec. 2.4.1). However, if the compact object possesses additional properties (or "hairs"), such as electric charge, these features will also imprint themselves on the lensed GW waveform, potentially leading to observable deviations from the standard PML predictions.

Beyond mass, the most natural additional property for a static, spherically symmetric compact object is the EM charge Q. The presence of charge modifies the spacetime metric at order $\mathcal{O}(\mathbb{Q}/r^2)$, where $\mathbb{Q} \equiv Q^2$ (see Sec. 2.4.2). Although astrophysical compact objects are generally expected to be electrically neutral due to efficient charge neutralization and screening processes [82, 125, 139, 251], similar charge-like corrections to the metric can arise in several well-motivated extensions of GR. Notable examples include braneworld scenarios, $f(T)$ gravity, Einstein-Gauss-Bonnet gravity, and certain scalar-tensor theories such as Horndeski gravity [46, 52, 53, 63, 118, 163, 206, 271]. In these contexts, the effective "charge" parameter may not correspond to EM charge, but instead encodes new gravitational degrees of freedom or couplings.

In this Chapter, we investigate the prospects for constraining the effective charge parameter of astrophysical compact objects via GW microlensing observations. We model the spacetime exterior to the lens as a static, spherically symmetric geometry described by a Reissner–Nordström (RN) metric, which incorporates a charge-like parameter $\mathbb{Q}$ in addition to the mass $M_{\rm L}$. We analyze how a nonzero charge modifies the lensing potential, introducing corrections at order $\mathcal{O}(\widetilde{Q}/x)$, as detailed in Eq. (2.58). The dimensionless effective charge parameter, $\widetilde{Q} \propto \mathbb{Q}/(\xi_0 M_{\rm L})$, is defined in terms of the lens mass $M_{\rm L}$ and the Einstein radius $\xi_0 = R_E$ (see Eqs. (2.57) and (2.37)). We numerically compute the resulting frequency-dependent magnification function, $\mathcal{F}(f)$, for a range

of lens masses, source positions, and values of $\widetilde{Q}$, thereby quantifying the impact of charge on the microlensed GW waveform.

To assess the detectability and measurability of the effective charge parameter $\widetilde{Q}$, we quantify the distinguishability between two microlensed GW signals: one corresponding to a true charge $\widetilde{Q}_{\rm tr}$ and another to a trial value $\widetilde{Q}$. This is achieved by computing the *match*, defined as the normalized, noise-weighted inner product between the two waveforms, where the weighting is determined by the detector's power spectral density (PSD). The match serves as a proxy for the statistical distinguishability of the two signals in the presence of detector noise. By evaluating the match across a range of $\widetilde{Q}$ values, we construct an approximate likelihood function over the lens parameters, thereby enabling a quantitative parameter estimation of $\widetilde{Q}$.

The remainder of this Chapter is organized as follows. In Sec. 3.1, we review several beyond-GR theories that predict RN-like metric. Sec. 3.2 analyzes the modifications to the lensing time delay and image properties induced by a nonzero charge parameter. In Sec. 3.3, we present the numerical method for computing the frequency-dependent magnification function and the resulting lensed GW waveform. Sec. 3.4 discusses the prospects for constraining the effective charge parameter through GW microlensing observations, based on simulated signals and projected detector sensitivities. Finally, Sec. 3.5 summarizes our main findings and outlines potential directions for future work.

3.1 EMERGENCE OF CHARGE IN MODIFIED GRAVITY

In this section, we review several well-motivated extensions of GR that predict the appearance of a nonzero effective charge in the spacetime metric, even in the absence of EM charge. Notable examples include:

- **Braneworld gravity:** In these models, our universe is a four-dimensional hypersurface (the "brane") embedded in a higher-dimensional spacetime. The effective gravitational field equations on the brane take the form [118, 271]

$$G_{\mu\nu} + E_{\mu\nu} = 0 \,, \tag{3.1}$$

  where $G_{\mu\nu}$ is the four-dimensional Einstein tensor and $E_{\mu\nu}$ is the projection of the five-dimensional Weyl tensor onto the brane. Due to the traceless property of $E_{\mu\nu}$, the resulting static, spherically symmetric solution has the form $-g_{tt} = g^{RR} = 1 - (2M_{\rm L}/R) - \left(|\mathbb{Q}|/R^2\right)$, with $\mathbb{Q} < 0$. This differs from the standard RN solution by the sign of the charge term [46, 163, 206].

- **Einstein–Gauss–Bonnet gravity:** In higher-dimensional spacetimes, this theory also admits RN-like solutions with a *negative* effective charge term ($\mathcal{Q} < 0$), where the charge originates from the Gauss–Bonnet coupling constant [206].
- **$f(T)$ gravity:** Modifications to GR involving torsion can yield similar metric structures, but with a *positive* effective charge term ($\mathcal{Q} > 0$) [88].
- **Horndeski gravity:** Certain subclasses of Horndeski theories, which include non-minimal couplings between scalar fields, gravity, and matter, also lead to RN-like metrics with a *positive* effective charge [53]. The magnitude of the charge depend on the specific coupling parameters.

In summary, a positive effective charge in the metric can arise from (a) standard EM charge, (b) $f(T)$ gravity, or (c) scalar-tensor couplings as in Horndeski theories. Negative charge terms typically originate from higher-dimensional scenarios, such as braneworld models or Einstein–Gauss–Bonnet gravity. The ubiquity of RN-like metrics in these diverse contexts makes the charged lens an ideal probe for testing both standard and exotic physics with microlensed GWs.

The possibility of measuring $\widetilde{Q}$ have been extensively studied in various astrophysical and gravitational contexts, including: (a) weak-field tests in the Solar System [73, 88, 95, 172, 229], (b) EM signatures from accreting black holes (BHs) [56, 58, 215, 276], (c) GW observations from binary mergers [50, 61, 93, 94, 97, 156, 159, 222, 223, 286], and (d) strong-field lensing and BH shadow measurements [57, 59, 96, 291].

Our results show that, if the lens is actually neutral, microlensing observations can constrain the effective charge parameter to $|\widetilde{Q}| \lesssim 10^{-3}$. For typical astrophysical configurations, the Einstein radius scales as $\xi_0 \sim (M_\mathrm{L} D_\mathrm{L})^{1/2}$, where D_L is the angular diameter distance to the lens. This leads to a constraint on the dimensionless charge: $\mathcal{Q}/M_\mathrm{L}^2 \lesssim \mathcal{O}(10^{-3}\sqrt{D_\mathrm{L}/M_\mathrm{L}})$. While these bounds are much weaker than the extremal limit for a charged BH ($\mathcal{Q}/M_\mathrm{L}^2 = 1$), they can still rule out certain exotic compact objects (such as naked singularities) and place meaningful limits on alternative gravity theories that predict large values of $\mathcal{Q}$.

3.2 LENS MAPPING FOR THE CHARGED LENS

The lensing potential for a charged lens is given in Eq. (2.58), leading to the following dimensionless time delay:

$$T(x,y) = \frac{(x-y)^2}{2} - \ln(x) - \frac{\widetilde{Q}}{x}\,, \tag{3.2}$$

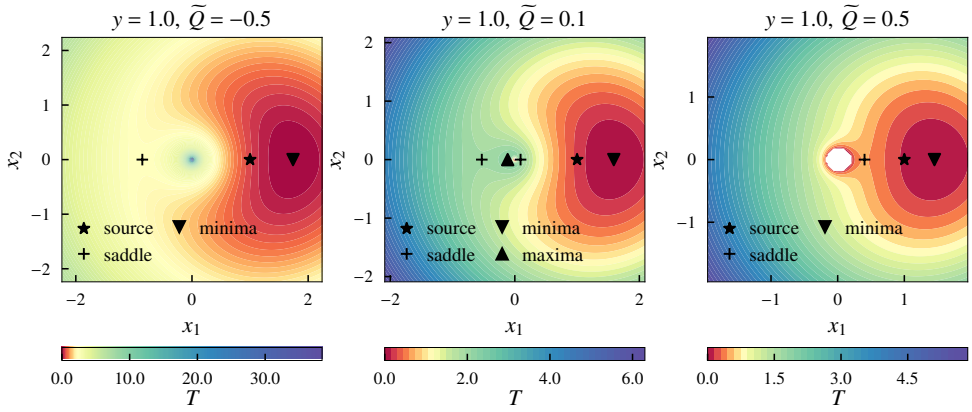

Figure 3.1: *Contours of the time delay T (in units of $4GM_{\rm Lz}/c^3$, with $T = 0$ at the global minimum) as a function of the lens plane coordinates (x_1, x_2).*

where ϕ_m is omitted, since the minimum time delay can be determined numerically.

To restore physical units, we express the dimensional time delay using the Einstein radius (see Eq. (2.20)):

$$t_{\rm d}(x,y) = \frac{D_{\rm S}\,\xi_0^2\,(1+z_{\rm L})}{c\,D_{\rm L}\,D_{\rm LS}}\,T\,(x,y) = \frac{4GM_{\rm Lz}}{c^3}\,T\,(x,y)\ , \tag{3.3}$$

where $M_{\rm Lz} \equiv M_{\rm L}(1+z_{\rm L})$ is the redshifted lens mass.

Figure 3.1 displays contours of the dimensionless time delay $T(x,y)$ on the lens plane, with coordinates x_1 and x_2, for a fixed source position y. The left, center, and right panels correspond to $\widetilde{Q} = -0.5$, 0.1, and 0.5, respectively. For each case, the image locations and their types are indicated. The image positions are determined by solving the lens equation (Eq. (2.59)) for $\mathbf{x}$[1] . Due to axial symmetry, this reduces to a one-dimensional problem, which can be solved using standard root-finding algorithms.

For $\widetilde{Q} \leq 0$, the lens equation yields two solutions: one corresponding to a saddle point image and the other to a minima image, as shown in the left panel of Fig. 3.1. Interestingly, for certain positive values of $\widetilde{Q}$ and source positions y, the lens equation can have up to four solutions, resulting in four images, including a maxima image. This behavior is illustrated in Fig. 3.2 and the middle panel of Fig. 3.1. For sufficiently large $\widetilde{Q}$, no images are formed, as the images are located directly behind the lens and become unresolvable.

The occurrence of multiple images can be understood in terms of caustics in the lensing potential. For $\widetilde{Q} \leq 0$, there are no caustics (except at the lens location), so two images always form. For $\widetilde{Q} > 0$, a caustic appears at a finite value of y, which decreases as $\widetilde{Q}$ increases. If $\widetilde{Q}$ is small enough, the source can lie within the caustic, producing four images. As $\widetilde{Q}$ increases further, the caustic moves to smaller y, and for sufficiently large $\widetilde{Q}$, the caustic shrinks to $y \sim 0$, so the source lies outside the caustic and only two images are produced. For even larger $\widetilde{Q}$, the images become unresolvable. This is demonstrated in Fig. 3.2.

[1] *This setup differs from the black hole shadow analyses in the strong-field regime, though our results reproduce their weak-field limit [129–131].*

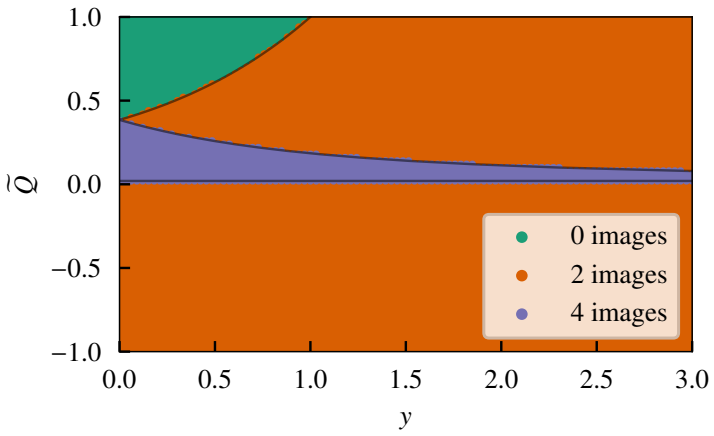

Figure 3.2: *Number of images as a function of the source position and the effective charge. There are always two images for $\widetilde{Q} \leq 0$. For $\widetilde{Q} > 0$, there can be zero, two, or four images, depending on the source position and charge.*

3.3 COMPUTING THE MAGNIFICATION FUNCTION

In this section, we describe how to compute the magnification function for a charged lens and analyze its impact on the lensed GW waveform. Unlike the PML, the charged lens does not admit a closed-form analytical expression for the magnification function. As a result, we must rely on numerical methods to evaluate the relevant diffraction integral.

Direct numerical integration of Eq. (2.22) is challenging due to the highly oscillatory nature of the integrand, which renders standard quadrature techniques both computationally expensive and potentially inaccurate. To address this, we have developed a new numerical scheme that is both efficient and robust, enabling accurate computation of the magnification function even in complex lensing scenarios.[2] Our approach builds upon the methods used in Diego et al. [121], which themselves are extensions of the foundational work by Ulmer and Goodman [289].

[2] *Earlier studies have relied on methods like Levin's algorithm [158, 228], Picard-Lefschetz theory [138, 184], and FFT-convolution [155], which have been validated primarily for simple lensing configurations.*

Below, we outline the key steps of our numerical procedure for computing the frequency-dependent magnification function in the presence of a charged lens. The new ingredient is the use of a histogram-based approach to efficiently evaluate the diffraction integral in time domain.

1. *Time-domain magnification function*: As mentioned, direct computation of $\mathcal{F}(w)$ requires evaluating a highly oscillatory integral, which is numerically challenging. To circumvent this, we instead compute the *time-domain magnification function* $\widetilde{\mathcal{F}}(t)$ defined in terms of the Fourier transform as:

$$\widetilde{\mathcal{F}}(t) \equiv \frac{1}{2\pi} \int_{-\infty}^{\infty} dw \frac{2\pi i}{w} \mathcal{F}(w) \exp\left[-iwt\right] \tag{3.4a}$$

$$= \int d\mathbf{x} \int_{-\infty}^{\infty} \frac{dw}{2\pi} \exp\left[iw\left(T(\mathbf{x}) - t\right)\right] \tag{3.4b}$$

$$= \int d\mathbf{x}\, \delta\left[T(\mathbf{x}) - t\right] \ . \tag{3.4c}$$

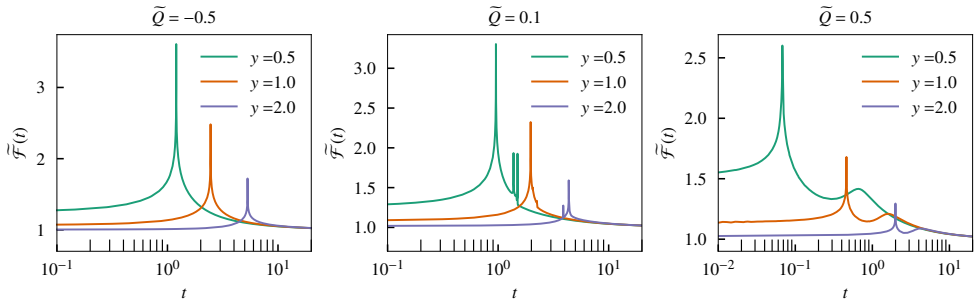

Figure 3.3: *The time-domain magnification function $\widetilde{\mathcal{F}}(t)$ as a function of t (in units of $4GM_{\rm Lz}/c^3$, where the global minima lies at $t = 0$).*

Physically, $d\widetilde{\mathcal{F}}(t)/dt$ represents the lensed response of a delta-function pulse emitted by a point source. For a given time t and a source location $\mathbf{y}$, the set of lens-plane positions satisfying $T(\mathbf{x}) = t$ forms a closed contour. The area enclosed between contours at t and $t + dt$ gives the contribution to $\widetilde{\mathcal{F}}(t)\, dt$. This leads to an intuitive expression,

$$\widetilde{\mathcal{F}}(t) = \frac{dS}{dt}\,, \tag{3.5}$$

where dS is the area between adjacent time delay contours. Thus, by measuring how the area between two infinitesimal closed time delay contours changes with t, we can determine the magnification function $\widetilde{\mathcal{F}}(t)$.

2. *Histogram of the time delay map*: To find the area between the contours of constant time delay, we place a uniform grid over the lens plane and evaluate the time delay function, given in Eq. (3.2), at each grid point (see, e.g., Fig. 3.1 for an illustration of the time delay surfaces). The resulting distribution of time delay values is then binned into a histogram. The height of each histogram bin is proportional to the area between t and $t + dt$, with dt being the bin width. After normalization, this histogram gives the time-domain magnification function $\widetilde{\mathcal{F}}(t)$, with two conventions:

   - The global minimum of the time delay is shifted to $t = 0$, and
   - $\widetilde{\mathcal{F}}(t)$ asymptotically approaches 1 as $t \to \infty$

   This histogram-based method efficiently captures both smooth and singular features in $\widetilde{\mathcal{F}}(t)$.

   Fig. 3.3 shows the time-domain magnification function computed for a charged lens. The panels from left to right correspond to cases with $\widetilde{Q} = -0.5, 0.1$ and 0.5, respectively. Within each panel, curves for source position values $y = 0.5, 1.0$ and 2.0 are shown.

   The structure of $\widetilde{\mathcal{F}}(t)$ reflects the nature and number of images:

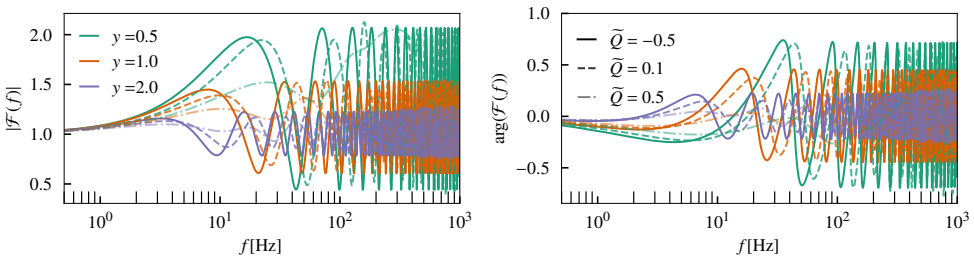

Figure 3.4: *Amplitude and phase of $\mathcal{F}(f)$ for a $500M_\odot$ lens at $z_L = 0.5$, with varying $\widetilde{Q}$ (lines) and y (colors).*

- *logarithmic peaks* in $\widetilde{\mathcal{F}}(t)$ arise from saddle point images, where the corresponding t gives their time delay relative to the global minimum image.
- *Step-like discontinuities* are associated with local minima or maxima images.

Assuming that the source is not exactly at the caustic, the analytic contribution from these singular features is given by [289]

$$\widetilde{\mathcal{F}}_{\rm singular}(t) = 2\pi \sum_{n_j=0,1} (-1)^{n_j}\, \mu_j^{1/2} \mathbb{H}(t-T_j) - 2 \sum_{n_j=1/2} |\mu_j|^{1/2} \ln|t-T_j| \,, \tag{3.6}$$

where n_j is the morse index of the j-th image (0 for minima, 1/2 for saddle, and 1 for maxima), μ_j is the corresponding magnification of the image, T_j is the image's time delay and $\mathbb{H}$ is the Heaviside step function.

In the left and right panels of Fig. 3.3, we always observe two images – a minima and a saddle image. In the middle panel ($\widetilde{Q} = 0.1$), for $y = 0.5$, there are four images - a global minima, two saddle images and a maxima image, which can clearly be identified from the multiple discontinuities. For larger y, the number of images reduces to two. However, as seen in the right panel, some additional *smooth bumps* appear in $\widetilde{\mathcal{F}}(t)$, which are purely wave-optics features.

3. *Frequency-domain magnification function*: Once $\widetilde{\mathcal{F}}(t)$ is computed, it is straightforward to determine $\mathcal{F}(w)$. We perform an inverse Fourier transform of $\widetilde{\mathcal{F}}(t)$ and multiply it by the prefactor $w/(2\pi i)$:

$$\mathcal{F}(w) = \frac{w}{2\pi i} \times \int_{-\infty}^{\infty} dt \exp(iwt)\, \widetilde{\mathcal{F}}(t) \,. \tag{3.7}$$

From Eqs. (2.19) and (2.37), the dimensionless frequency w can be related to the GW frequency f as

$$w = \frac{8\pi G M_{\rm Lz}}{c^3} f \,. \tag{3.8}$$

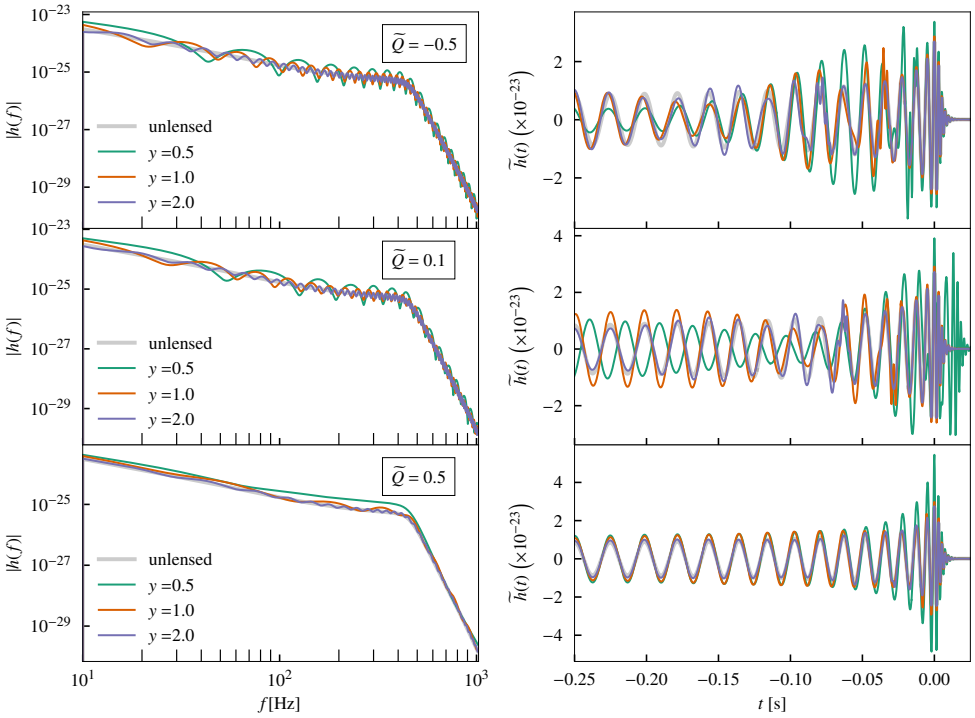

Figure 3.5: *Amplitude of microlensed GW signals for a $500M_\odot$ compact object at $z_L = 0.5$ with $\widetilde{Q} = -0.5, 0.1, 0.5$ (top to bottom) and various source positions (colors). Left: frequency domain; right: time domain. Gray lines show unlensed waveforms.*

While the time-domain magnification function $\widetilde{\mathcal{F}}(t)$ is purely real valued, its Fourier transform $\mathcal{F}(f)$ is generally complex. In Fig. 3.4 we show both the amplitude $|\mathcal{F}(f)|$ and the phase $\arg[\mathcal{F}(f)]$. As expected, the amplitude of $\mathcal{F}(f)$ is highest for negative $\widetilde{Q}$, and decreases as $\widetilde{Q}$ becomes more positive. Additionally, the magnification effect weakens as the source position y increases.

4. *Lensed waveform*: Finally, the lensed GW signal is obtained by applying the magnification function to the unlensed waveform. Specifically, we use Eq. (2.23) to obtain

$$\widetilde{h}^{\rm L}(f;\boldsymbol{\theta},\boldsymbol{\lambda}) = \mathcal{F}(f;\boldsymbol{\lambda})\,\widetilde{h}^{\rm U}(f;\boldsymbol{\theta})\,, \tag{3.9}$$

where $\boldsymbol{\theta}$ is the set of intrinsic and extrinsic source parameters, $\boldsymbol{\lambda} = \{M_{\rm Lz}, \widetilde{Q}, y\}$ is the set of lensing parameters, and

$$\widetilde{h}^{\rm U}(f) = F_+\widetilde{h}_+(f) + F_\times\widetilde{h}_\times(f) \tag{3.10}$$

is the unlensed waveform written in terms of the '+' and '×' polarizations, and the detector antenna pattern functions F_+ and $F_\times$ (discussed in Sec. 1.4.3).

Fig. 3.5 shows the microlensed GW signals in both the frequency (left panel) and time (right panel) domains, compared with the corresponding unlensed waveforms. The plots illustrate different values of the effective charge $\widetilde{Q}$ and source positions.

From the time-domain plots, we observe that the lensed waveform for $\widetilde{Q} < 0$ as well as for $\widetilde{Q} > 0$ with four images show the largest deviation from the unlensed waveform. In contrast, for positive $\widetilde{Q}$ with two image configuration, the lensed waveforms remain closer in morphology to the unlensed one. A similar trend for the phase relationship can also be seen.

These distinct features in both amplitude and phase, make it easier to detect and constrain negative and small positive values of $\widetilde{Q}$, compared to larger positive values, where the lensing effect is more subtle.

To validate our numerical method, we apply it to the case of a point mass lens (without charge), for which the magnification function is known analytically (see, Eq.(2.41)). We then compute the *mismatch* (see Sec. 3.4 for a definition) between the lensed waveforms obtained using the analytical magnification and those computed numerically with $\widetilde{Q} = 0$. The mismatch was found to be well within acceptable limits ($\lesssim 10^{-5}$), confirming the accuracy of our approach.

3.4 PROSPECTIVE CONSTRAINTS ON THE EFFECTIVE CHARGE

In this section, we estimate how well future microlensed GW observations could constrain the charge of a compact object. To do this, we use simulated microlensed GW signals and compute approximate Bayesian posteriors for the effective charge parameter $\widetilde{Q}$. Given some observed data d, the joint *posterior* probability for the source parameters ($\boldsymbol{\theta}$) and lensing parameters ($\boldsymbol{\lambda}$) under the microlensing hypothesis is given by Bayes' theorem:

$$p\left(\boldsymbol{\theta}, \boldsymbol{\lambda} | d\right) = \frac{p\left(d | \boldsymbol{\theta}, \boldsymbol{\lambda}, \mathcal{H}_{\rm ML}\right)\ p\left(\boldsymbol{\theta}, \boldsymbol{\lambda}\right)}{p\left(d | \mathcal{H}_{\rm ML}\right)}\ , \tag{3.11}$$

where $p(\boldsymbol{\theta}, \boldsymbol{\lambda})$ is the *prior* on the source and lens parameters, $p(d|\boldsymbol{\theta}, \boldsymbol{\lambda}, \mathcal{H}_{\rm ML})$ is the *likelihood* of observing the data d given the parameters and the microlensing hypothesis $\mathcal{H}_{\rm ML}$, and $p(d|\mathcal{H}_{\rm ML})$ is the *evidence*, i.e., the likelihood integrated over all possible parameter values.

The posterior distribution of the effective charge, $p(\widetilde{Q}|d)$, can be computed by marginalizing $p(\boldsymbol{\theta}, \boldsymbol{\lambda}|d)$ over all parameters except $\widetilde{Q}$. For simplicity, we assume that the lens parameters $\boldsymbol{\lambda}$ are largely uncorrelated with the source parameters $\boldsymbol{\theta}$. Hence we need to compute the likelihood only on $\boldsymbol{\lambda}$ for estimating prospective constraints on $\widetilde{Q}$. This is a reasonable assumption although recent work has identified possible correlations between microlensing modulations and modulations induced by spin-induced precession [224]. An uncharged point mass lens in the gravitational field of a macro lens (e.g., a galaxy) could also introduce more complex modulations in the GW signal [102, 121, 220, 225], potentially mimicking some of the effects of a charged lens. Also, note

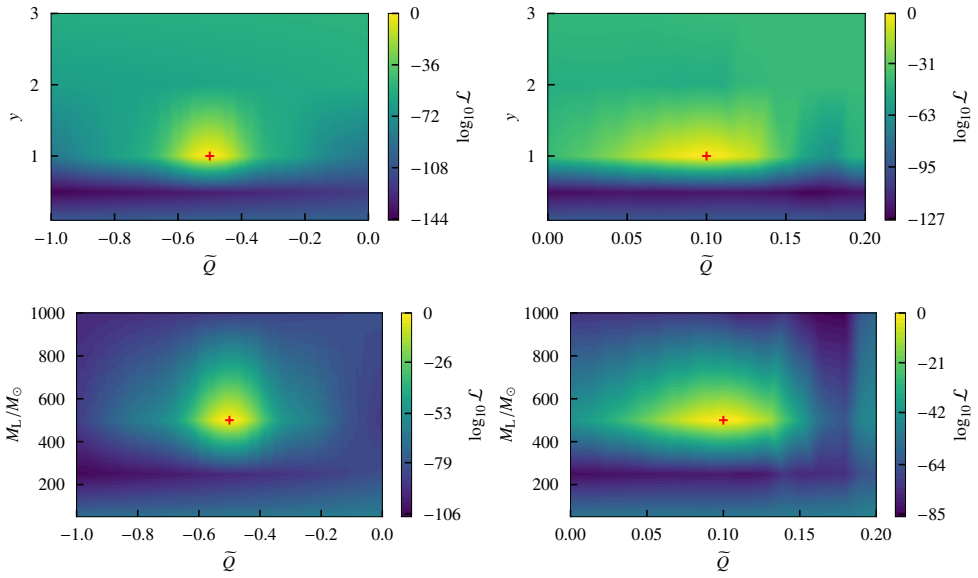

Figure 3.6: *Joint likelihood for* SNR $= 25$ *GW signals microlensed by a* $500M_\odot$ *charged compact object at* $z_L = 0.5$. *Top: likelihood in* y-$\widetilde{Q}$ *space. Bottom: likelihood in* M_L-$\widetilde{Q}$ *space. Red markers indicate true values.* $\widetilde{Q}$ *is largely uncorrelated with* M_L *and* y.

that currently, we assume nonspining compact object lenses. There could be some correlations between the charge and the spin of a compact object (see, e.g., [93]). For the time being, we ignore these additional complexities.

It turns out that the lens parameters M_L, y are also largely uncorrelated with the charge $\widetilde{Q}$ (see, Fig. 3.6 for an illustration). Thus, to compute the expected bounds on $\widetilde{Q}$, to a good approximation one needs to compute the likelihood in $\widetilde{Q}$ only. Assuming large SNR values for the future detectors[3] , we employ the following approximation of the expectation value of the likelihood (see Appendix A):

$$\mathcal{L}(\widetilde{Q}) \equiv \langle p(d|\widetilde{Q}, \mathcal{H}_{\rm ML})\rangle \simeq \exp\left[-\rho^2\left(1-\mathcal{M}(\widetilde{Q}_{\rm tr}, \widetilde{Q})\right)\right] , \tag{3.12}$$

which is valid upto a constant factor. Here ρ is the optimal SNR of the signal[4] and $\mathcal{M}$ is the *match* which measures the degree of similarity between the two waveforms with injected (true) charge $\widetilde{Q}_{\rm tr}$ and template waveform with charge $\widetilde{Q}$, defined in Eq. (A.8).

When we assume a flat prior in $\widetilde{Q}$, the expectation value of the posterior distribution $p(\widetilde{Q}|d)$ is the same as the likelihood $\mathcal{L}(\widetilde{Q})$. Hence we present $\mathcal{L}(\widetilde{Q})$ and its 90% credible upper limits in Fig. 3.7 and Fig. 3.8. In these figures, we have assumed the PSD of the advanced LIGO targeted for the O5 observing run (A+ configuration) [2]. Additionally, the unlensed signal is assumed to be due to a nonspinning equal mass black hole binary with component masses $20M_\odot$ each. We compute the likelihood assuming true values of $(\widetilde{Q}_{\rm tr}/M_L) = 0, -0.1$ and -0.5 in Fig. 3.7 and for the following true values of $(\widetilde{Q}_{\rm tr}/M_L) = 0, 0.1$ and 0.25 in Fig. 3.8.

Equation (3.12) shows that the likelihood decreases rapidly when the *mismatch* $(1-\mathcal{M})$ between the true charge $\widetilde{Q}_{\rm tr}$ and the trial value $\widetilde{Q}$ is large (i.e., when the two waveforms differ significantly), or when the SNR is high. This

[3] *SNR values can go up to several hundred for future detectors. Refer to [209, 250] for details.*

[4] *For the purpose of our study, SNR is a constant number.*

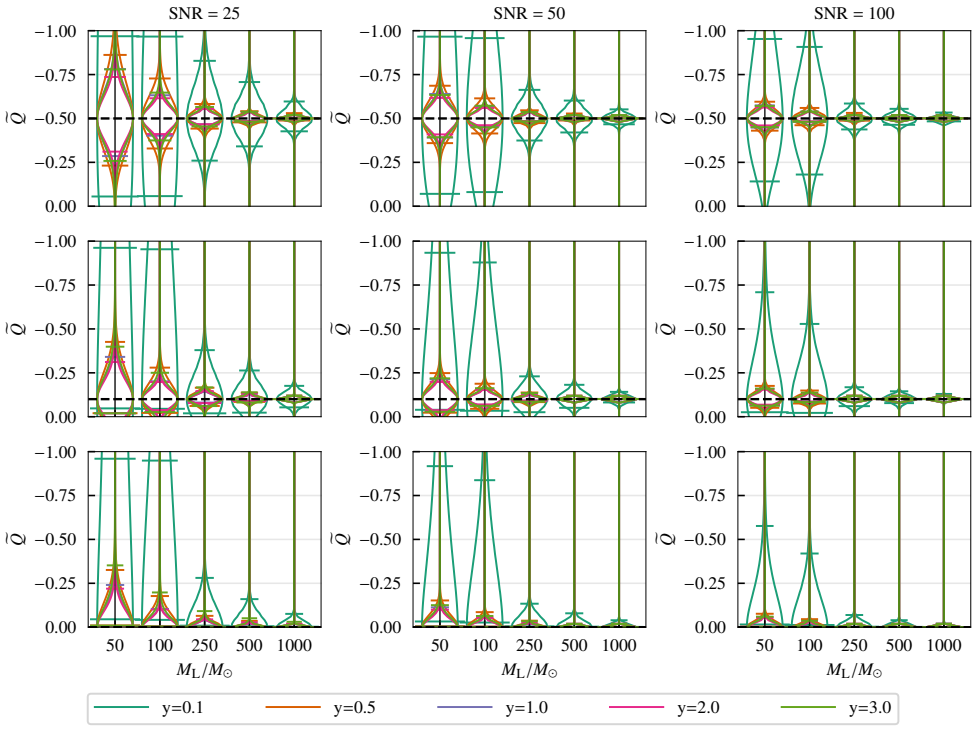

Figure 3.7: *Posteriors with 90% credible bounds on $\widetilde{Q}$ using aLIGO PSD, for various values the source position y (colors). Panels from left to right correspond to SNR values of 25, 50 and 100, respectively. In the top, middle and bottom panels, the GW signal is lensed by a BH of effective charge $\widetilde{Q}_{\rm tr} = -0.5, -0.1$ and 0, respectively (indicated by horizontal dashed black lines). Here, we use the prior $\widetilde{Q} \leq 0$.*

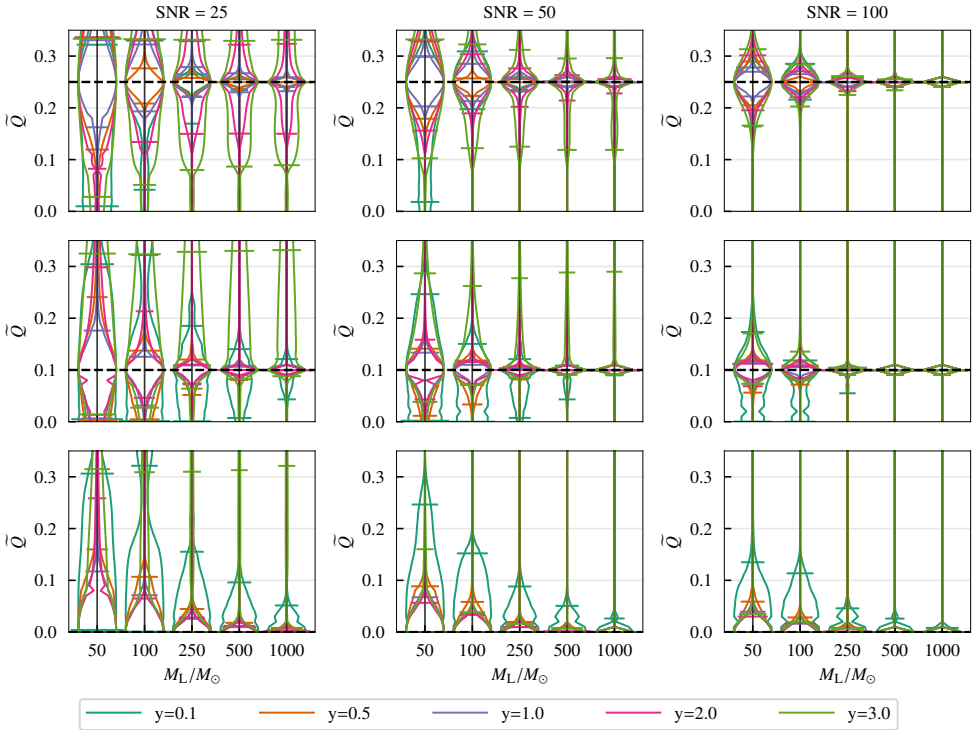

Figure 3.8: *Same as Fig. 3.7, except that the GWs are lensed by BHs of charge $\widetilde{Q}_{\rm tr} = 0.25, 0.1$ and 0, respectively (indicated by horizontal dashed black lines). Here, we use the prior $0 \leq \widetilde{Q} \leq 0.35$. Note that we have kept the prior such that the no-image parameter space is excluded. This is because there is no lensing of GWs in that parameter space.*

behavior is clearly visible in the figures. As expected, the precision with which $\widetilde{Q}$ can be measured improves at higher SNRs and for larger lens masses. Figure 3.9 summarizes the upper limits on $|\widetilde{Q}|$ for the case of an uncharged lens. Our ability to constrain various exotic scenarios will depend on these bounds. The improvement of the bounds with increasing SNR is straightforward. The tighter constraints at higher lens masses ($M_{\rm L} \sim 1000 M_\odot$) arise because such masses induce stronger wave optics effects in the GW signal. In general, the bounds are weaker for larger source positions y, since lensing effects diminish as the source moves farther from the lens axis. Interestingly, the bounds also become weaker for very small y, with the strongest constraints occurring near $y \simeq 1$.

As mentioned earlier, if astrophysical objects were found to have large negative effective charge, it would be a tell-tale signature of the existence of extra dimensions. In particular, such a feature arises naturally in braneworld scenarios, where our four-dimensional universe (brane) is embedded in a higher dimensional space (bulk). Even though an exact analytic description of how the brane is embedded in the bulk is not available, the size of the extra dimension, χ, can be estimated by numerically integrating Einstein's equations along the extra dimension, together with appropriate boundary (or junction) conditions [98].

For cases where $|\mathbb{Q}/M_{\rm L}^2| \sim \mathcal{O}(1)$, the influence of the higher-dimensional bulk on the brane is significant. In such scenarios, the size of the extra dimension χ cannot be arbitrarily small and is typically bounded by the ratio (G_5/G_4), where G_5 and G_4 are the Newton's constants in the five-dimensional bulk and four-dimensional brane, respectively. If G_5 is at the electroweak scale[5] , then the size of the extra dimension is constrained to be smaller than about $\mathcal{O}(10^{-18}\,\mathrm{m})$.

The induced tidal charge on the brane, $\mathbb{Q}$, is expected to depend exponentially on the geometry of the extra dimension. Specifically, numerical and perturbative studies suggest a relation of the form $(\mathbb{Q}/M_{\rm L}^2) \sim \exp(\ell/\chi)$, where ℓ is the AdS curvature radius of the extra dimension. So, for typical negative values of $\widetilde{Q}$ that we will be able to constrain, that is $|\widetilde{Q}| \lesssim 10^{-3}$, this would imply an upper bound $\mathbb{Q}/M_{\rm L}^2 \lesssim 10^8$. [6] . Using this exponential scaling, this translates to a lower bound on the size of the extra dimension: $(\chi/\ell) \gtrsim 0.1$, or equivalently, $\chi \gtrsim 0.1(G_5/G_4)$, assuming $\ell \sim G_5/G_4$. This estimate is motivated by studies of brane-localized black holes for which $\mathbb{Q}/M_{\rm L}^2 \sim \mathcal{O}(1)$ corresponds to $\chi/\ell \sim \mathcal{O}(1)$, and we assume a similar relationship holds for larger values of the charge. If G_5 corresponds to the electroweak scale, this lower bound becomes $\chi \gtrsim 10^{-19}\,\mathrm{m}$. Such a bound is complementary to small-scale tests of Newton's law [201, 216, 277, 310], which provide upper limits on the size of extra dimensions.

[5] *Large Hadron Collider (LHC) searches exclude extra spatial dimensions at energies below the electroweak scale (∼ few* TeV*). With optimal sensitivity, the constraint can improve by an order of magnitude.*

[6] *This estimate assumes typical lens and source parameters including mass and distance.*

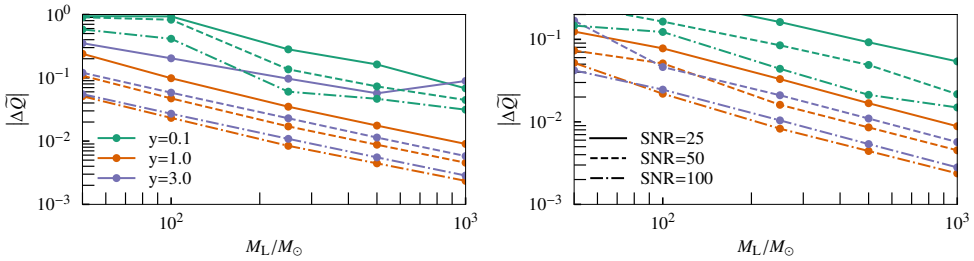

Figure 3.9: *Left: 90% upper bounds on negative $\widetilde{Q}$ as a function of lens mass M_L for various y (colors) and SNRs (line styles). Right: same for positive $\widetilde{Q}$, assuming an uncharged lens.*

3.5 SUMMARY AND OUTLOOK

Upcoming GW detectors are expected to detect gravitationally lensed GWs. Possible lenses include compact objects including BHs. When the gravitational radii of these lenses are comparable to the wavelength of GWs, lensing will produce wave optics effects, producing characteristic deformations in the observed signals. The exact nature of these deformations will depend on the precise spacetime geometry (lensing potential) of the lens. Thus, lensing observations can potentially probe the detailed nature of these lenses.

In this Chapter, we derived the lensing potential for a point mass lens carrying an effective charge. Although the charge $\mathbb{Q}$ can have an EM origin, in which case it is a positive definite quantity ($\mathbb{Q}$ is the square of the electric charge Q), it can also arise in (at least) four different situations, all of which are beyond GR. These include

- Braneworld gravity, where the presence of an extra spatial dimension modifies Einstein's equations, and introduces a charge term $\mathbb{Q}$ that is negative,
- Gauss–Bonnet theory in higher dimensions, which leads to an effective four-dimensional spacetime with a negative charge,
- $f(T)$ theories of gravity, and
- Certain class of Horndeski theories which brings in a positive charge term in the spacetime metric.

Thus, negative values of the charge definitely hint at the presence of extra dimensions, while positive values of the charge can have an EM origin, or can also arise from modified theories of gravity. If one can detect the charge hair of a compact object spacetime, it is possible to comment on the fundamental questions, e.g., the existence of extra dimension, as well as tell-tale signature of gravity theories beyond GR.

Using the lensing potential of charged point mass lens that we derived, we computed the deformation of the lensed GW signals considering wave optics effects. This was done using a numerical scheme that we developed. This

scheme is capable of computing the frequency-dependent lensing magnification for arbitrary lensing potentials. We noticed interesting new observables in the case of charged lenses. Owing to the axial symmetry of the lensing potential, the images and the source always lie on a line on the lens plane (same as the case of uncharged lens). For a negatively charged lens there are always two images (same as the uncharged lens), while for a positively charged lens, there can be two or four images, depending on the value of the charge and the source position. This new feature can be understood in terms of the (numerically computed) structure of the caustics of charged lenses. This introduces rich and complex effects in the lensed GW signals which are absent in those lensed by uncharged BHs. These additional features would help us to identify the presence of positively charged compact object lenses, if they exist. On the other hand, negatively charged lenses produce features very similar to those of uncharged BHs, making it difficult to distinguish them from uncharged BHs.

We then explored the ability of future lensing observations to constrain the charge of the lens. We consider lensing observations by a single LIGO detector with sensitivity anticipated in the O5 observing run. We showed that modest constraints on the charge can be obtained using observation of lensed GWs. Our ability to constrain the charge parameter is weakened by the fact that the charge-dependent term in the lensing potetial has a coefficient that is $\mathcal{O}(M_{\rm L}/D_{\rm L})^{1/2}$, which is very small ($\sim 10^{-10}$) in typical astrophysical lensing scenarios (here, $M_{\rm L}$ is the mass of the lens and $D_{\rm L}$ is the angular diameter distance between the lens and the observer). Even for a maximally charged BH, the effect of electric charge is too weak to be measurable in the foreseeable future. Thus, any measurable charge will be of modified gravity origin; not electric charge. If the GW lensing confirms a positive value of charge, it is very likely that the lens describes a naked singularity. On the other hand, if a negative charge is confirmed, the lens could be a BH in an alternative theory of gravity (e.g., braneworld scenario).

Note that the expected constraints presented here are based on an approximate likelihood. We neglect possible correlations between lensing-induced modulations in GW signals and those produced by other physical effects, such as orbital eccentricity of the binary source. We also ignored the possible degeneracy between a GW signal lensed by a charged BH and a GW signal lensed by an uncharged point mass lens in the presence of a macro lens (e.g., a galaxy; see Chapter 4), which can introduce more complex features. Additionally, we also neglected the effect of the spin of the BH lens. While we expect these broad conclusions to hold, the precise forecasts of the prospective constraints need to be revisited in the future considering these additional complexities.

The numerical scheme that we employ to compute lensing magnification for arbitrary lensing potentials is too expensive to employ in actual GW parameter estimation which will require a large number of likelihood evaluations. In order to employ in GW parameter estimation, we need to develop some surrogate (see Chapter 5) or semianalytical models that interpolate the numerically computed lensing magnifications over the parameter space of interest.

In this Chapter, we have worked with static and spherically symmetric spacetimes so far, and hence it would be interesting to generalize the same to rotating spacetimes, as all astrophysical objects are, in general, rotating. One could explore the possibility of measuring the spin of the compact object from lensing observations. One could also explore more general spacetimes: here we have considered the cases where $-g_{tt} = g^{rr}$; it will be useful to understand how to derive the lensing potential for spacetimes, with $-g_{tt} \neq g^{rr}$. Another possibility is probing the astrophysical environment of BHs using lensing observations.

Note that some of the modifications to GR that induce an effective charge on BHs could also cause other effects in the generation and propagation of GWs, which we neglect here. Our proposal should be seen as a way of effectively checking the consistency of the GW signal that is lensed by a BH in GR (in this case the Schwarzschild metric). Any observed inconsistency with the Schwarzschild lens will need to be investigated further in order to ascertain the nature of the charge. This is similar in spirit to various other tests of GR using GW observations. In any case, future observations of lensed GWs are very likely to offer new ways of probing the nature of compact objects.

4

INVESTIGATING THE EFFICACY OF MICROLENSING SEARCHES USING PML MODELS

Dark matter (DM) accounts for a significant fraction of the mass-energy in the Universe [43, 69, 282]. Presence of DM is required to explain a wealth of observations ranging from galaxy rotation curves [274] and cluster dynamics [48] to Cosmic Microwave Background (CMB) anisotropies [170]. Cosmoogical N-body simulations incorporating DM also successfully conform with the observed morphology of large-scale structures and non-linear clustering [275].

Despite its clear gravitational imprint, the nature of DM remains elusive.[1] Two of the prominent DM candidate classes include weakly interacting massive particles (WIMPs) and massive astrophysical compact object halos (MACHOs). WIMPs consist of a number of fundamental particles beyond the Standard Model of particle physics. Another related class of candidates include axions and axion-like particles, which emerge from solutions to the combination of charge conjugation and parity (CP) transformation symmetry problem in quantum chromodynamics and are also predicted in various extensions of the Standard Model. None of these particles have been detected so far [260, 267]. MACHOs consist of baryonic objects (e.g., planets, white dwarfs, neutron stars etc.) and black holes – with primordial black holes (PBHs)[2] being potentially promising candidates of DM.

The abundance of PBHs is tightly constrained across a broad mass range. These limits arise from the absence of expected signals in various astrophysical and cosmological observations. PBHs with masses below $\sim 10^{-16}\,M_\odot$ would have evaporated via Hawking radiation, and the resulting γ-ray and positron fluxes are strongly limited by measurements of the extragalactic background and the galactic 511 keV line. Gravitational microlensing surveys in EM regime rule out PBHs in the range $\sim 10^{-11} - 1\,M_\odot$ as the dominant DM component. More massive PBHs can accrete matter during the cosmic dark ages, injecting energy that alters the ionization history and leaves imprints on the CMB. These are constrained by Planck and Far Infrared Absolute Spectrophotometer (FIRAS) data. LVK observations limit PBH abundances in the $1 - 100\,M_\odot$ range based on observed event rates and the non-detection of sub-solar mass binaries

[1] *See Bertone and Hooper [72] for a comprehensive review on dark matter candidates and their observational status.*

[2] *Carr and Hawking [90] proposed in 1974, that black holes could have formed from dense regions in the early Universe.*

$(10^{-1} - 1\,M_\odot)$. Dynamical constraints from disruption of wide binaries in the Milky Way halo, the stability of ultra-faint dwarf galaxies, tidal heating of globular clusters, and survival of stars in dense environments all place upper bounds on PBH densities at higher masses ($M > 100 M_\odot$). Additional limits arise from large-scale structure formation, early-Universe nucleosynthesis (BBN), and the preservation of the Lyman-α forest.[3]

[3] *Refer to Carr et al. [91] and Carr and Kuhnel [92] for a detailed review on these constraints.*

GW microlensing in the ground-based detectors can arise from compact microlenses in the mass range $\sim 10^2 - 10^5 M_\odot$. There has not been any confirmed detection of wave-optics effects in the detected CBC events till date [36, 160]. These searches commonly employ a Bayesian model comparison framework, using the *Bayes factor* to distinguish between the lensed and unlensed hypotheses. Non-observation of microlensing signatures in the LVK data has been used to place upper bounds on the *fraction of dark matter as MACHOs* ($f_{\rm DM}$) within the aforementioned mass range [66]. This mass regime is particularly relevant for PBHs, which are typically modeled as isolated point mass lenses. However, in realistic astrophysical scenarios, compact lenses are not truly isolated; they often reside within larger structures such as galaxies. Consequently, the isolated PML may be an oversimplification, potentially introducing biases in the microlensing analyses.[4] In this Chapter, we investigate how the presence of an external galactic potential modifies the lensing signatures and impacts the efficiency of current microlensing searches. Specifically, we quantify the degradation in the Bayes factor due to the background galaxy in a statistical sense, which can weaken the constraints on $f_{\rm DM}$ from the non-observation of microlensing events.

[4] *Diego et al. [121] and Mishra et al. [225] study the effects of a population of microlenses embedded in an external potential on strongly lensed GWs.*

The remainder of this Chapter is organized as follows. In Sec. 4.1 we introduce the lens model which incorporates the external potential effects. In Sec. 4.2 we sample a realistic population of lensing configurations. Sec. 4.3 highlights the methods employed in computing the lensed waveforms. Sec. 4.4 discusses the primary results where we quantify the loss in Bayes factor due to non-consideration of host galaxy effects in microlensing. Finally, in Sec. 4.5 we summarize our findings and highlight possible future work.

4.1 MICROLENS IN A GALACTIC POTENTIAL

PBHs as microlenses (or atleast a fraction of them) are expected to reside within the DM halos of galaxies. In this work, we assume these host galaxies as having a spherically symmetric mass distribution modeled by a singular isothermal sphere (SIS) profile. This profile effectively captures the flat rotation curves observed in galaxies via a constant velocity dispersion, σ_v (see Sec. 2.4.3). The gravitational influence of the host galaxy on the microlens is incorporated as an external tidal field. This effect is quantified through the convergence field

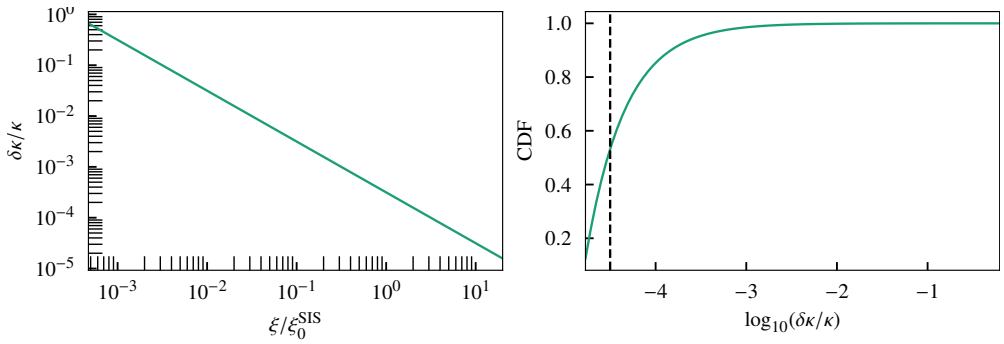

Figure 4.1: *Validity of constant κ approximation for SIS lens with $\sigma_v = 200\,\mathrm{km/s}$. (Left) Fractional variation of κ between adjacent grid spaced by the Fresnel radius. (Right) Cumulative distribution of this variation across the galaxy.*

κ and the shear field γ (see Sec. 2.4.5). For an SIS galaxy, κ and $\gamma \equiv \{\gamma_1, \gamma_2\}$ are related to each other as follows [193]

$$\gamma_1 = -\kappa \cos 2\varphi_\gamma \tag{4.1a}$$

$$\gamma_2 = -\kappa \sin 2\varphi_\gamma \tag{4.1b}$$

where φ_γ is the position angle defining the orientation of the external shear. For SIS, the convergence field is given by Eq. (2.67).

The characteristic distance scale over which wave effects are significant for microlensing is set by the Fresnel scale $r_{\rm F}$ of the microlens, given by [204]

$$r_{\rm F} \equiv \left(\frac{D_{\rm L} D_{\rm LS}}{D_{\rm S}} \frac{c}{2\pi f (1+z_{\rm L})} \right)^{1/2} = \frac{R_E}{\sqrt{w}}\,, \tag{4.2}$$

where R_E is the Einstein radius defined in Eq. (2.37) and w is the dimensionless frequency given in Eq. (3.8). To check for the variation of κ in the vicinity of the microlens, we partition the radial coordinate ξ (since SIS is axially symmetric) on the lens plane (centered on the galactic core) into segments of size $r_{\rm F}$. We fix $r_{\rm F}$ to the largest possible value considered in this study. We find that within each segment, κ can be treated as effectively constant. This is justified by the fact that the fractional variation $\delta\kappa/\kappa$ across a Fresnel-scale region is typically below 10^{-4} (based on the median). The left plot of Fig. 4.1 shows the fractional variation $\delta\kappa/\kappa$ as a function of the projected distance ξ from the galactic centre, expressed in units of the Einstein radius of the SIS lens $\xi_0^{\rm SIS}$ (see Eq. (2.64)), assuming $\sigma_v = 200\,\mathrm{km/s}$, $D_{\rm L} = 500\,\mathrm{Mpc}$ and $D_{\rm S} = 1000\,\mathrm{Mpc}$. The right plot of Fig. 4.1 shows the cumulative distribution of $\delta\kappa/\kappa$. Even though $\delta\kappa/\kappa$ can be as large as ~ 1 for very small values of ξ, the number of microlenses expected in this region is very small (see the left plot of Fig. 4.4), thus, validating that κ is effectively constant around the microlenses.

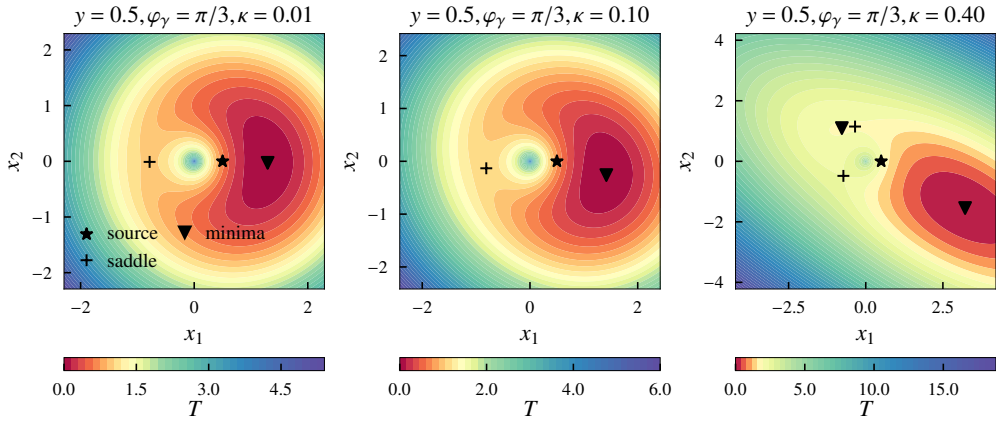

Figure 4.2: *Contours of the time delay T (in units of $4GM_{\mathrm{Lz}}/c^3$, with $T = 0$ at the global minimum) as a function of the lens plane coordinates (x_1, x_2) for the PMX lens.*

With this setup, the dimensionless time delay function for the *point lens embedded in an external potential* (PMX) can be obtained from Eqs. (2.83) and (2.20) as

$$T(\mathbf{x}, \mathbf{y}) = \frac{|\mathbf{x} - \mathbf{y}|^2}{2} - \ln(|\mathbf{x}|) - \frac{\kappa}{2}|\mathbf{x}|^2 + \frac{\kappa}{2}\cos 2\varphi_\gamma (x_1^2 - x_2^2) + \kappa \sin 2\varphi_\gamma \, x_1 x_2 \,, \tag{4.3}$$

where κ and φ_γ denote the local values, evaluated at the position of the microlens. Fig. 4.2 displays the time delay maps corresponding to several representative lens configurations. The source is fixed at $y = 0.5$,[5] while convergence takes values $\kappa = \{0.01, 0.1, 0.4\}$, with the shear orientation set to $\varphi_\gamma = \pi/3$. As evident from the figure, the first two configurations (left and center panels) give rise to two images (a minima and a saddle image), whereas the third (right panel) results in four distinct images (two minima and two saddle images) under the geometric-optics approximation.

[5] *We exploit the coordinate degree of freedom to fix the source position along the y_1-axis by setting $y_2 = 0$ henceforth.*

The shaded regions in Fig. 4.3 delineate the subset of the κ-y parameter space that yields four images in the geometric-optics limit. Outside of this region, only two images are produced. As the plot indicates, the number of images increases with both increasing convergence κ and source offset y. This behavior is consistent with the image configurations observed in the time delay maps of Fig. 4.2, thereby reinforcing the interpretation based on caustic structure in the PMX model.

4.2 GENERATING A POPULATION OF MICROLENSES

The spatial distribution of microlenses within the galaxy is modeled according to the Navarro-Frenk-White (NFW) profile [237, 238], which is a widely adopted model for the DM density profile of galactic halos in the cold dark matter (CDM) paradigm. This profile emerges naturally from cosmological N-body simulations [84] and captures the nearly universal density profile of virialized halos across a wide range of mass scales (see Sec. 2.4.4 for details).

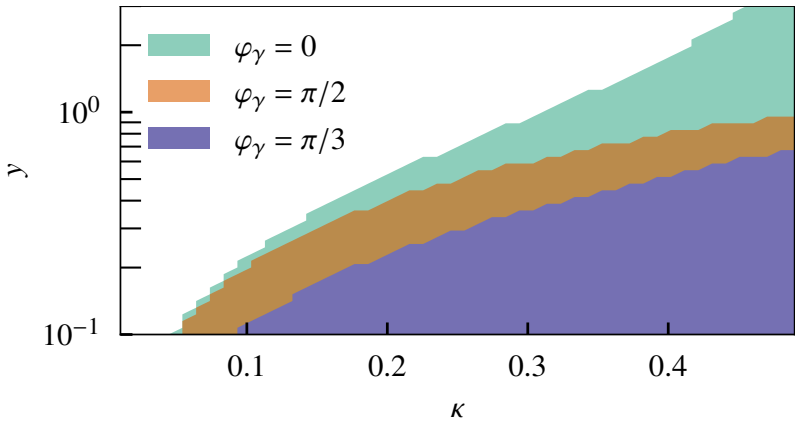

Figure 4.3: *Regions of κ-y parameter space that produce four images. Colors indicate different values of φ_γ. The unshaded area corresponds to configurations that produce only two images.*

While baryonic components (e.g., stars, gas) dominate the inner regions of galaxies, compact objects such as PBHs are expected to trace the underlying DM distribution. Consequently, if microlenses constitute a fraction of the DM, their spatial distribution should follow that of the host halo and be reasonably described by the NFW profile.

In our setup, we assume a Milky Way-like halo with virial mass $M_{\rm vir} = 10^{12} M_\odot$ and concentration parameter $c_{\rm vir} = 12$ [79, 219]. $M_{\rm vir}$ is defined as the mass within the virial radius $r_{\rm vir}$, which marks the extent within which the halo is in approximate dynamical equilibrium. The concentration parameter is defined as $c_{\rm vir} \equiv r_{\rm vir}/r_s$. Given these parameters, the scale radius r_s and the characteristic density ρ_s can be determined. We use the `Colossus` library [122] to compute these quantities, yielding $r_s \simeq 17\,\mathrm{kpc}$ and $\rho_s \simeq 10^7\, M_\odot/\mathrm{kpc}^3$.

Accordingly, we distribute the microlenses following the projected NFW surface density. The probability of finding a microlens between radial distances ξ and $\xi + d\xi$ on the lens plane is given by

$$dp = \Sigma_{\rm NFW}(\xi)\, 2\pi\xi\, d\xi \,, \tag{4.4}$$

where $\Sigma_{\rm NFW}$ is the surface density of the NFW profile (see Eq. (2.79)). Microlenses are sampled out to the virial radius of the halo ($\sim 200\,\mathrm{kpc}$). At each sampled position, κ is computed using the SIS form (Eq. (2.67)). The shear angle φ_γ is drawn from a uniform distribution $\mathcal{U}[0, \pi)$. The source positions are sampled from a radial distribution $p(y) \propto y$, with a cutoff $y \in [0.1, 3]$. We assume a monochromatic mass spectrum for the microlenses in the range of redshifted mass $M_{\rm Lz} \in [10^2, 10^5] M_\odot$.

Fig. 4.4 shows the resulting distribution of microlens locations measured from the galactic centre (left panel) and the corresponding distribution of κ values (right panel). As seen from the figure, the median value of $\kappa \approx 0.02$.

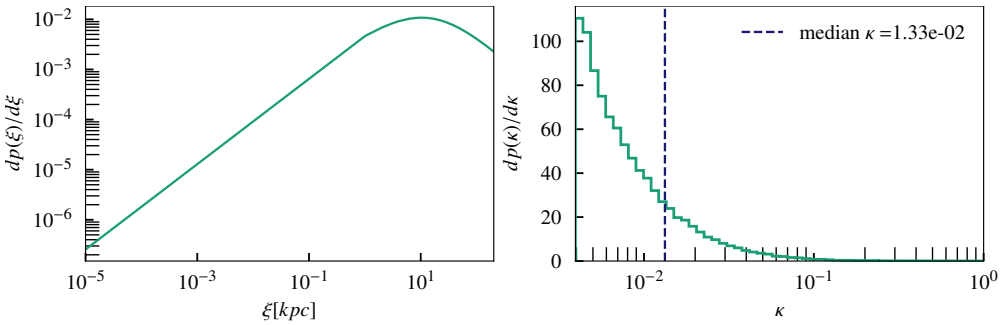

Figure 4.4: *(Left) Probability distribution of microlens location from the centre of the galaxy. (Right) Corresponding distribution of κ computed at those locations.*

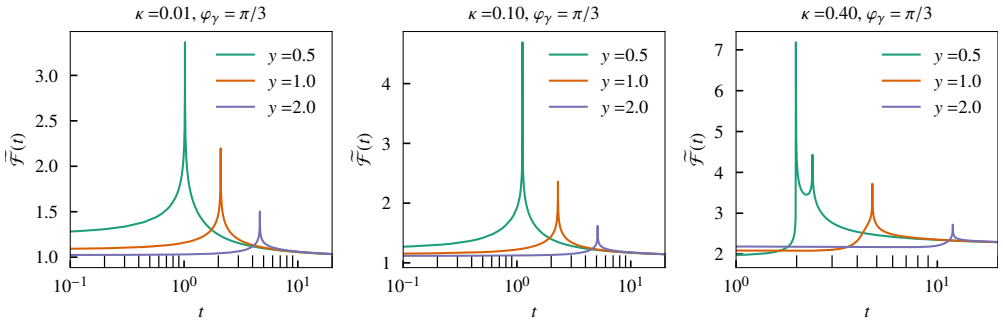

Figure 4.5: *Time-domain magnification function $\widetilde{\mathcal{F}}(t)$ for a PMX lens as a function of t (in units of $4GM_{\rm Lz}/c^3$), where the global minima lies at $t = 0$.*

4.3 COMPUTING MICROLENSED WAVEFORMS

The microlensed waveforms pertaining to the PMX model can be obtained by computing the magnification function (Eq. (2.22)), with the time delay function defined in Eq. (4.3). This integral, however, needs to be evaluated numerically and is computationally expensive owing to the oscillatory nature of the integrand. Therefore, we make use of the algorithm detailed in Sec. 3.3 to compute the time-domain magnification functions $\widetilde{\mathcal{F}}(t)$[6] , which are then used to compute the frequency-domain magnification functions $\mathcal{F}(f)$.

[6] *Throughout this chapter we restrict our analysis to $\kappa < 0.5$, since the PMX model does not produce closed time delay contours for $\kappa \geq 0.5$, making the computation strategy of $\widetilde{\mathcal{F}}(t)$ unreliable. In addition, Fig. 4.4 shows negligible support for such high values of κ.*

Fig. 4.5 shows the morphology of $\widetilde{\mathcal{F}}(t)$ for various values of convergence $\kappa = \{0.01, 0.1, 0.4\}$ and source positions $y = \{0.5, 1.0, 2.0\}$, for a fixed $\varphi_\gamma = \pi/3$. The contribution from the saddle images can be clearly identified from the logarithmic divergent peaks on the left and center panels. For the parameters in these two panels, there are always two images with the global minima image being at $t = 0$. The right panel also showcases two-image scenarios except for $y = 0.5$, which gives two minima and two saddle images. The saddle peaks can again be identified by their logarithmic signatures. The second minima appears as a jump discontinuity in $\widetilde{\mathcal{F}}(t)$ but has a time delay very similar to one of the saddle images, making it difficult to visually identify from the $\widetilde{\mathcal{F}}(t)$ plot. Interestingly, as $t \to \infty$, $\widetilde{\mathcal{F}}(t) \to 1/\sqrt{1-2\kappa}$. This implies that the asymptotic behavior of $\widetilde{\mathcal{F}}(t)$ in the case of PMX lens is different from that of the PML, where the $\widetilde{\mathcal{F}}(t)$ plots always asymptote to 1 at large t. This feature is attributed solely to the non-zero convergence of the external potential in PMX.

By Fourier transforming $\widetilde{\mathcal{F}}(t)$ and applying Eq. (3.7), we obtain $\mathcal{F}(w)$. The conversion from the dimensionless frequency w to the physical frequency f is

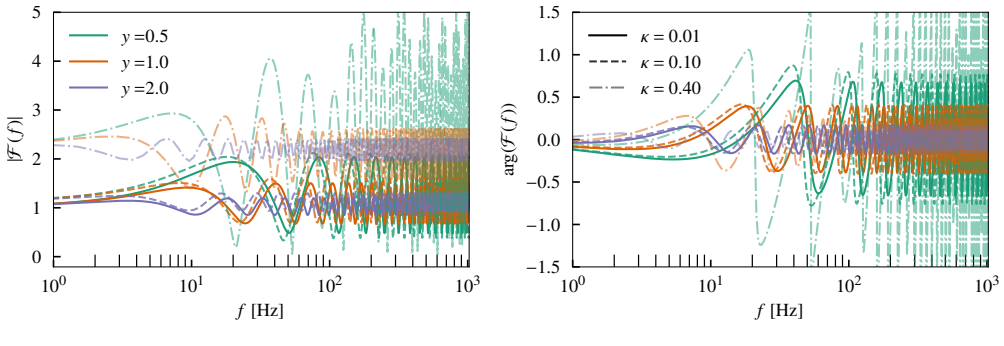

Figure 4.6: *Amplitude and phase of $\mathcal{F}(f)$ for a $500M_\odot$ lens at $z_L = 0.5$, with varying κ (lines) and y (colors), fixing $\varphi_\gamma = \pi/3$.*

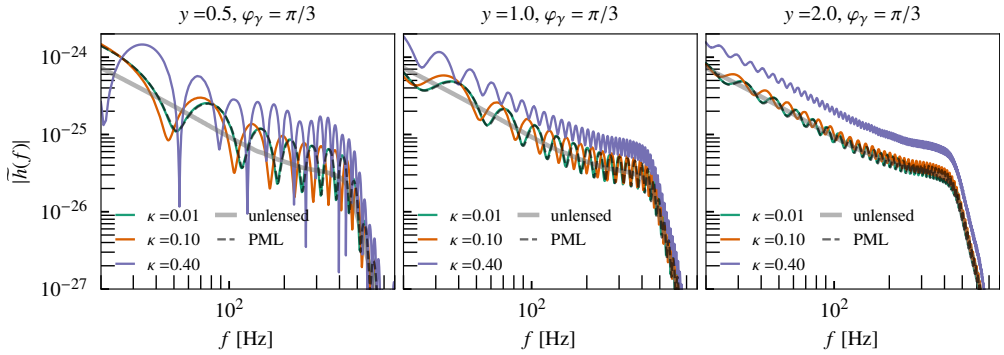

Figure 4.7: *Amplitudes of microlensed GWs for a $500M_\odot$ lens at $z_L = 0.5$, varying κ and y, with fixed $\varphi_\gamma = \pi/3$. The source is an equal-mass, non-spinning binary of total mass $40M_\odot$.*

performed using Eq. (3.8), given a redshifted lens mass M_{Lz} for the microlens. Fig. 4.6 displays the amplitude and phase of the magnification function for a PMX lens with $M_L = 500M_\odot$ at redshift $z_L = 0.5$. Different colors correspond to varying source positions while line styles distinguish between different convergence values. As evident from the figure, higher convergence leads to more pronounced modulations at lower frequencies. Moreover, a non-zero κ introduces an overall magnification offset, which increases with increasing κ.

Finally, we compute the lensed waveforms via Eq. (3.9), which requires an underlying unlensed GW signal specified by a set of source parameters $\boldsymbol{\theta}^b = \{\mathcal{M}_c, \eta, \chi_{\rm eff}, \chi_{\rm p}\}$. These parameters are defined as

$$\eta \equiv \frac{m_1 m_2}{(m_1+m_2)^2} \tag{4.5a}$$

$$\mathcal{M}_c \equiv (1+z_S)\eta^{3/5}(m_1+m_2) \tag{4.5b}$$

$$\chi_{\rm eff} \equiv \frac{\chi_{1z} m_1 + \chi_{2z} m_2}{m_1+m_2} \tag{4.5c}$$

$$\chi_p \equiv \max\left(\chi_1^\perp, \frac{4q+3}{4+3q} q\, \chi_2^\perp\right) , \tag{4.5d}$$

where m_1 and m_2 are the component masses of the binary, χ_{1z} and χ_{2z} their spin projections along the orbital angular momentum, $\chi_1^\perp$ and $\chi_2^\perp$ the corresponding spin projections perpendicular to the orbital angular momentum, η the symmetric mass ratio, $q \equiv m_2/m_1 \leq 1$ the mass ratio, $\mathcal{M}_c$ the redshifted chirp mass, $\chi_{\rm eff}$ the effective aligned spin, and $\chi_{\rm p}$ the effective precession spin. For generating the unlensed GW waveform, we employ the frequency-domain approximant `IMRPhenomXPHM` [253] which self-consistently includes both spin-induced orbital precession and higher order multipole corrections.

Fig. 4.7 illustrates the impact of microlensing by a PMX lens on the observed waveforms. For reference, the unlensed waveforms (in grey) and the PML-lensed waveforms (in dashed black) are also plotted. We consider a non-spinning, equal mass binary source with $m_1 + m_2 = 40M_\odot$. The lens parameters and configuration are the same as in Fig. 4.6. Across all panels, the microlensed waveforms deviate noticeably from the unlensed case. The deviation from PML is also prominent for large κ values. As the dimensionless source offset y increases, the strength of microlensing decreases as expected. At the same time, the introduction of an overall magnification offset due to a non-zero κ raises the baseline amplitude in each curve.

4.4 RESULTS

Given observational data d that contains a GW signal, the evidence for microlensing can be evaluated by computing the *Bayes factor* between the two competing hypotheses: the microlensed (PML-lensed) hypothesis $\mathcal{H}_{\rm PML}$, and the unlensed hypothesis $\mathcal{H}_{\rm U}$. The Bayes factor is defined as

$$\mathcal{B}_{\rm U}^{\rm PML} \equiv \frac{p(d|\mathcal{H}_{\rm PML})}{p(d|\mathcal{H}_{\rm U})} \,, \tag{4.6}$$

where $p(d|\mathcal{H}_{\rm PML})$ and $p(d|\mathcal{H}_{\rm U})$ are the Bayesian evidences (i.e., marginalized likelihoods) under the PML-lensed and unlensed hypotheses, respectively (see Eq. (B.3)). A Bayes factor $\mathcal{B}_{\rm U}^{\rm PML} > 1$ indicates that the data favor the microlensed scenario over the unlensed one, while values less than unity suggest greater support for the unlensed hypothesis. Current GW microlensing searches employ this Bayes factor as a statistical discriminator to infer the presence of microlensing signatures, and, in the absence of such signatures, to place upper bounds on $f_{\rm DM}$.

Similarly, we define the Bayes factor $\mathcal{B}_{\rm U}^{\rm PMX}$ to compare the PMX-lensed and unlensed hypotheses, thereby enabling the assessment of microlensing signatures when host galaxy effects on the microlens are included:

$$\mathcal{B}_{\rm U}^{\rm PMX} \equiv \frac{p(d|\mathcal{H}_{\rm PMX})}{p(d|\mathcal{H}_{\rm U})} \,. \tag{4.7}$$

Suppose the true signal is microlensed by a PMX lens with parameters $\boldsymbol{\theta}_{\rm tr}$,[7] but the inference is carried out using the simplified PML model and the corresponding Bayes factor $\mathcal{B}_{\rm U}^{\rm PML}$. We aim to investigate whether neglecting the influence of the host galaxy, that is, using an incorrect lensing model, significantly degrades the Bayes factor, hence reducing the sensitivity to microlensing.

[7] $\boldsymbol{\theta}_{\rm tr}$ *includes both source as well as lensing parameters* $M_{\rm Lz}, y, \kappa,$ *and* φ_γ.

To this end, we define the *loss factor* as the ratio of Bayes factors (see Eq.(B.7))

$$\text{L.F.} \equiv \frac{\mathcal{B}_{\text{U}}^{\text{PMX}}}{\mathcal{B}_{\text{U}}^{\text{PML}}} \simeq \exp\left[-\rho^2(1-\text{FF})\right] \ , \tag{4.8}$$

where the last equality holds only in the high SNR (ρ) limit (see Appendix B for a detailed derivation). The *fitting factor* FF is defined as

$$\text{FF} \equiv \max_{\boldsymbol{\theta}_{\text{PML}}} \mathcal{M}(\boldsymbol{\theta}_{\text{tr}}, \boldsymbol{\theta}_{\text{PML}}) \ , \tag{4.9}$$

where the match $\mathcal{M}$ is computed between the true PMX-lensed waveform and the best-fit waveform from the PML template family. The maximization of match is performed over the full parameter space $\boldsymbol{\theta}_{\text{PML}}$, encompassing both lens and intrinsic source parameters.

We compute the loss factor following the steps outlined below:

1. *Generate lensed injection signals*: We simulate a set of PMX-lensed injection (or true) signals in a grid spanning $\kappa \in [10^{-3}, 10^{-1}]$, $y \in [0.1, 3.0]$ and $M_{\text{Lz}} \in [10^2, 10^5] M_\odot$. The shear angle φ_γ is drawn uniformly from $\mathcal{U}[0, \pi)$. The source parameters include $\mathcal{M}_c = \{20, 30, 40\} M_\odot$ and $\eta = \{0.2, 0.25\}$, with all systems assumed to be non-spinning, that is, $\chi_{\text{eff}} = \chi_{\text{p}} = 0$. These define the true parameters $\boldsymbol{\theta}_{\text{tr}}$ for each simulated signal.

2. *Fitting factor computation*: For each of these true signals, we compute the fitting factor by maximizing the match over the PML parameter space, including $M_{\text{Lz}}, y, \mathcal{M}_c, \eta, \chi_{\text{eff}}$ and χ_{p}. We use the PSD pertaining to the advanced LIGO targeted for the O5 observing run (A+ configuration) [2].

3. *Re-weighting and marginalization*: The computed fitting factors are re-weighted and marginalized over the true lensing parameters $(\kappa_{\text{tr}}, y_{\text{tr}})$ using their probability distributions (see Sec. 4.2 for details on these distributions.) as

$$\langle \text{FF} \rangle = \int\int d\kappa_{\text{tr}}\, dy_{\text{tr}}\, p(\kappa_{\text{tr}})\, p(y_{\text{tr}})\, \text{FF}(\boldsymbol{\theta}_{\text{tr}}) \ . \tag{4.10}$$

   This gives the average FF over the microlens population.

4. *Loss factor estimation*: Inserting $\langle \text{FF} \rangle$ into Eq. (4.8), gives the corresponding average loss factor.

Fig. 4.8 presents the average loss factor pertaining to the microlens population as a function of the redshifted microlens mass for different chirp mass $\mathcal{M}_c$ and symmetric mass ratio η values. The SNR increases from left to right panels. The plots show that the degradation in Bayes factor becomes

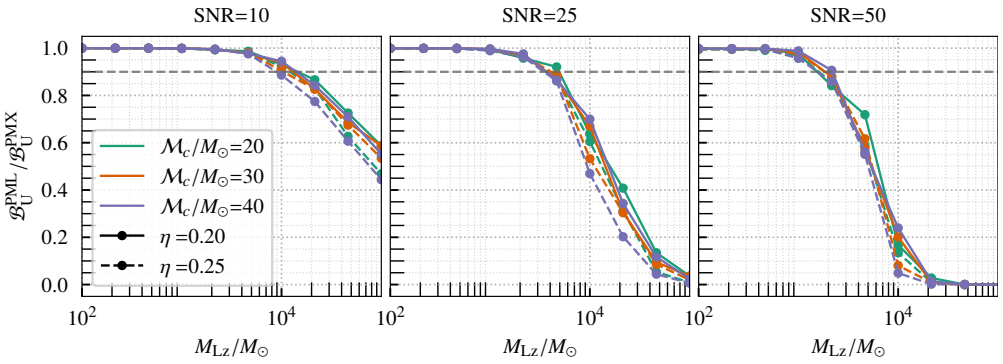

Figure 4.8: *Loss factor as a function of redshifted microlens mass. The panels show various SNR values, colors denote different $\mathcal{M}_c$ and η are denoted by different line styles.*

significant for higher microlens masses, whereas the simplified PML model remains an adequate approximation at lower lens masses.

4.5 SUMMARY AND OUTLOOK

In this work, we looked at the impact on microlensing due to the presence of an external potential – specifically, a galaxy parameterized by the convergence and shear modeled by the SIS lens – on the detectability of microlensing signatures in GW observations. To assess the effect of using an incorrect lens model, we defined the *loss factor* as the ratio of Bayes factors computed under the PMX and PML lensing models. In the high-SNR limit, this quantity depends on the mismatch between the true and best-fit waveforms.

Our analysis involved generating a set of PMX-lensed injection signals over a broad parameter space of lens and source properties. We computed the *fitting factor* between these signals and their best-fitting counterparts from the PML model. Lower values of the fitting factor reflects the inability of the PML model to capture waveform distortions introduced by the host galaxy's gravitational field.

By marginalizing the fitting factors over astrophysically motivated distributions of convergence and source position, we obtained the population-averaged loss factor, which quantifies the expected degradation in Bayes factor across realistic lens populations. The results, presented in Fig. 4.8, demonstrate that the use of an incomplete model leads to a systematic underestimation of the Bayes factor in the high lens-mass and high-SNR regime. This degradation becomes more pronounced for sources with higher symmetric mass ratios (comparable mass binaries).

These findings underscore the importance of including host galaxy effects in waveform models when searching for microlensed GW signals. Neglecting such effects may result in reduced sensitivity to microlensing events in current and future GW datasets. In addition, this can potentially affect the existing constraints on the compact dark matter fraction $f_{\rm DM}$.

Note that our current study suffers from some limitations. First, the macromodel of the host galaxy was assumed to be modeled by SIS, which, while an-

alytically convenient, does not fully capture the diversity of galactic potentials. In particular, elliptical galaxy profiles may introduce different distributions of shear and convergence, thereby altering the PMX parameter space. Second, our analysis assumes a high-SNR approximation to the Bayes factor, which may not hold for all observed events.

A more rigorous treatment would require assessing model evidences within a full Bayesian framework, rather than relying on the large-SNR approximation adopted here. It also involves using more realistic models for the background galaxy (e.g., singular isothermal ellipsoid - SIE). Since a full Bayesian analysis using more complex lens models is computationally prohibitive using current techniques, we defer such an analysis for future work. The surrogate modeling techniques introduced in Chapter 5 might provide a resolution to this issue. We will also re-derive the upper limits on $f_{\rm DM}$ in the future.

5

SURROGATE MODELING OF MICROLENSED GRAVITATIONAL WAVES

Gravitational microlensing of GWs offers a unique window into both fundamental physics and compact object populations. Examples of potential microlenses for LVK sources include (but are not limited to) isolated intermediate-mass black holes (IMBHs), whose masses lie in the range $M \in \sim [10^2, 10^4] M_\odot$. Currently, searches for microlensing/wave-optics patterns (see, e.g., [36]) in detected CBC events assume a point mass lens. This assumption is made for two reasons. The first is that an exact, analytical form of the frequency-domain microlensing magnification function, $\mathcal{F}(f)$, is known (see Eq. (2.41)[1]), which facilitates the creation of an interpolation table for $\mathcal{F}(f)$. The evaluation of this interpolant, for arbitrary GW frequencies and lens parameters (viz., lens mass and source position), is sufficiently rapid to attempt large-scale parameter estimation runs without prohibitively taxing computational resources [160]. The second is that IMBHs as microlenses have been argued to be well-modelled by the point mass lens [197].

[1] *The conversion between w and f is given in Eq. (3.8).*

However, other models of microlenses exist, many of which do not currently have any known analytical form for $\mathcal{F}(f)$. An example of particular astrophysical relevance is microlens(es) embedded in a macro potential (see, Chapter 4). It has been argued that a microlens, such as a massive compact object, lying in the halo of an intervening galaxy that provides the macro-potential, could result in the production of resolvable images with wave-optics effects imprinted on each of them [220]. Moreover, multiple microlenses in the macropotential would additionally produce interference patterns between the images [102, 121, 225, 245]. The resulting magnification function $\mathcal{F}(f)$, containing beating, diffraction and interference patterns, has no known analytical form to date.

Constructing such realistic $\mathcal{F}(f)$'s requires solving the diffraction integral, with the appropriate superposition of lensing potentials, numerically. This has been achieved (see, e.g., [225, 270]) using the method described in [289]. However, producing these $\mathcal{F}(f)$'s, for a single set of lens parameters, typically takes several seconds or longer per waveform, making large-scale GW parameter estimation (PE) of such lens configurations unfeasible.

In this Chapter, we adopt a widely used interpolation technique, called "surrogate modeling". This technique has found its application in modeling

waveforms in the context of CBCs [76, 77, 141, 149, 175–177, 259, 295, 296, 312, 313]; see Sec. 5 of Ref. [41] for a summary of recent CBC applications. In addition, a recent study has demonstrated the application of surrogate modeling to describe waveforms for hyperbolic encounters between black holes [145]. The main appeal of surrogate modeling lies in the fact that one can obtain a fast and accurate prediction of a high-dimensional, complicated function at arbitrary points in parameter space, interpolating from a finite (and usually small) set of points in that space where the function is known. To achieve this, surrogate models take advantage of the underlying similarity among the numerical solutions across the parameter space. Surrogate models thus provide a drastic increase in the evaluation speed of the function, compared to slow numerical solutions, while only negligibly deviating from them. We apply surrogate modeling, *for the first time*, to the rapid and accurate construction of time-domain lensing magnification functions $\widetilde{\mathcal{F}}(t)$. We benchmark the accuracy and production speeds of the surrogate microlensed GWs in the frequency-domain.

As a proof of principle, we consider the following lens models: point mass lens (PML) and singular isothermal sphere (SIS). We numerically evaluate the time-domain magnification function $\widetilde{\mathcal{F}}(t)$ at a few discrete points in the lensing parameter space. From these, we construct surrogate magnification functions $\widetilde{\mathcal{F}}^{\rm S}(t)$ for each of the lensing configurations. After Fourier transforming and producing microlensed GW waveforms in the frequency-domain, we evaluate the production-time and accuracy of the surrogate microlensed waveforms. We find that we are able to achieve mismatches of the order of $\mathcal{O}(10^{-7} - 10^{-3})$ with respect to the waveforms evaluated numerically, with evaluation times of $\mathcal{O}(10^{-1} - 10^{-2})$s. These benchmarking tests showcase the efficacy of surrogate modeling applied to microlensed GWs. They also suggest that surrogate modeling can be feasibly used for GW parameter estimation in the context of GW microlensing.

The rest of the Chapter is organized as follows. Sec. 5.1 introduces the basics of surrogate modeling and its application in the construction of time-domain lensing magnification functions. Sec. 5.2 presents the results which demonstrate the accuracy and evaluation speed of the surrogate microlensed waveforms. Finally, Sec. 5.3 summarizes the results and suggests future work.

5.1 METHOD

The integrand of the diffraction integral given in Eq. (2.22) can be highly oscillatory. As mentioned in Chapter 3, it is computationally expensive to evaluate the diffraction integral using conventional numerical schemes for astrophysically relevant lens models. Moreover, it is difficult to model oscillatory functions using surrogates. Therefore, we compute the magnification

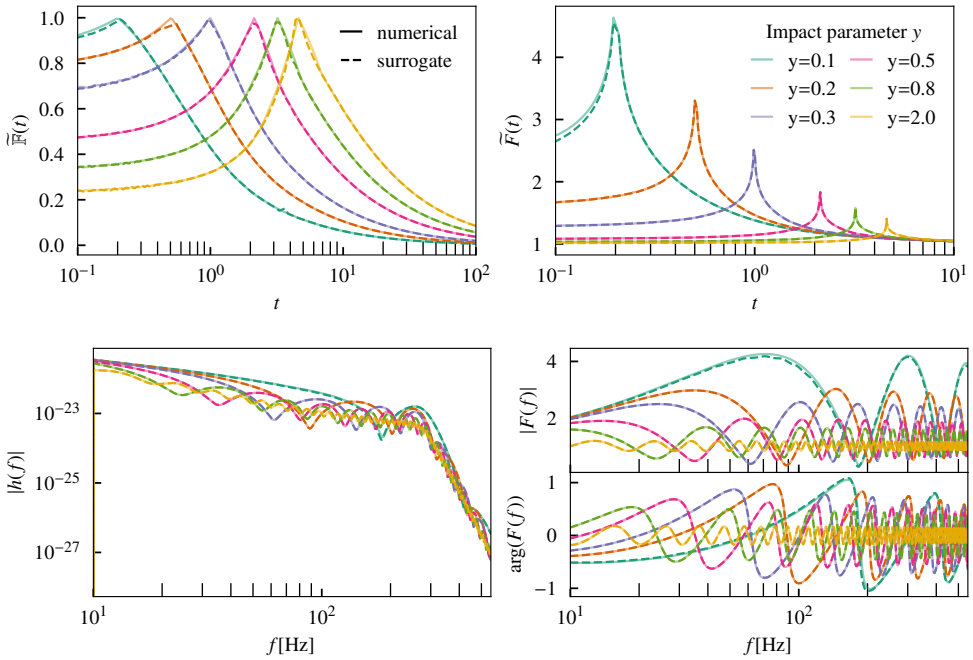

Figure 5.1: *Top row: The time-domain magnification function $\widetilde{\mathcal{F}}(t)$, and its regularized version (defined in Eq. (5.2)) $\widetilde{\mathbb{F}}(t)$, due to a PML for various source positions y as a function of time t (in units of $4GM_{\rm Lz}/c^3$, where the global minima lies at $t = 0$). Bottom left: Amplitude of the lensed waveforms considering a GW150914-like source. Bottom right: amplitude and phase of the frequency-domain magnification function $\mathcal{F}(f)$ for corresponding values of source locations computed numerically (solid lines) and with the surrogate models (dashed lines) for a lens of mass $M_{\rm L} = 10^3 M_\odot$ at redshift $z_{\rm L} = 0.05$.*

function in time-domain, following the idea described in Sec. 3.3. Surrogate models of $\widetilde{\mathcal{F}}(t)$ are then generated using numerically obtained $\widetilde{\mathcal{F}}(t)$ as the training data. The strategy is then to arrive at $\mathcal{F}(w)$ or $\mathcal{F}(f)$ using Eq. (3.7). This is also useful in generalizing the procedure to more complicated lenses. In this work, we construct surrogate lensing waveforms for the PML and SIS lens models, which are described in Sec. 2.4.

In this study, we focus on the lens parameter space that generates multiple images in the geometric-optics regime. The lens models considered here can produce at most two images. Cases with a single image are excluded as their corresponding $\widetilde{\mathcal{F}}(t)$ has a straightforward functional form, making them trivial to model. We emphasize that the geometric-optics quantities, such as, image time delays and image magnifications, are used in Sec. 5.1.1 and Sec. 5.1.2 solely to improve the modeling of $\widetilde{\mathcal{F}}(t)$. This is because the primary contribution to $\mathcal{F}(f)$ comes from the images, making it essential to capture them accurately. However, we do not apply the geometric-optics approximation to $\mathcal{F}(f)$ anywhere in this study.[2]

In this section, we outline the key steps in constructing the surrogate microlensed waveforms. We start by introducing the peak reconstruction procedure in Sec. 5.1.1, an essential step to accurately model the contribution of the region in the lens plane near the saddle point images to the time-domain mag-

[2] *Image parity produces a* Morse phase *in the geometric-optics magnification (see, Sec. 2.3). Without that approximation, the same phase is implicitly present in $\mathcal{F}(f)$.*

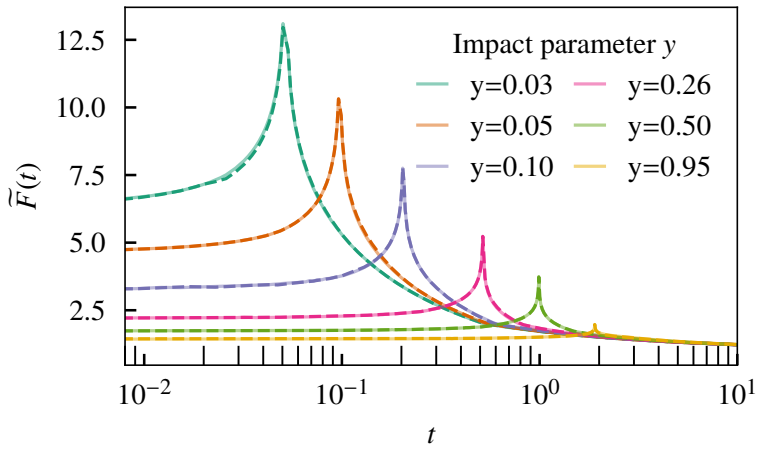

Figure 5.2: $\widetilde{\mathcal{F}}(t)$ *for an SIS lens at various* y*, comparing numerical (solid) and surrogate (dashed) results. Time is in units of* $4GM_{\mathrm{Lz}}/c^3$*, with* $t = 0$ *at the global minimum.*

nification function. We then describe the amplitude regularization technique in Sec. 5.1.2 to assist the surrogate to better interpolate between waveforms. Finally, in Sec. 5.1.3 we present the details of the surrogate modeling approach.

5.1.1 *Peak reconstruction*

Fig. 5.1 shows the magnification function in both the time-domain (top right panel) and frequency-domain (bottom right panel) for various source positions y, computed numerically (solid lines) and using the surrogate model (dashed lines) for PML (see Sec. 5.2 for details). The corresponding lensed GW waveforms are shown in the bottom left panel. The logarithmic peaks in $\widetilde{\mathcal{F}}(t)$ (top right panel) occur at $t = \Delta T$ (see Eq. (2.45) for PML and Eq. (2.74) for SIS), a feature characteristic of the saddle image. Similarly, Fig. 5.2 illustrates the time-domain magnification function, $\widetilde{\mathcal{F}}(t)$, computed for various source locations using both the numerical method (solid lines) and the surrogate model (dashed lines) for SIS.

Accurate computation of the time-domain magnification function via Eq. (3.4) demands sufficiently high resolution in the numerical integration. Nonetheless, even at high resolution, the numerical solution may struggle to capture the peak of $\widetilde{\mathcal{F}}(t)$ due to the logarithmic divergence at the peak. This limitation can impact the accuracy (especially at large w) of the frequency-domain magnification function $\mathcal{F}(w)$, as defined in Eq. (3.7) (see Fig. 5.3 for an illustration). Since w increases with M_{L} (refer to Eq. (3.8)), accurate modeling of the peak becomes even more important for large M_{L} values.

To overcome the limitation of numerical methods in resolving the peak feature, we utilize the analytical expressions for the peak location and the behavior of $\widetilde{\mathcal{F}}(t)$ in the vicinity of the peak is given by (see Eq. (3.6)),

$$\widetilde{\mathcal{F}}_{\mathrm{approx}}(t) = 2\pi\sqrt{\mu_+} - 2\sqrt{|\mu_-|}\,\ln\left(|t - \Delta T|\right)\,, \tag{5.1}$$

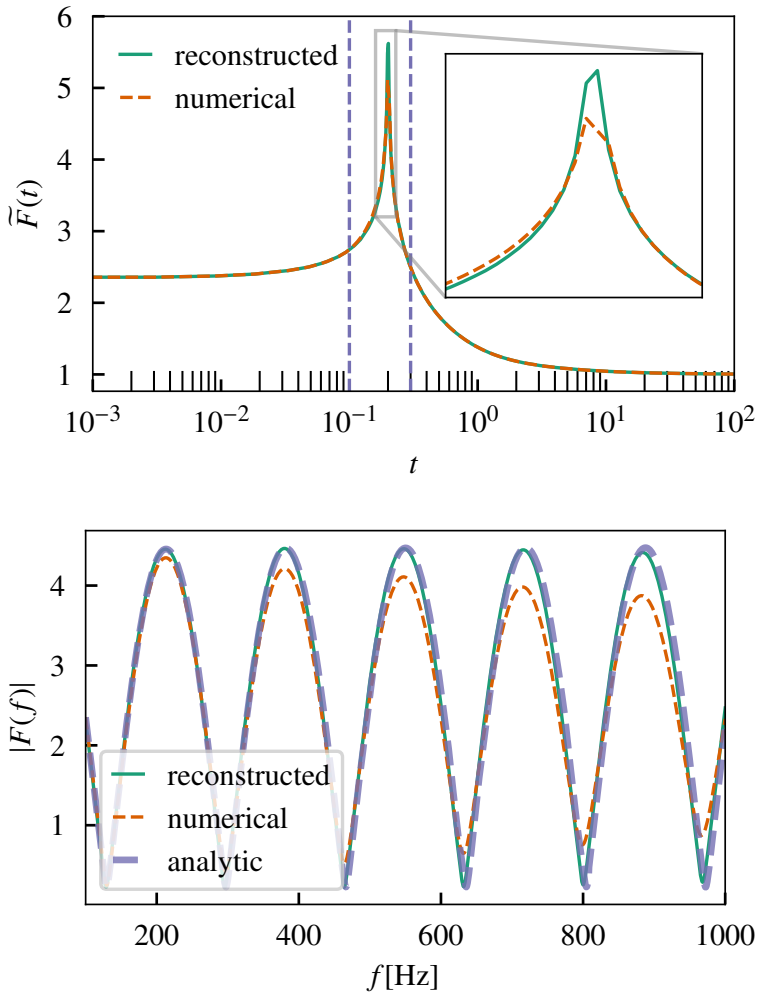

Figure 5.3: *Illustration of improvement in the accuracy of $\mathcal{F}(f)$ with peak reconstruction. Top: Time-domain magnification function with and without peak reconstruction for PML lens for $y = 0.1$ as a function of time t (in units of $4GM_{\mathrm{Lz}}/c^3$). The dashed vertical lines denote the window in which peak correction is applied. Bottom: Amplitude of the frequency-domain magnification function with and without peak reconstruction for the same lens with mass $M_{\mathrm{L}} = 1000M_{\odot}$ at $z_{\mathrm{L}} = 0.5$. Additionally, the analytically computed $|\mathcal{F}(f)|$ is shown for comparison.*

where the values of $\mu_\pm$ and ΔT are given by Eqs. (2.44), (2.45) for PML, and Eqs. (2.73), (2.74) for SIS lenses. We use the following steps to reconstruct the peak features by smoothly hybridizing the numerical and analytical approximation on either side of the peak:

(a) Identify the peak location, ΔT, using the analytic expression given in Eq. (2.45) for PML and Eq. (2.74) for SIS.

(b) Split the numerical $\widetilde{\mathcal{F}}(t)$ at ΔT into a left segment, $\widetilde{\mathcal{F}}^{\rm l}_{\rm num}(t)$, and a right segment, $\widetilde{\mathcal{F}}^{\rm r}_{\rm num}(t)$.

(c) Using the analytical approximation of $\widetilde{\mathcal{F}}(t)$ near the peak (Eq. (5.1)) evaluate the left and right approximations, $\widetilde{\mathcal{F}}^{\rm l}_{\rm approx}(t)$ for $t < \Delta T$ and $\widetilde{\mathcal{F}}^{\rm r}_{\rm approx}(t)$ for $t > \Delta T$.

(d) Define a reconstruction window, $[t^{\rm l}_{\rm match}, t^{\rm r}_{\rm match}]$, around ΔT to match and reconstruct the peak. The window span is empirically chosen: a larger span reduces accuracy of the approximation in Eq. (5.1) as it moves away from the peak, while a smaller window span depends on the accuracy of the numerical method near the saddle image. A window spanning a time interval equal to 5% on each side of ΔT is found to be effective.

(e) Rescale the approximated segments $\widetilde{\mathcal{F}}^{\rm l}_{\rm approx}(t)$ and $\widetilde{\mathcal{F}}^{\rm r}_{\rm approx}(t)$ to match the numerical $\widetilde{\mathcal{F}}(t)$ values at $t^{\rm l}_{\rm match}$ and $t^{\rm r}_{\rm match}$, respectively.

(f) Replace the portion of the numerical $\widetilde{\mathcal{F}}(t)$ within the reconstruction window with the rescaled approximated segments.

Following the above procedure results in a reconstructed time-domain magnification function,

$$\widetilde{\mathcal{F}}(t) = \begin{cases} \widetilde{\mathcal{F}}^{\rm l}_{\rm num}(t), & t \leq t^{\rm l}_{\rm match} \\ \widetilde{\mathcal{F}}^{\rm l}_{\rm approx}(t), & t^{\rm l}_{\rm match} < t < t_{\rm peak} \\ \widetilde{\mathcal{F}}^{\rm r}_{\rm approx}(t), & t_{\rm peak} < t < t^{\rm r}_{\rm match} \\ \widetilde{\mathcal{F}}^{\rm r}_{\rm num}(t), & t \geq t^{\rm r}_{\rm match} \end{cases},$$

which is a continuous, but non-smooth, function. Fig. 5.3 shows that reconstructing the peak in the $\widetilde{\mathcal{F}}(t)$ (top panel) consistently provides a better match (bottom panel) with the analytic expression (Eq. (2.41)) as compared to the vanilla numerical $\widetilde{\mathcal{F}}(t)$. As seen in the figure, the difference between the various methods becomes more pronounced at higher frequencies, primarily due to limited resolution near the peak. However, as discussed in Sec. 5.2, the peak-reconstruction method has been calibrated to ensure a maximum mismatch of 10^{-4} within the parameter space. Increasing the resolution can improve accuracy at high frequencies, though this comes at the cost of longer

generation times for the training data. Importantly, this does not impact the evaluation speed of the surrogate model.

5.1.2 *Amplitude regularization*

The logarithmic singularity at ΔT presents a challenge for accurately modeling the region near the peak of $\widetilde{\mathcal{F}}(t)$ using a surrogate. To address this, we apply a regularization procedure to the reconstructed $\widetilde{\mathcal{F}}(t)$ (see Sec. 5.1.1 for details on the reconstruction) and construct a surrogate model based on this peak-reconstructed, regularized time-domain magnification function, $\widetilde{\mathbb{F}}(t)$. The following transformation suppresses the peak contribution:

$$\widetilde{\mathbb{F}}(t) = 1 - \exp\left[-\pi \frac{\left(\widetilde{\mathcal{F}}(t) - 1\right)}{\sqrt{\mu_-}}\right] , \tag{5.2}$$

where μ_- is the magnification due to the saddle image, given by Eq. (2.44) for PML and (2.73) for SIS lens models. The regularization effectively eliminates the singularity and makes the derivative of the magnification function continuous. The top left panel in Fig. 5.1 compares the regularized $\widetilde{\mathbb{F}}(t)$ for PML computed for various source locations using the numerical method and the surrogate model for PML. After evaluating the surrogate, an inverse transformation is applied to obtain the time-domain magnification function $\widetilde{\mathcal{F}}(t)$ from $\widetilde{\mathbb{F}}(t)$.

5.1.3 *Surrogate modeling*

In this section, we introduce the basics of surrogate modeling, its application in computing the lensing magnification function for lensed GW waveforms and the setup used in this work. Surrogate modeling has been used extensively in building fast and accurate GW waveforms, especially in building surrogate models for Numerical Relativity (NR) waveforms [75, 141, 285]. Surrogate modeling is particularly advantageous in situations where the number of available waveforms is limited due to the prohibitively large computation time required to generate them, such as when solving partial differential equations, which results in a sparse training dataset. It is also highly beneficial when a data analysis study demands millions of waveform evaluations, requiring exceptionally rapid model evaluation times to meet the computational demands efficiently. For example, effective-one-body surrogates [111, 146, 189, 255, 256, 284] are extensively used as part of LVK parameter estimation efforts.

In the following, we will briefly discuss how surrogate modeling reduces the dimensionality of the problem by using reduced basis and empirical interpolation methods. These two methods ensure that with only a limited

number of waveforms (chosen appropriately), one can build an accurate model for predicting solutions outside the training set of parameters. Because these two steps can be precomputed, it also ensures that the model, evaluated at arbitrary points in parameter space, is orders of magnitude faster than numerical solutions.

5.1.3.1 *Surrogate modeling basics*

In the following, we briefly outline building a surrogate model.[3]

[3] *We follow the methods described in Sec. II and III of Field et al. [141] and refer the reader to it for a detailed overview of building a surrogate model.*

1. The first step is to find a minimal set of solutions called the *reduced basis* (RB) [140] in terms of which solutions at other parameters can be expressed. Given a known set of solutions (also called the training set), the RB is found using a greedy search algorithm. For example, with a RB with m basis elements, $\{e_i\}_{i=1}^{m}$, a solution $\widetilde{\mathbb{F}}(t;\boldsymbol{\lambda})$ in the training set at the lens parameter values $\boldsymbol{\lambda}$ can be well approximated as:

$$\widetilde{\mathbb{F}}(t;\boldsymbol{\lambda}) \approx \sum_{i=1}^{m} c_i(\boldsymbol{\lambda})\, e_i(t). \tag{5.3}$$

   This approximation is also good at other parameters outside the training set as long as the training set is dense enough. However, getting a dense training set can be very expensive and sometimes prohibitive. In such cases, one can build the training set using a greedy search method to provide an optimal training set for a given desired accuracy of the surrogate prediction. We come back to this in Sec. 5.1.3.3 where we discuss the surrogate modeling setup specific to our problem.

   Since the number of RB, m, is usually very small compared to the number of solutions in the training set, say M, the dimensionality of the problem reduces by a factor of m/M, which is usually $\ll 1$.

2. The next step is to find the most representative times, the empirical times or nodes $\{T_i\}_{i=1}^{m}$ to construct an interpolant in time using *empirical interpolant method* (EIM) [62, 100, 141, 166, 205] for a given parameter $\boldsymbol{\lambda}$:

$$\mathcal{I}_m[\widetilde{\mathbb{F}}](t;\boldsymbol{\lambda}) = \sum_{i=i}^{m} C_i(\boldsymbol{\lambda})\, e_i(t). \tag{5.4}$$

   The coefficients $C_i(\boldsymbol{\lambda})$ are defined by requiring that the interpolant becomes equal to the value of the solutions at the empirical nodes:

$$\sum_{i=i}^{m} C_i(\boldsymbol{\lambda})\, e_i(T_j) = \widetilde{\mathbb{F}}(T_j;\boldsymbol{\lambda}), \quad j = 1, ..., m \tag{5.5}$$

or equivalently,

$$\sum_{i=1}^{m} V_{ji}\, C_i(\boldsymbol{\lambda}) = \widetilde{\mathbb{F}}(T_j;\boldsymbol{\lambda}), \quad j = 1, ..., m \tag{5.6}$$

where the interpolation matrix is given by

$$V \equiv \begin{pmatrix} e_1(T_1) & e_2(T_1) & \dots & e_m(T_1) \\ e_1(T_2) & e_2(T_2) & \dots & e_m(T_2) \\ \vdots & \vdots & \ddots & \vdots \\ e_1(T_m) & e_2(T_m) & \dots & e_m(T_m) \end{pmatrix}. \tag{5.7}$$

The coefficients $C_i(\boldsymbol{\lambda})$ can be obtained by solving the above m-by-m system:

$$C_i = \sum_{j=1}^{m} (V^{-1})_{ij}\, \widetilde{\mathbb{F}}(T_j;\boldsymbol{\lambda}). \tag{5.8}$$

Substituting Eq. (5.8) in Eq. (5.4), the empirical interpolant can be rewritten as:

$$\mathcal{I}_m[\widetilde{\mathbb{F}}](t;\boldsymbol{\lambda}) = \sum_{j=i}^{m} B_j(t)\, \widetilde{\mathbb{F}}(T_j;\boldsymbol{\lambda}), \tag{5.9}$$

with:

$$B_j(t) \equiv \sum_{i=1}^{m} e_i(t)\, (V^{-1})_{ij}. \tag{5.10}$$

The function $B_j(t)$ is independent of $\boldsymbol{\lambda}$ and can be precomputed offline using only the information contained in the RB. Similar to the RB, the empirical nodes – also independent of $\boldsymbol{\lambda}$ and equal in number to the RB functions – are determined using a separate greedy search algorithm. Since the RB typically consists of only a few functions, the empirical interpolant's representation of the function, as expressed in Eq. (5.9), requires only a sparse set of time points. This eliminates the need for a dense, uniform temporal grid, which would otherwise significantly increase computational cost. As a result, the temporal dimensionality of the problem is reduced by a factor of m/L, where m is the number of RB functions (and empirical nodes), and L is the number of points required for interpolation on a uniform grid.

The use of RB and EIM reduces the dimensionality of the problem by a factor of $(m \times m)/(M \times L) \ll 1$.

3. With the interpolant $\mathcal{I}_m[\widetilde{\mathbb{F}}](t;\boldsymbol{\lambda})$ in Eq. (5.9) at hand, we need to know the values of the solutions at the empirical nodes $\{T_i\}_{i=1}^{m}$. Therefore, the

third step is to construct parametric fits at each empirical node across the parameter space.

4. Finally, the surrogate model prediction at a new parameter $\boldsymbol{\lambda}_*$ outside the training data set is computed by first using the parametric fits (constructed in the third step) to evaluate the values of $\widetilde{\mathbb{F}}(t;\boldsymbol{\lambda}_*)$ at the empirical nodes $\{T_i\}_{i=1}^m$ and then building the interpolant $\mathcal{I}_m[\widetilde{\mathbb{F}}](t;\boldsymbol{\lambda})$ using Eq. (5.9).

The first three steps are performed offline (i.e, precomputed), which drastically expedites the evaluation of the surrogate model at arbitrary points in parameter space.

5.1.3.2 *Surrogate for microlensed waveforms*

We apply the technique of surrogate modeling to obtain a model of the GW waveforms undergoing microlensing. However, since the effect of microlensing is a frequency-dependent modulation of the GW amplitude, one needs only to model this magnification function provided a fast, unlensed model exists already. Therefore, instead of modeling the microlensed waveform directly, we build a surrogate model $\widetilde{\mathbb{F}}^{\rm S}(t)$ for the regularized lens magnification function $\widetilde{\mathbb{F}}(t)$ in the time-domain. We then obtain the frequency-dependent magnification function $\mathcal{F}^{\rm S}(f)$ by taking a Fourier transform of the back-transformed $\widetilde{\mathcal{F}}^{\rm S}(t)$ (see Sec. 5.1.2). The surrogate microlensed waveform $\widetilde{h}^{\rm SL}(f)$ is then obtained from the unlensed waveform $\widetilde{h}^{\rm U}(f)$ using Eq. (2.23) as:

$$\widetilde{h}^{\rm SL}(f) = \mathcal{F}^{\rm S}(f) \times \widetilde{h}^{\rm U}(f). \tag{5.11}$$

5.1.3.3 *Surrogate modeling setup*

The RB is found by using a greedy algorithm that guarantees that the error

$$\sigma_m \equiv \max_{\lambda} \min_{c_i \in C} \left|\left| \widetilde{\mathbb{F}}(.;\boldsymbol{\lambda}) - \sum_{i=1}^{m} c_i(\boldsymbol{\lambda})\, e_i(.) \right|\right| , \tag{5.12}$$

associated with the approximation in Eq. (5.3) (minimized over the coefficients c_i and maximized over the parameter $\boldsymbol{\lambda}$) is less than a desired value, usually called the *basis tolerance*. Here, we have defined the standard L_2 norm as

$$\left|\left|\widetilde{\mathbb{F}}(.;\boldsymbol{\lambda})\right|\right| \equiv \sqrt{\int_{t_{\rm min}}^{t_{\rm max}} \left|\widetilde{\mathbb{F}}(t;\boldsymbol{\lambda})\right|^2 dt} \,. \tag{5.13}$$

Using an optimal basis tolerance when building the RB is crucial in making a surrogate model as fast as possible. Using a very small basis tolerance may result in a larger number of bases, which in turn results in a larger number of empirical time nodes. While evaluating the surrogate model, a significant

portion of the computation time involves evaluating the fits at the empirical nodes. Thus, a smaller basis tolerance is likely to make the surrogate model slower. Therefore, we use an optimal basis tolerance of $\sim 5 \times 10^{-4}$ for building the RB so that the surrogate models achieve the required accuracy compared to the microlensed waveform computed using the numerical solutions without causing any overfitting.

To obtain the training data set, we employ a greedy search algorithm as described in [76]. In the greedy search, we start with an initial training set consisting of only the corner points of the parameter range of interest. At each step, we build the surrogate model with a specific basis tolerance ($\sim 5 \times 10^{-4}$ in our case) and then validate it against a large number of numerical solutions generated randomly within the parameter range. This validation set excludes the parameters already in the training set. The validation involves measuring the normalized L_2 error between the surrogate prediction $\widetilde{\mathbb{F}}^{\mathrm{S}}(t)$ and the numerical solution $\widetilde{\mathbb{F}}(t)$,

$$L_2 = \frac{\sqrt{\int_{t_{\min}}^{t_{\max}} \left|\widetilde{\mathbb{F}}^{\mathrm{S}}(t) - \widetilde{\mathbb{F}}(t)\right|^2 dt}}{\sqrt{\int_{t_{\min}}^{t_{\max}} \left|\widetilde{\mathbb{F}}(t)\right|^2 dt}}, \tag{5.14}$$

where $t_{\min}$ and $t_{\max}$ denote the range of the time segment within which the error is computed.

We pick the parameter where the L_2 error is the maximum and add it to the training set to be used in the next step and repeat the procedure until we achieve the maximum L_2 error to be smaller than a desired value, which in our case is 10^{-2}. With such a greedy search, we find our training data sets that consist of $\sim 35 - 100$ data points depending on the particular microlens model.

For constructing the fits at the empirical nodes, we use the *Gaussian Process Regression* (GPR) method as described in the supplemental material of [296].

In a nutshell, the training data $\widetilde{\mathbb{F}}(t)$ is obtained by applying a peak reconstruction followed by a regularization operation on $\widetilde{\mathcal{F}}(t)$. This training data is used to build the surrogate $\widetilde{\mathbb{F}}^{\mathrm{S}}(t)$. Then an inverse transformation is applied followed by a peak reconstruction to obtain $\widetilde{\mathcal{F}}^{\mathrm{S}}(t)$.

5.2 RESULTS

In order to validate our model, we compute the match $\mathcal{M}$, defined in Eq. (A.8) between the surrogate microlensed waveform model and the corresponding numerical model used for training. We use `pycbc.filter.matchedfilter` module from the `PyCBC` package [240] to compute the match. We make use of the next-generation ground-based detector Einstein Telescope (ET) PSD,

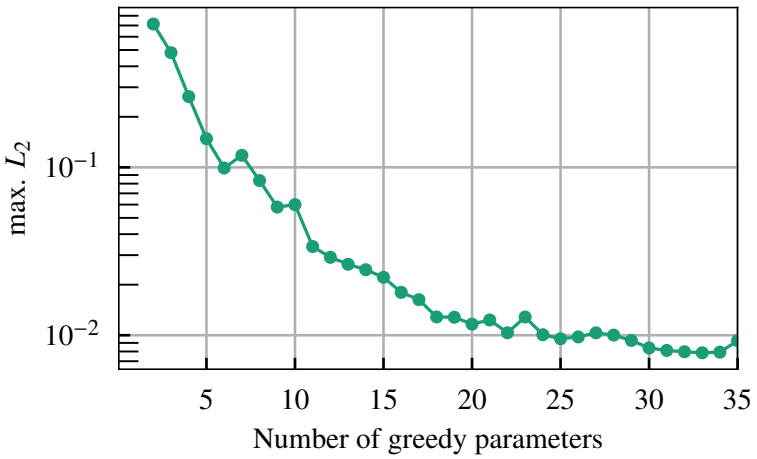

Figure 5.4: *Largest relative L_2 error of the surrogate for the PML model as a function of number of greedy parameters. The error is computed as the maximum error between the entire validation set and the surrogate model. The model is seen to converge as the training data set increases.*

pertaining to the ET design sensitivity [167]. The reason for choosing this particular PSD is two-fold: the frequency bin is larger than the current ground-based detectors, giving rise to conservative mismatches, and statistically, we expect to see a significant number of lensed GW events during the observing runs of next-generation detectors such as ET.

Note that, the numerical magnification functions used to train the model for PML and SIS are calibrated to the analytic form given in Eq. (2.41) for PML and the summation form given in Eq. (2.77) for SIS, such that the maximum mismatch $(1 - \mathcal{M})$ between the numerically computed lensed waveform and the analytically obtained lensed waveform is $< 10^{-4}$ for all possible points in the parameter space.

We present mismatches between the surrogate microlensed GWs and the numerically evaluated microlensed GWs used to construct the surrogate model. We ensure that the lensing parameters used for training the model, and those used for testing (i.e, evaluating the mismatches), are different. The lensing parameters are chosen over a grid, and the mismatches are evaluated for each point on that grid, as well as different unlensed CBC waveforms. Evaluation times per microlensed frequency-domain waveform are also measured. These are then compared with corresponding times pertaining to other methods, viz., a frequency-domain interpolation method employed by the LVK collaboration to search for GWs microlensed by PMLs, as well as numerical methods to acquire magnification function for the SIS lens. The waveforms are sampled at frequencies with bin width, $\delta f = 1/32$, resulting in the total number of waveform evaluation points in the frequency-domain to range from $\sim 1.3 \times 10^4$ (for total binary mass $M_{\rm tot} = 100 M_\odot$) to $\sim 6.5 \times 10^4$ (for total binary mass $M_{\rm tot} = 20 M_\odot$).

The surrogate model for PML is created using 27 basis vectors with a basis tolerance of 5×10^{-4}, while for SIS, it is created using 15 basis vectors with the same basis tolerance. We use the `numpy.fft` module from `NumPy` [164] package to compute FFT. All computations related to creating and evaluating

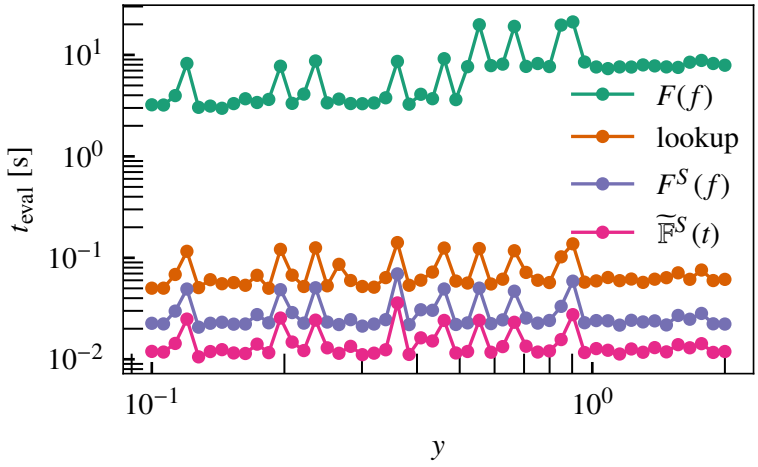

Figure 5.5: *Evaluation time for magnification functions for a PML with $M_L = 100M_\odot$ at $z_L = 0.5$, lensing an equal mass CBC source with $M_{tot} = 20M_\odot$. We compare evaluation times across source positions y for the numerical magnification function ($\mathcal{F}(f)$), the time-domain surrogate $\left(\widetilde{\mathbb{F}}^S(t)\right)$, its FFT $\left(\mathcal{F}^S(f)\right)$ and the lookup table.*

the surrogate model were performed on a 32-core workstation with Intel Xeon E5-2650 v2 chip, OS: Linux. Note that no parallelization was used during the evaluation; thus, the computations effectively used a single core.

POINT MASS LENS (PML): We create a surrogate model for the regularized time-domain magnification function $\widetilde{\mathbb{F}}(t)$. It is a single-parameter model parameterized by the source location y. Note that the lens mass M_L sets the time scale while converting the dimensionless angular frequency w to the dimension-full frequency f (see Eq. (3.8)). Therefore, it can be factored out while creating the model. We use the numerically computed $\widetilde{\mathbb{F}}(t)$ (as shown in Fig. 5.1) to train our model. Fig. 5.4 shows the improvement in the maximum L_2 between the numerically obtained $\widetilde{\mathbb{F}}(t)$ and the surrogate $\widetilde{\mathbb{F}}^S(t)$ with an increase in the number of greedy parameters. The error versus greedy parameters curve plateaus for greedy parameter counts greater than approximately 30 for PML. Therefore, we use the first 35 greedy parameters to construct the surrogate model. The greedy parameter space of y spans from $y = 0.1$ to $y = 2$.

The current LVK microlensing analysis makes use of an interpolation table ("lookup table") in $w - y$ plane to compute $\mathcal{F}(w)$ given in Eq. (2.41) for PML and Eq. (2.77) for SIS (see, e.g., [308]). We compare the evaluation time of the PML surrogate model with the lookup table to verify that it performs at least as well as the lookup table for simple lensing cases. For the SIS surrogate model, we compare with the numerical method, as our goal is to extend this study to more complex lens models where interpolation tables may not be feasible, and only direct numerical computations are possible.

Fig. 5.5 shows the evaluation time for the surrogate model compared to the lookup table for the same number of evaluation points. We also indicate the time taken to generate the numerically obtained $\mathcal{F}(f)$. As seen from

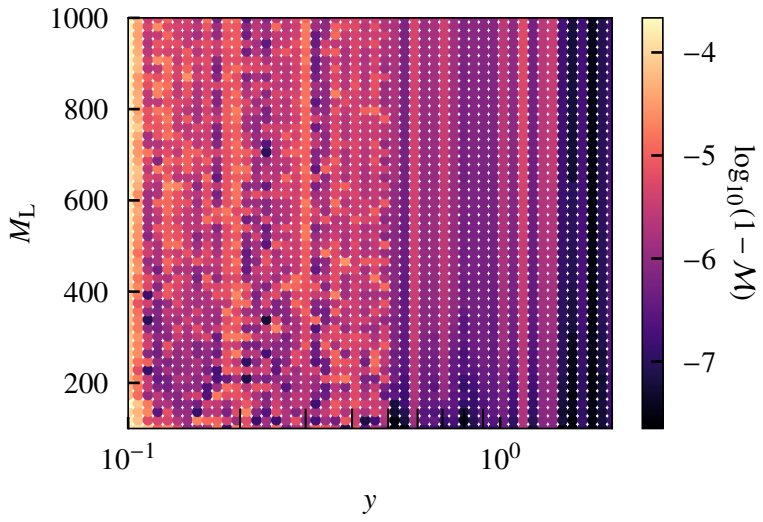

Figure 5.6: *Mismatch in the $M_L - y$ plane between the numerical method and the surrogate model for a lensed GW150914-like signal. We assume the lens to be a PML at $z_L = 0.05$*

the figure, the surrogate performs faster than the lookup table throughout the parameter space. Note that a part of the lookup table evaluation uses information from the geometric-optics approximation, whereas the numerical method and therefore, the surrogate model is based completely on the wave-optics computation.

Fig. 5.6 shows the mismatch between the surrogate microlensed waveform and the microlensed waveform obtained using the numerical method for a GW150914-like signal for various values of M_L and y. The unlensed waveform is generated using the `IMRPhenomXP` approximant [253]. As evident from the figure, the mismatches are better than 0.03%.

Further, we show the dependence of the accuracy of our model on the source mass of the binary by simulating equal component mass, non-spinning, binary black hole (BBH) unlensed waveforms for different total binary masses ($M_{tot} = \{20, 40, 60, 80, 100\} M_\odot$) by computing mismatch in the $M_L - y$ grid spanning $100 \leq M_L/M_\odot \leq 1000$ and $0.1 \leq y \leq 2$. We consider equal mass binaries. The top left panel in Fig. 5.8 shows the histogram of mismatch values for the different source masses between the lensed waveforms generated using the numerical method and the surrogate model. As can be seen, the mismatches are lower than 0.05%. Moreover, the top right panel compares the evaluation times for the surrogate with the lookup table for the same grid and source masses.

SINGULAR ISOTHERMAL SPHERE (SIS): Similar to the PML model, this model is also a single-parameter model parameterized by y. As shown in Fig. 5.7, the error versus greedy parameters curve plateaus for greedy parameter counts greater than approximately 85 for SIS. Therefore, to construct the surrogate model for SIS, we use the first 100 greedy parameters. The greedy parameter space of y spans from $y = 0.01$ to $y = 0.95$. We compute mismatch and compare evaluation times between the numerically obtained

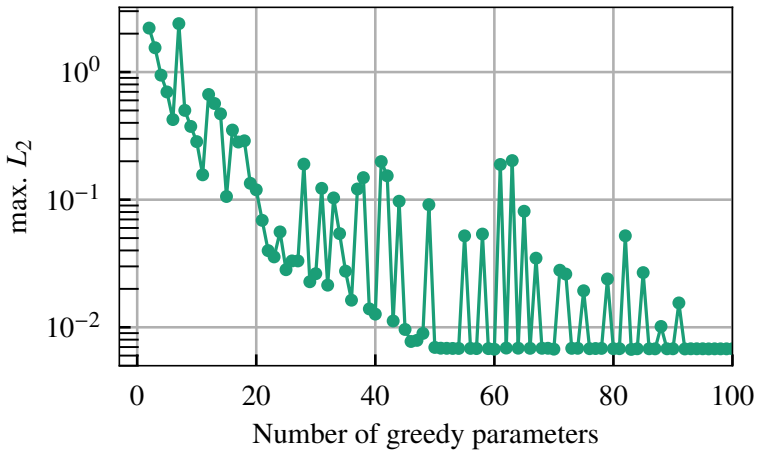

Figure 5.7: *Similar to Fig. 5.4, this shows the convergenge of the largest relative L_2 error of the surrogate for the SIS model as the training data set increases.*

microlensed waveforms and the surrogate microlensed waveforms. The bottom left panel in Fig. 5.8 shows the histogram of mismatch values for various source masses, similar to the case for PML. Here, we restrict the y values between $0.01 \leq y \leq 0.95$ because for $y > 1$ we are no longer in the two-image regime. Similar to PML, the mismatch values are within 0.05%, showing very promising results. The bottom right panel compares the evaluation times for the surrogate with the numerically obtained microlensed waveform. The surrogate model is evidently faster than the numerically obtained microlensed waveforms by orders of magnitude.

5.3 SUMMARY AND OUTLOOK

Probing for signatures of wave-optics-induced microlensing effects in detected GW events requires large scale Bayesian PE runs, whose feasibility crucially relies on accurate and rapidly producible microlensed waveforms. Apart from GWs microlensed by a PML and a few other simplistic lensing models, no closed form analytical solutions to the lensing equation exist. Numerical methods are, therefore, the only recourse to generate microlensed waveforms for most realistic lensing configurations.

Evaluating microlensed GWs numerically is time consuming, with waveform generation taking up to several seconds (per waveform). Indeed, even efficient numerical methods (see, e.g. [280]) are likely to be too slow to enable large-scale PE campaigns in a cost-effective manner. One way to mitigate this issue is to use interpolation, where the microlensing magnification function is evaluated at a few discrete points in the parameter space of the lens, and then interpolated to any arbitrary point. This has been attempted for the PML in the frequency domain, and found to be faster than directly evaluating the complicated magnification function analytically [36]. It has also been attempted for other spherically symmetric lensing configurations in the time domain, where the magnification function is then Fourier transformed to the

frequency domain [103]. Both these methods require reading-off precomputed interpolation data from a table, and are referred to in this work as the "lookup table" methods. For other efficient methods for rapid evaluation of lensing magnification functions, we refer the reader to [298].

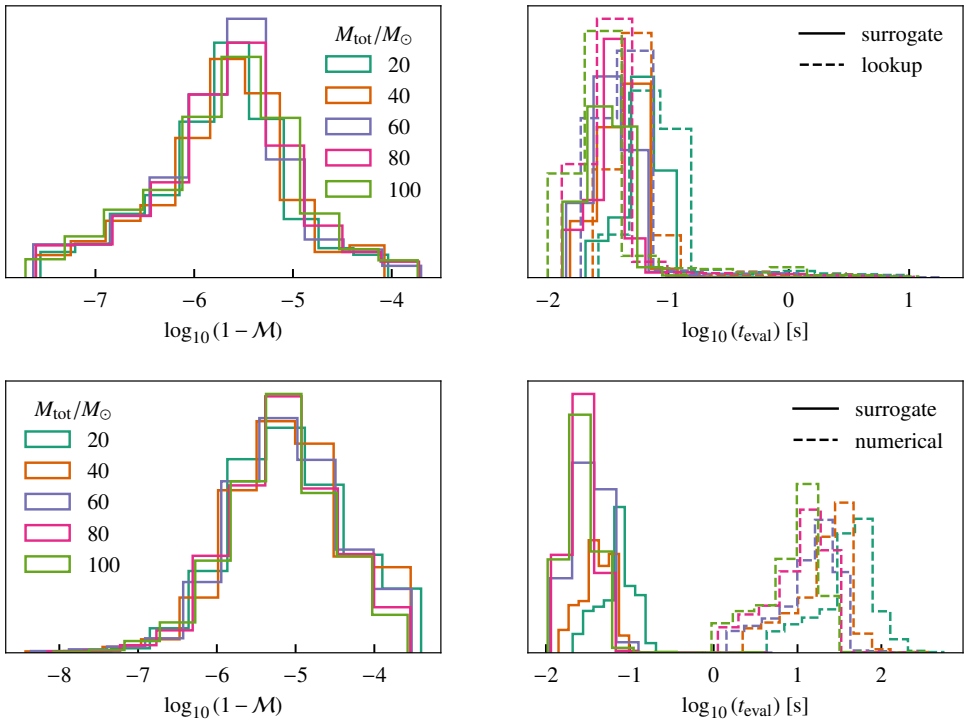

Figure 5.8: *Mismatch and evaluation time comparisons.* Top panel*: (Left) Histograms of mismatches between surrogate and numerical microlensed waveforms for a PML lens, across sources with* $M_{\rm tot} = \{20, 40, 60, 80, 100\} M_\odot$ *evaluated over a grid* $100 \leq M_{\rm L}/M_\odot \leq 1000$ *and* $0.1 \leq y \leq 2$*. (Right) Evaluation time histograms for the surrogate (solid) and lookup table (dashed) over the same* $M_{\rm L} - y$ *grid for PML.* Bottom panel*: (Left) Same as top-left but for an SIS lens with* $0.01 \leq y \leq 0.95$*. (Right) Evaluation time histograms for the surrogate (solid) and numerical method (dashed) for SIS.*

Given the impressive success of surrogate modeling to accurately and rapidly produce (unlensed) CBC templates, in this work, we assess its applicability in the context of generating microlensed GWs. We construct surrogate models of GWs microlensed by a PML and SIS lens. We consider a range of realistic lens masses and source locations. We achieve this by building time-domain surrogate magnification functions, Fourier transforming them, and then multiplying them with the unlensed frequency-domain GW waveform.

To assess the performance of the surrogate models, we compute mismatches between the surrogate microlensed waveforms and the corresponding, numerically evaluated, waveforms that were used to build the surrogate models, ensuring that the mismatches are not evaluated at lens parameter values used for surrogate construction. We do so over a grid of lens parameter values, and find that we are able to achieve mismatches in the range $\sim 10^{-8} - 10^{-4}$. Moreover, we measure the evaluation times of the microlensed waveforms in the frequency domain and find that they are typically $\mathcal{O}(10^{-2} - 10^{-1})$s for number of sample points ranging from $\sim (1.3 - 6.5) \times 10^4$. These benchmark-

ing tests demonstrate the power of surrogate modeling applied to microlensed GWs, suggesting that large-scale PE runs can be feasibly conducted using surrogate magnification functions.

It is worth pointing out that the rate-determining step in the computation of surrogate microlensed GWs in the frequency domain is, in fact, the Fourier transform, for which we employ `NumPy`'s FFT package [164]. The evaluation times of the time-domain surrogate waveforms are smaller than the FFT compuation by a couple of orders of magnitude. We find that, for the PML, the microlensed waveforms computed using the lookup table method in the frequency domain are marginally worse than the corresponding surrogate waveforms for large portions of the lensing parameter space considered.

The main advantage of surrogate modeling of microlensed GWs is that it does not intrinsically rely on any symmetries of the lensing potential. Indeed, if numerical solutions are able to provide time-domain magnification functions, it should be possible to construct corresponding surrogate models. Thus, in principle, our work should be readily extendable to asymmetric lensing configurations that better model those found in nature, such as a microlens embedded in a macropotential (e.g., an IMBH inside a galaxy-scale lens). However, constructing surrogate models for realistic lenses needs to mitigate an important problem.

Caustics – curves in the source plane where the image magnification formally diverges – demarcate distinct regions in that plane. These regions differ from each other in the number of images[4] that will be produced if the source is positioned in those regions. Abrupt changes in the number of images when crossing over caustics correspond to non-smooth changes in the shape of the time-domain magnification function as the source position changes. Indeed, even in the case of SIS lens, we restricted ourselves to lens parameters that ensure that exactly two images are produced. A possible workaround is to build separate surrogate models for each region in the lens plane containing a fixed number of images. Modeling the shape of the caustics poses an additional challenge. It is straightforward for symmetric lensing potentials but difficult for asymmetric systems - especially when several microlenses are embedded in a macropotential. We leave the surrogate modeling of such lensing configurations for future work. In addition, the accuracy of the model depends on the quality of the training data, which in turn relies on the numerical method and the image-finding algorithm (for peak reconstruction and amplitude regularization). Potential inaccuracies at high frequencies can be mitigated by increasing the resolution near the peaks of $\widetilde{\mathcal{F}}(t)$. Future work will focus on further refining these aspects for enhanced performance.

[4] *In the geometric-optics limit*

6

CONCLUSION AND FUTURE OUTLOOK

The direct detection of GWs by the current generation of ground-based interferometric detectors has advanced our understanding of astrophysics, cosmology and fundamental physics. CBCs being the primary sources of GWs among the current detections, have enabled exploration of compact binary properties, population properties of the compact objects, as well as the nature of these objects. Additionally, GWs provide access to extreme gravity regimes, thus, allowing stringent tests of GR in strong field. GWs also serve as independent cosmological probes at intermediate redshifts. The catalog of detected GWs is expanding with the ongoing O4 observing run, and further rapid increase in the number of detected events is expected with the addition of future generations of detectors. As a result, the precision and diversity of science that can be done with GWs will continue to grow.

Detection of lensed GWs promises to broaden this scientific reach even further, potentially complementing EM lensing. Because the wavelength of GW is typically much larger than EM waves, this allows us to explore lensing in the diffraction regime (i.e., microlensing). These microlensing effects enable the probe of previously unobserved lens populations. In this context, this thesis develops and applies microlensing of GWs in probing the nature and environment of compact objects. Moreover, GW microlensing allows testing alternative theories of gravity and put upper limits on the fraction of dark matter as compact objects. We also show the application of surrogate modeling in generating faster microlensed waveforms, opening the window towards large-scale parameter inference of astrophysical lenses.

In Chapter 3, we explore the potential of GW microlensing observations to constrain the effective charge of compact objects. We derive the lensing potential for a compact object lens whose external spacetime is described by RN metric parameterized by the lens mass and an effective charge. The effect of charge is incorporated in the wave-optics magnification function, which we numerically compute using a newly developed method. The various interpretations of this effective charge allows us to probe electric charge, naked singularities and several classes of alternative theories of gravity. Although detection of the electric charge of BHs via microlensing remains challenging, our forecasts suggest that future observations will be able to place meaningful constraints on the effective charge of exotic compact objects and on the

various modified theories of gravity. These projections use an approximate likelihood – necessitated by the lack of computationally efficient methods for computing GW signals lensed by a charged lens – and assume a non-spinning lens. We keep the development of faster and accurate microlensed waveforms for charged lenses and probing the effect of spin as future works. We also neglect possible correlations between microlensing and other physical effects on GWs such as orbital eccentricity or precession of the binary source. Moreover, we ignore the possible degeneracies between microlensing due to other astrophysically relevant lens models. We leave tesing the validity of these simplifications and refining the results for future.

Current microlensing searches, in general, assume the lens to be isolated. Non-observation of GW microlensing is further used to put upper limits on $f_{\rm DM}$ (composed primarily of PBHs). Chapter 4 investigates the effects of this assumption on microlensing searches. Specifically, we look at the effect on microlensing signatures due to lenses embedded in a host galaxy. We model the galaxy as SIS and assume that these PBH lenses follow the spatial distribution of the underlying galactic DM halo. We generate a mock distribution of such lens configurations and find that statistically, the presence of the external galaxy causes a loss in the Bayes factor, especially for large microlens masses. This results in a degradation of the efficiency of the microlensing searches. We expect that this effect will change the existing constraints on $f_{\rm DM}$. However, we keep a detailed analysis for this as a future work. Incorporating realistic galaxy models, such as those with elliptical mass distributions or substructures could lead to additional modifications in the microlensed signals leading to further loss of Bayes factor. Future studies will explore these effects.

Finally, Chapter 5 addresses the computational challenges of Bayesian parameter estimation for microlensed waveforms. We show that the technique of surrogate modeling can be applied to model the regularized time-domain magnification functions. This method evaluates the waveforms from the underlying reduced basis in the lens parameter space and the empirical nodes in time. We benchmark the efficiency of surrogate modeling in generating fast and accurate microlensed waveforms for spherically symmetric lens configurations, viz., PML and SIS. The speedup is promising to enable large-scale parameter inference of microlensed signals. Extending this work for complicated and more realistic lenses will enable the search for a broader range of lens model candidates in the GW data and subsequent parameter inference.

A

EXPECTED LIKELIHOOD IN THE HIGH-SNR LIMIT

We assume the detector output is of the form

$$d(f) = \widetilde{h}_{\rm tr}(f) + \widetilde{n}(f) \,, \tag{A.1}$$

consisting of a true signal $\widetilde{h}_{\rm tr}(f) \equiv \widetilde{h}(f;\boldsymbol{\theta}_{\rm tr})$ with signal parameters $\boldsymbol{\theta}_{\rm tr}$, and a specific realization of a stationary, zero-mean Gaussian noise $\widetilde{n}(f)$[1] . In this appendix, we summarize the key steps leading to the noise-averaged likelihood in the limit of large signal-to-noise ratio (SNR).[2]

[1] *It satisfies* $\widetilde{n}(-f) = \widetilde{n}^*(f)$.

[2] *Refer to Vallisneri [293] for a detailed study.*

We define the noise-weighted inner product between any two complex waveforms $a(f)$ and $b(f)$ as

$$(a|b) \equiv 2\int_0^\infty \frac{a(f)b^*(f) + a^*(f)b(f)}{S_n(f)} \,, \tag{A.2}$$

where * denotes complex conjugation and $S_n(f)$ is the one-sided power spectral density (PSD) defined as [116]

$$\langle \widetilde{n}^*(f)\, \widetilde{n}(f')\rangle_n = \frac{1}{2} S_n(f)\, \delta(f - f') \,. \tag{A.3}$$

Here $\langle \dots \rangle_n$ is the ensemble average over many possible noise realizations[3] .

[3] *Assuming ergodicity, the ensemble average is replaced by a time average.*

Under the hypothesis $\mathcal{H}$ that the data contain a signal $\widetilde{h}(\boldsymbol{\theta}) \equiv \widetilde{h}(f;\boldsymbol{\theta},\mathcal{H})$, the likelihood can be defined in terms of inner product as (see, e.g. Maggiore [208])

$$p(d|\boldsymbol{\theta},\mathcal{H}) \propto \exp\left[-\frac{1}{2}\left(d - \widetilde{h}(\boldsymbol{\theta}) \,\middle|\, d - \widetilde{h}(\boldsymbol{\theta})\right)\right] \,, \tag{A.4}$$

Evaluating the expectation value of the log-likelihood over noise realizations, and using the properties of Gaussian noise, we obtain

$$\langle \log p(d|\boldsymbol{\theta},\mathcal{H})\rangle_n = -\frac{1}{2}\langle \left(d - \widetilde{h}(\boldsymbol{\theta})|d - \widetilde{h}(\boldsymbol{\theta})\right)\rangle_n + \text{const} \tag{A.5}$$

$$= -\frac{1}{2}\left(\left(\widetilde{h}_{\rm tr} - \widetilde{h}(\boldsymbol{\theta})|\widetilde{h}_{\rm tr} - \widetilde{h}(\boldsymbol{\theta})\right) + \langle (n|n)\rangle_n\right) + \text{const} \,. \tag{A.6}$$

The noise term $\langle (n|n)\rangle_n$ is independent of $\boldsymbol{\theta}$ and can be absorbed into the normalization.

The optimal SNR for the true signal is defined as

$$\rho^2 \equiv (\widetilde{h}_{\rm tr}|\widetilde{h}_{\rm tr}) \ . \tag{A.7}$$

The match $\mathcal{M}(\boldsymbol{\theta}_{\rm tr}, \boldsymbol{\theta})$ between the normalized true signal and the normalized template[4] is given by (see e.g., Chatziioannou et al. [101])

[4] *Match is maximized over the arrival time and orbital phase of the signals.*

$$\mathcal{M}(\boldsymbol{\theta}_{\rm tr}, \boldsymbol{\theta}) \equiv \frac{(\widetilde{h}_{\rm tr}|\widetilde{h}(\boldsymbol{\theta}))}{\sqrt{(\widetilde{h}_{\rm tr}|\widetilde{h}_{\rm tr})\,(\widetilde{h}(\boldsymbol{\theta})|\widetilde{h}(\boldsymbol{\theta}))}} \ . \tag{A.8}$$

The match quantifies the similarity between two waveforms, with $\mathcal{M} = 1$ indicating perfect agreement. If the template is normalized such that $(\widetilde{h}(\boldsymbol{\theta})|\widetilde{h}(\boldsymbol{\theta})) \simeq (\widetilde{h}_{\rm tr}|\widetilde{h}_{\rm tr}) = \rho^2$, then

$$(\widetilde{h}_{\rm tr}|\widetilde{h}(\boldsymbol{\theta})) = \rho^2 \mathcal{M}(\boldsymbol{\theta}_{\rm tr}, \boldsymbol{\theta}) \ . \tag{A.9}$$

Expanding the inner product,

$$\begin{aligned}(\widetilde{h}_{\rm tr} - \widetilde{h}(\boldsymbol{\theta})|\widetilde{h}_{\rm tr} - \widetilde{h}(\boldsymbol{\theta})) &= (\widetilde{h}_{\rm tr}|\widetilde{h}_{\rm tr}) + (\widetilde{h}(\boldsymbol{\theta})|\widetilde{h}(\boldsymbol{\theta})) - 2(\widetilde{h}_{\rm tr}|\widetilde{h}(\boldsymbol{\theta})) &\text{(A.10a)}\\ &= 2\rho^2(1 - \mathcal{M}(\boldsymbol{\theta}_{\rm tr}, \boldsymbol{\theta})) \ . &\text{(A.10b)}\end{aligned}$$

Therefore, the expected likelihood becomes

$$\langle p(d|\boldsymbol{\theta}, \mathcal{H})\rangle_n \propto \exp\left[-\rho^2(1 - \mathcal{M}(\boldsymbol{\theta}_{\rm tr}, \boldsymbol{\theta}))\right] \ . \tag{A.11}$$

This expression shows that, in the high-SNR limit, the likelihood is sharply peaked around the maximum match between the template and the true signal, with the width of the peak determined by the SNR.

B

LOSS OF BAYES FACTOR WITH INCORRECT MODELS IN HIGH-SNR LIMIT

In this appendix, we analyze how using an *incorrect* or *alternative* model, instead of the *true* model, affects the Bayes factor in the context of microlensing detection in GW signals.[1]

[1] *Our calculations follow the methods described in Cornish et al. [110] and Vallisneri [294].*

Suppose a GW signal has been microlensed, and the true parameters of the microlensed waveform are denoted by $\boldsymbol{\theta}_{\rm tr} = \{\boldsymbol{\theta}_0^b, \boldsymbol{\theta}_0^\ell\}$, where:

- $\boldsymbol{\theta}_0^b$ are the intrinsic binary parameters (such as masses and spins),
- $\boldsymbol{\theta}_0^\ell$ are the lens parameters and the source position.

We consider two microlensing models, M_1 and M_2. For each model M_i ($i = 1, 2$), the parameters are $\boldsymbol{\theta}_i = \{\boldsymbol{\theta}_i^b, \boldsymbol{\theta}_i^\ell\}$.

Assuming the SNR ρ is large, the expected likelihood of observing data d given model M_i and parameters $\boldsymbol{\theta}_i$ is approximated by (see Eq. (A.11)):

$$p(d|\boldsymbol{\theta}_i, \mathcal{H}_i) = \exp\left[-\rho^2\left(1 - \mathcal{M}(\boldsymbol{\theta}_{\rm tr}, \boldsymbol{\theta}_i)\right)\right] \ , \tag{B.1}$$

upto a constant factor. Here $\mathcal{M}(\boldsymbol{\theta}_{\rm tr}, \boldsymbol{\theta}_i)$ is the match (see Eq.(A.8)) between the true waveform and the model waveform.

For the *unlensed* hypothesis $\mathcal{H}_{\rm U}$, where the signal is assumed not to be lensed, the likelihood is

$$p(d|\boldsymbol{\theta}_{\rm U}, \mathcal{H}_{\rm U}) \propto \exp\left[-\rho^2\left(1 - \mathcal{M}(\boldsymbol{\theta}_{\rm tr}, \boldsymbol{\theta}_{\rm U})\right)\right] \ , \tag{B.2}$$

where $\boldsymbol{\theta}_{\rm U}$ are the parameters of the unlensed waveform.

The *evidence* for each hypothesis is obtained by integrating the likelihood over all possible parameters:

$$p(d|\mathcal{H}_i) = \int d\boldsymbol{\theta}_i \, p(d|\boldsymbol{\theta}_i, \mathcal{H}_i) \simeq \exp\left[-\rho^2\left(1 - \mathrm{FF}_i\right)\right] \ , \tag{B.3a}$$

$$p(d|\mathcal{H}_{\rm U}) = \int d\boldsymbol{\theta}_{\rm U} \, p(d|\boldsymbol{\theta}_{\rm U}, \mathcal{H}_{\rm U}) \simeq \exp\left[-\rho^2\left(1 - \mathrm{FF}_{\rm U}\right)\right] \ , \tag{B.3b}$$

where the *fitting factor* (FF) is defined as the maximum match between the true waveform and the best-fit waveform from a given model:

$$\mathrm{FF}_i \equiv \max_{\boldsymbol{\theta}_i} \mathcal{M}(\boldsymbol{\theta}_{\mathrm{tr}}, \boldsymbol{\theta}_i) \ , \tag{B.4a}$$

$$\mathrm{FF}_{\mathrm{U}} \equiv \max_{\boldsymbol{\theta}_{\mathrm{U}}} \mathcal{M}(\boldsymbol{\theta}_{\mathrm{tr}}, \boldsymbol{\theta}_{\mathrm{U}}) \ . \tag{B.4b}$$

A fitting factor of 1 means the model can perfectly reproduce the true signal.

The *Bayes factor* comparing the evidence for the lensed model to the unlensed model[2] is given by

$$\mathcal{B}^i_{\mathrm{U}} \equiv \frac{p(d|\mathcal{H}_i)}{p(d|\mathcal{H}_{\mathrm{U}})} \simeq \exp\left[-\rho^2\left(\mathrm{FF}_{\mathrm{U}} - \mathrm{FF}_i\right)\right] \ . \tag{B.5}$$

A higher Bayes factor indicates stronger preference for the lensed model.

Suppose M_1 is the *true* model (M_{tr}), and M_2 is an *alternative* (incorrect) model (M_{alt}). For the true model, $\mathrm{FF}_{\mathrm{tr}} = 1$. This gives the Bayes factors:

$$\ln \mathcal{B}^{\mathrm{tr}}_{\mathrm{U}} \simeq \rho^2\left(1 - \mathrm{FF}_{\mathrm{U}}\right) \ , \tag{B.6a}$$

$$\ln \mathcal{B}^{\mathrm{alt}}_{\mathrm{U}} \simeq \rho^2\left(\mathrm{FF}_{\mathrm{alt}} - \mathrm{FF}_{\mathrm{U}}\right) \ , \tag{B.6b}$$

where $\mathrm{FF}_{\mathrm{alt}}$ is the fitting factor for the alternative model.

To quantify the reduction in Bayes factor when using an alternative model, we define the *loss factor* as

$$\mathrm{L.F.} \equiv \frac{\mathcal{B}^{\mathrm{alt}}_{\mathrm{U}}}{\mathcal{B}^{\mathrm{tr}}_{\mathrm{U}}} \simeq \exp\left[-\rho^2\left(1 - \mathrm{FF}_{\mathrm{alt}}\right)\right] \ . \tag{B.7}$$

The loss factor measures how much the Bayes factor is reduced due to imperfect modeling. If $\mathrm{FF}_{\mathrm{alt}}$ is close to 1, the loss is small; if it is much less than 1, the loss is significant, especially at high SNR.

[2] *Formally, model comparison should be based on the odds – i.e., the Bayes factor weighted by the prior odds – rather than the Bayes factor alone. However, in our analysis we set the prior odds to unity.*

BIBLIOGRAPHY

[1] J. Aasi et al. "Gravitational waves from known pulsars: results from the initial detector era." In: *Astrophys. J.* 785 (2014), p. 119. DOI: 10.1088/0004-637X/785/2/119. arXiv: 1309.4027 [astro-ph.HE].

[2] J. Aasi et al. "Advanced LIGO." In: *Class. Quant. Grav.* 32 (2015), p. 074001. DOI: 10.1088/0264-9381/32/7/074001. arXiv: 1411.4547 [gr-qc].

[3] B. P. Abbott et al. "Observation of Gravitational Waves from a Binary Black Hole Merger." In: *Phys. Rev. Lett.* 116.6 (2016), p. 061102. DOI: 10.1103/PhysRevLett.116.061102. arXiv: 1602.03837 [gr-qc].

[4] B. P. Abbott et al. "Tests of general relativity with GW150914." In: *Phys. Rev. Lett.* 116.22 (2016). [Erratum: Phys.Rev.Lett. 121, 129902 (2018)], p. 221101. DOI: 10.1103/PhysRevLett.116.221101. arXiv: 1602.03841 [gr-qc].

[5] B. P. Abbott et al. "A gravitational-wave standard siren measurement of the Hubble constant." In: *Nature* 551.7678 (2017), pp. 85–88. DOI: 10.1038/nature24471. arXiv: 1710.05835 [astro-ph.CO].

[6] B. P. Abbott et al. "GW170817: Observation of Gravitational Waves from a Binary Neutron Star Inspiral." In: *Phys. Rev. Lett.* 119.16 (2017), p. 161101. DOI: 10.1103/PhysRevLett.119.161101. arXiv: 1710.05832 [gr-qc].

[7] B. P. Abbott et al. "Gravitational Waves and Gamma-rays from a Binary Neutron Star Merger: GW170817 and GRB 170817A." In: *Astrophys. J. Lett.* 848.2 (2017), p. L13. DOI: 10.3847/2041-8213/aa920c. arXiv: 1710.05834 [astro-ph.HE].

[8] B. P. Abbott et al. "Multi-messenger Observations of a Binary Neutron Star Merger." In: *Astrophys. J. Lett.* 848.2 (2017), p. L12. DOI: 10.3847/2041-8213/aa91c9. arXiv: 1710.05833 [astro-ph.HE].

[9] B. P. Abbott et al. "All-sky search for continuous gravitational waves from isolated neutron stars using Advanced LIGO O2 data." In: *Phys. Rev. D* 100.2 (2019), p. 024004. DOI: 10.1103/PhysRevD.100.024004. arXiv: 1903.01901 [astro-ph.HE].

[10] B. P. Abbott et al. "GWTC-1: A Gravitational-Wave Transient Catalog of Compact Binary Mergers Observed by LIGO and Virgo during the First and Second Observing Runs." In: *Phys. Rev. X* 9.3 (2019), p. 031040. DOI: 10.1103/PhysRevX.9.031040. arXiv: 1811.12907 [astro-ph.HE].

[11] B. P. Abbott et al. "Search for Subsolar Mass Ultracompact Binaries in Advanced LIGO's Second Observing Run." In: *Phys. Rev. Lett.* 123.16 (2019), p. 161102. DOI: 10.1103/PhysRevLett.123.161102. arXiv: 1904.08976 [astro-ph.CO].

[12] B. P. Abbott et al. "Searches for Continuous Gravitational Waves from 15 Supernova Remnants and Fomalhaut b with Advanced LIGO." In: *Astrophys. J.* 875.2 (2019). [Erratum: Astrophys.J. 918, 91 (2021)], p. 122. DOI: 10.3847/1538-4357/ab113b. arXiv: 1812.11656 [astro-ph.HE].

[13] B. P. Abbott et al. "Tests of General Relativity with GW170817." In: *Phys. Rev. Lett.* 123.1 (2019), p. 011102. DOI: 10.1103/PhysRevLett.123.011102. arXiv: 1811.00364 [gr-qc].

[14] B. P. Abbott et al. "Tests of General Relativity with the Binary Black Hole Signals from the LIGO-Virgo Catalog GWTC-1." In: *Phys. Rev. D* 100.10 (2019), p. 104036. DOI: 10.1103/PhysRevD.100.104036. arXiv: 1903.04467 [gr-qc].

[15] B. P. Abbott et al. "GW190425: Observation of a Compact Binary Coalescence with Total Mass $\sim 3.4 M_{\odot}$." In: *Astrophys. J. Lett.* 892.1 (2020), p. L3. DOI: 10.3847/2041-8213/ab75f5. arXiv: 2001.01761 [astro-ph.HE].

[16] B. Abbott et al. "Upper limits on gravitational wave bursts in LIGO's second science run." In: *Phys. Rev. D* 72 (2005), p. 062001. DOI: 10.1103/PhysRevD.72.062001. arXiv: gr-qc/0505029.

[17] Benjamin P Abbott et al. "Exploring the Sensitivity of Next Generation Gravitational Wave Detectors." In: *Class. Quant. Grav.* 34.4 (2017), p. 044001. DOI: 10.1088/1361-6382/aa51f4. arXiv: 1607.08697 [astro-ph.IM].

[18] Benjamin P. Abbott et al. "First search for gravitational waves from known pulsars with Advanced LIGO." In: *Astrophys. J.* 839.1 (2017). [Erratum: Astrophys.J. 851, 71 (2017)], p. 12. DOI: 10.3847/1538-4357/aa677f. arXiv: 1701.07709 [astro-ph.HE].

[19] Benjamin P. Abbott et al. "Search for Tensor, Vector, and Scalar Polarizations in the Stochastic Gravitational-Wave Background." In: *Phys. Rev. Lett.* 120.20 (2018), p. 201102. DOI: 10.1103/PhysRevLett.120.201102. arXiv: 1802.10194 [gr-qc].

[20] R. Abbott et al. "GW190521: A Binary Black Hole Merger with a Total Mass of $150 M_{\odot}$." In: *Phys. Rev. Lett.* 125.10 (2020), p. 101102. DOI: 10.1103/PhysRevLett.125.101102. arXiv: 2009.01075 [gr-qc].

[21] R. Abbott et al. "GW190814: Gravitational Waves from the Coalescence of a 23 Solar Mass Black Hole with a 2.6 Solar Mass Compact Object." In: *Astrophys. J. Lett.* 896.2 (2020), p. L44. DOI: 10.3847/2041-8213/ab960f. arXiv: 2006.12611 [astro-ph.HE].

[22] R. Abbott et al. "Properties and Astrophysical Implications of the 150 $M_{\odot}$ Binary Black Hole Merger GW190521." In: *Astrophys. J. Lett.* 900.1 (2020), p. L13. DOI: 10.3847/2041-8213/aba493. arXiv: 2009.01190 [astro-ph.HE].

[23] R. Abbott et al. "All-sky search for long-duration gravitational-wave bursts in the third Advanced LIGO and Advanced Virgo run." In: *Phys. Rev. D* 104.10 (2021), p. 102001. DOI: 10.1103/PhysRevD.104.102001. arXiv: 2107.13796 [gr-qc].

[24] R. Abbott et al. "All-sky search for short gravitational-wave bursts in the third Advanced LIGO and Advanced Virgo run." In: *Phys. Rev. D* 104.12 (2021), p. 122004. DOI: 10.1103/PhysRevD.104.122004. arXiv: 2107.03701 [gr-qc].

[25] R. Abbott et al. "GWTC-2: Compact Binary Coalescences Observed by LIGO and Virgo During the First Half of the Third Observing Run." In: *Phys. Rev. X* 11 (2021), p. 021053. DOI: 10.1103/PhysRevX.11.021053. arXiv: 2010.14527 [gr-qc].

[26] R. Abbott et al. "GWTC-3: Compact Binary Coalescences Observed by LIGO and Virgo During the Second Part of the Third Observing Run." In: (Nov. 2021). arXiv: 2111.03606 [gr-qc].

[27] R. Abbott et al. "Observation of Gravitational Waves from Two Neutron Star–Black Hole Coalescences." In: *Astrophys. J. Lett.* 915.1 (2021), p. L5. DOI: 10.3847/2041-8213/ac082e. arXiv: 2106.15163 [astro-ph.HE].

[28] R. Abbott et al. "Searches for Continuous Gravitational Waves from Young Supernova Remnants in the Early Third Observing Run of Advanced LIGO and Virgo." In: *Astrophys. J.* 921.1 (2021), p. 80. DOI: 10.3847/1538-4357/ac17ea. arXiv: 2105.11641 [astro-ph.HE].

[29] R. Abbott et al. "Tests of General Relativity with GWTC-3." In: (Dec. 2021). arXiv: 2112.06861 [gr-qc].

[30] R. Abbott et al. "Tests of general relativity with binary black holes from the second LIGO-Virgo gravitational-wave transient catalog." In: *Phys. Rev. D* 103.12 (2021), p. 122002. DOI: 10.1103/PhysRevD.103.122002. arXiv: 2010.14529 [gr-qc].

[31] R. Abbott et al. "Upper limits on the isotropic gravitational-wave background from Advanced LIGO and Advanced Virgo's third observing run." In: *Phys. Rev. D* 104.2 (2021), p. 022004. DOI: 10.1103/PhysRevD.104.022004. arXiv: 2101.12130 [gr-qc].

[32] R. Abbott et al. "All-sky search for continuous gravitational waves from isolated neutron stars using Advanced LIGO and Advanced Virgo O3 data." In: *Phys. Rev. D* 106.10 (2022), p. 102008. DOI: 10.1103/PhysRevD.106.102008. arXiv: 2201.00697 [gr-qc].

[33] R. Abbott et al. "Searches for Gravitational Waves from Known Pulsars at Two Harmonics in the Second and Third LIGO-Virgo Observing Runs." In: *Astrophys. J.* 935.1 (2022), p. 1. DOI: 10.3847/1538-4357/ac6acf. arXiv: 2111.13106 [astro-ph.HE].

[34] R. Abbott et al. "Constraints on the Cosmic Expansion History from GWTC–3." In: *Astrophys. J.* 949.2 (2023), p. 76. DOI: 10.3847/1538-4357/ac74bb. arXiv: 2111.03604 [astro-ph.CO].

[35] R. Abbott et al. "Population of Merging Compact Binaries Inferred Using Gravitational Waves through GWTC-3." In: *Phys. Rev. X* 13.1 (2023), p. 011048. DOI: 10.1103/PhysRevX.13.011048. arXiv: 2111.03634 [astro-ph.HE].

[36] R. Abbott et al. "Search for gravitational-lensing signatures in the full third observing run of the LIGO-Virgo network." In: (Apr. 2023). arXiv: 2304.08393 [gr-qc].

[37] R. Abbott et al. "GWTC-2.1: Deep extended catalog of compact binary coalescences observed by LIGO and Virgo during the first half of the third observing run." In: *Phys. Rev. D* 109.2 (2024), p. 022001. DOI: 10.1103/PhysRevD.109.022001. arXiv: 2108.01045 [gr-qc].

[38] F. Acernese. "The Advanced Virgo detector." In: *J. Phys. Conf. Ser.* 610.1 (2015). Ed. by Giacomo Ciani, John W. Conklin, and Guido Mueller, p. 012014. DOI: 10.1088/1742-6596/610/1/012014.

[39] K. Ackley et al. "Neutron Star Extreme Matter Observatory: A kilohertz-band gravitational-wave detector in the global network." In: *Publ. Astron. Soc. Austral.* 37 (2020), e047. DOI: 10.1017/pasa.2020.39. arXiv: 2007.03128 [astro-ph.HE].

[40] R. X. Adhikari et al. "A cryogenic silicon interferometer for gravitational-wave detection." In: *Class. Quant. Grav.* 37.16 (2020), p. 165003. DOI: 10.1088/1361-6382/ab9143. arXiv: 2001.11173 [astro-ph.IM].

[41] Niayesh Afshordi et al. "Waveform Modelling for the Laser Interferometer Space Antenna." In: (Nov. 2023). arXiv: 2311.01300 [gr-qc].

[42] Gabriella Agazie et al. "The NANOGrav 15 yr Data Set: Evidence for a Gravitational-wave Background." In: *Astrophys. J. Lett.* 951.1 (2023), p. L8. DOI: 10.3847/2041-8213/acdac6. arXiv: 2306.16213 [astro-ph.HE].

[43] N. Aghanim et al. "Planck 2018 results. VI. Cosmological parameters." In: *Astron. Astrophys.* 641 (2020). [Erratum: Astron.Astrophys. 652, C4 (2021)], A6. DOI: 10.1051/0004-6361/201833910. arXiv: 1807.06209 [astro-ph.CO].

[44] Parameswaran Ajith et al. "Phenomenological template family for black-hole coalescence waveforms." In: *Class. Quant. Grav.* 24 (2007). Ed. by B. Krishnan, M. A. Papa, and Bernard F. Schutz, S689–S700. DOI: 10.1088/0264-9381/24/19/S31. arXiv: 0704.3764 [gr-qc].

[45] T. Akutsu et al. "Overview of KAGRA: Detector design and construction history." In: *PTEP* 2021.5 (2021), 05A101. DOI: 10.1093/ptep/ptaa125. arXiv: 2005.05574 [physics.ins-det].

[46] A. N. Aliev and A. E. Gumrukcuoglu. "Charged rotating black holes on a 3-brane." In: *Phys. Rev. D* 71 (2005), p. 104027. DOI: 10.1103/PhysRevD.71.104027. arXiv: hep-th/0502223.

[47] Bruce Allen and Joseph D. Romano. "Detecting a stochastic background of gravitational radiation: Signal processing strategies and sensitivities." In: *Phys. Rev. D* 59 (1999), p. 102001. DOI: 10.1103/PhysRevD.59.102001. arXiv: gr-qc/9710117.

[48] Steven W. Allen, August E. Evrard, and Adam B. Mantz. "Cosmological Parameters from Observations of Galaxy Clusters." In: *Ann. Rev. Astron. Astrophys.* 49 (2011), pp. 409–470. DOI: 10.1146/annurev-astro-081710-102514. arXiv: 1103.4829 [astro-ph.CO].

[49] Pau Amaro-Seoane et al. "Laser Interferometer Space Antenna." In: (Feb. 2017). arXiv: 1702.00786 [astro-ph.IM].

[50] David Andriot and Gustavo Lucena Gómez. "Signatures of extra dimensions in gravitational waves." In: *JCAP* 06 (2017). [Erratum: JCAP 05, E01 (2019)], p. 048. DOI: 10.1088/1475-7516/2017/06/048. arXiv: 1704.07392 [hep-th].

[51] Iair Arcavi et al. "Optical emission from a kilonova following a gravitational-wave-detected neutron-star merger." In: *Nature* 551 (2017), p. 64. DOI: 10.1038/nature24291. arXiv: 1710.05843 [astro-ph.HE].

[52] Eugeny Babichev and Christos Charmousis. "Dressing a black hole with a time-dependent Galileon." In: *JHEP* 08 (2014), p. 106. DOI: 10.1007/JHEP08(2014)106. arXiv: 1312.3204 [gr-qc].

[53] Eugeny Babichev, Christos Charmousis, and Mokhtar Hassaine. "Charged Galileon black holes." In: *JCAP* 05 (2015), p. 031. DOI: 10.1088/1475-7516/2015/05/031. arXiv: 1503.02545 [gr-qc].

[54] M. Bailes et al. "Gravitational-wave physics and astronomy in the 2020s and 2030s." In: *Nature Rev. Phys.* 3.5 (2021), pp. 344–366. DOI: 10.1038/s42254-021-00303-8.

[55] Luca Baiotti. "Gravitational waves from neutron star mergers and their relation to the nuclear equation of state." In: *Prog. Part. Nucl. Phys.* 109 (2019), p. 103714. DOI: 10.1016/j.ppnp.2019.103714. arXiv: 1907.08534 [astro-ph.HE].

[56] Indrani Banerjee, Sumanta Chakraborty, and Soumitra SenGupta. "Excavating black hole continuum spectrum: Possible signatures of scalar hairs and of higher dimensions." In: *Phys. Rev. D* 96.8 (2017), p. 084035. DOI: 10.1103/PhysRevD.96.084035. arXiv: 1707.04494 [gr-qc].

[57] Indrani Banerjee, Sumanta Chakraborty, and Soumitra SenGupta. "Silhouette of M87*: A New Window to Peek into the World of Hidden Dimensions." In: *Phys. Rev. D* 101.4 (2020), p. 041301. DOI: 10.1103/PhysRevD.101.041301. arXiv: 1909.09385 [gr-qc].

[58] Indrani Banerjee, Sumanta Chakraborty, and Soumitra SenGupta. "Looking for extra dimensions in the observed quasi-periodic oscillations of black holes." In: *JCAP* 09 (2021), p. 037. DOI: 10.1088/1475-7516/2021/09/037. arXiv: 2105.06636 [gr-qc].

[59] Indrani Banerjee, Sumanta Chakraborty, and Soumitra SenGupta. "Hunting extra dimensions in the shadow of Sgr A*." In: *Phys. Rev. D* 106.8 (2022), p. 084051. DOI: 10.1103/PhysRevD.106.084051. arXiv: 2207.09003 [gr-qc].

[60] Christian Baraldo, Akio Hosoya, and Takahiro T. Nakamura. "Gravitationally induced interference of gravitational waves by a rotating massive object." In: *Phys. Rev. D* 59 (1999), p. 083001. DOI: 10.1103/PhysRevD.59.083001.

[61] Enrico Barausse and Kent Yagi. "Gravitation-Wave Emission in Shift-Symmetric Horndeski Theories." In: *Phys. Rev. Lett.* 115.21 (2015), p. 211105. DOI: 10.1103/PhysRevLett.115.211105. arXiv: 1509.04539 [gr-qc].

[62] Maxime Barrault, Yvon Maday, Ngoc Cuong Nguyen, and Anthony T. Patera. "An 'empirical interpolation' method: application to efficient reduced-basis discretization of partial differential equations." In: *Comptes Rendus. Mathématique* 339.9 (Oct. 2004), pp. 667–672. ISSN: 1778-3569. DOI: 10.1016/j.crma.2004.08.006. URL: http://dx.doi.org/10.1016/j.crma.2004.08.006.

[63] José Barrientos, Fabrizio Cordonier-Tello, Fernando Izaurieta, Perla Medina, Daniela Narbona, Eduardo Rodríguez, and Omar Valdivia. "Nonminimal couplings, gravitational waves, and torsion in Horndeski's theory." In: *Phys. Rev. D* 96.8 (2017), p. 084023. DOI: 10.1103/PhysRevD.96.084023. arXiv: 1703.09686 [gr-qc].

[64] Matthias Bartelmann. "Arcs from a universal dark matter halo profile." In: *Astron. Astrophys.* 313 (1996), pp. 697–702. arXiv: astro-ph/9602053.

[65] Matthias Bartelmann. "Gravitational Lensing." In: *Class. Quant. Grav.* 27 (2010), p. 233001. DOI: 10.1088/0264-9381/27/23/233001. arXiv: 1010.3829 [astro-ph.CO].

[66] S. Basak, A. Ganguly, K. Haris, S. Kapadia, A. K. Mehta, and P. Ajith. "Constraints on Compact Dark Matter from Gravitational Wave Microlensing." In: *Astrophys. J.* 926.2 (2022), p. L28. DOI: 10.3847/2041-8213/ac4dfa. arXiv: 2109.06456 [gr-qc].

[67] Soummyadip Basak, Aditya Kumar Sharma, Shasvath J. Kapadia, and Parameswaran Ajith. "Prospects for the Observation of Continuous Gravitational Waves from Spinning Neutron Stars Lensed by the Galactic Supermassive Black Hole." In: *Astrophys. J. Lett.* 942.2 (2023), p. L31. DOI: 10.3847/2041-8213/acab50. arXiv: 2205.00022 [gr-qc].

[68] Thomas W. Baumgarte and Stuart L. Shapiro. "Numerical relativity and compact binaries." In: *Phys. Rept.* 376 (2003), pp. 41–131. DOI: 10.1016/S0370-1573(02)00537-9. arXiv: gr-qc/0211028.

[69] C. L. Bennett et al. "Nine-Year Wilkinson Microwave Anisotropy Probe (WMAP) Observations: Final Maps and Results." In: *Astrophys. J. Suppl.* 208 (2013), p. 20. DOI: 10.1088/0067-0049/208/2/20. arXiv: 1212.5225 [astro-ph.CO].

[70] Gary Bernstein and Philippe Fischer. "Values of H_o from models of the gravitational lens 0957+561." In: *Astron. J.* 118 (1999), p. 14. DOI: 10.1086/300949. arXiv: astro-ph/9903274.

[71] Emanuele Berti, Kent Yagi, Huan Yang, and Nicolás Yunes. "Extreme Gravity Tests with Gravitational Waves from Compact Binary Coalescences: (II) Ringdown." In: *Gen. Rel. Grav.* 50.5 (2018), p. 49. DOI: 10.1007/s10714-018-2372-6. arXiv: 1801.03587 [gr-qc].

[72] Gianfranco Bertone and Dan Hooper. "History of dark matter." In: *Rev. Mod. Phys.* 90.4 (2018), p. 045002. DOI: 10.1103/RevModPhys.90.045002. arXiv: 1605.04909 [astro-ph.CO].

[73] Sourav Bhattacharya and Sumanta Chakraborty. "Constraining some Horndeski gravity theories." In: *Phys. Rev. D* 95.4 (2017), p. 044037. DOI: 10.1103/PhysRevD.95.044037. arXiv: 1607.03693 [gr-qc].

[74] Simeon Bird, Ilias Cholis, Julian B. Muñoz, Yacine Ali-Haïmoud, Marc Kamionkowski, Ely D. Kovetz, Alvise Raccanelli, and Adam G. Riess. "Did LIGO detect dark matter?" In: *Phys. Rev. Lett.* 116.20 (2016), p. 201301. DOI: 10.1103/PhysRevLett.116.201301. arXiv: 1603.00464 [astro-ph.CO].

[75] Jonathan Blackman, Scott E. Field, Chad R. Galley, Béla Szilágyi, Mark A. Scheel, Manuel Tiglio, and Daniel A. Hemberger. "Fast and Accurate Prediction of Numerical Relativity Waveforms from Binary Black Hole Coalescences Using Surrogate Models." In: *Phys. Rev. Lett.* 115.12 (2015), p. 121102. DOI: 10.1103/PhysRevLett.115.121102. arXiv: 1502.07758 [gr-qc].

[76] Jonathan Blackman, Scott E. Field, Mark A. Scheel, Chad R. Galley, Daniel A. Hemberger, Patricia Schmidt, and Rory Smith. "A Surrogate Model of Gravitational Waveforms from Numerical Relativity Simulations of Precessing Binary Black Hole Mergers." In: *Phys. Rev. D* 95.10 (2017), p. 104023. DOI: 10.1103/PhysRevD.95.104023. arXiv: 1701.00550 [gr-qc].

[77] Jonathan Blackman, Scott E. Field, Mark A. Scheel, Chad R. Galley, Christian D. Ott, Michael Boyle, Lawrence E. Kidder, Harald P. Pfeiffer, and Béla Szilágyi. "Numerical relativity waveform surrogate model for generically precessing binary black hole mergers." In: *Phys. Rev. D* 96.2 (2017), p. 024058. DOI: 10.1103/PhysRevD.96.024058. arXiv: 1705.07089 [gr-qc].

[78] Luc Blanchet. "Post-Newtonian Theory for Gravitational Waves." In: *Living Rev. Rel.* 17 (2014), p. 2. DOI: 10.12942/lrr-2014-2. arXiv: 1310.1528 [gr-qc].

[79] Joss Bland-Hawthorn and Ortwin Gerhard. "The Galaxy in Context: Structural, Kinematic, and Integrated Properties." In: *Ann. Rev. Astron. Astrophys.* 54.1 (2016), pp. 529–596. DOI: 10.1146/annurev-astro-081915-023441. arXiv: 1602.07702 [astro-ph.GA].

[80] Roger Blandford and Ramesh Narayan. "Fermat's principle, caustics, and the classification of gravitational lens images." In: *Astrophys. J.* 310 (1986), pp. 568–582. DOI: 10.1086/164709.

[81] Max Born and Emil Wolf. *Principles of optics*. Cambridge Univ. Pr., 1999. ISBN: 978-1-139-64418-1. DOI: 10.1017/CBO9781139644181.

[82] Gabriele Bozzola and Vasileios Paschalidis. "General Relativistic Simulations of the Quasicircular Inspiral and Merger of Charged Black Holes: GW150914 and Fundamental Physics Implications." In: *Phys. Rev. Lett.* 126.4 (2021), p. 041103. DOI: 10.1103/PhysRevLett.126.041103. arXiv: 2006.15764 [gr-qc].

[83] Floor S. Broekgaarden, Sharan Banagiri, and Ethan Payne. "Visualizing the Number of Existing and Future Gravitational-wave Detections from Merging Double Compact Objects." In: *Astrophys. J.* 969.2 (2024), p. 108. DOI: 10.3847/1538-4357/ad4709. arXiv: 2303.17628 [astro-ph.HE].

[84] James S. Bullock, Tsafrir S. Kolatt, Yair Sigad, Rachel S. Somerville, Andrey V. Kravtsov, Anatoly A. Klypin, Joel R. Primack, and Avishai Dekel. "Profiles of dark haloes. Evolution, scatter, and environment." In: *Mon. Not. Roy. Astron. Soc.* 321 (2001), pp. 559–575. DOI: 10.1046/j.1365-8711.2001.04068.x. arXiv: astro-ph/9908159.

[85] A. Buonanno and T. Damour. "Effective one-body approach to general relativistic two-body dynamics." In: *Phys. Rev. D* 59 (1999), p. 084006. DOI: 10.1103/PhysRevD.59.084006. arXiv: gr-qc/9811091.

[86] Craig Cahillane and Georgia Mansell. "Review of the Advanced LIGO Gravitational Wave Observatories Leading to Observing Run Four." In: *Galaxies* 10.1 (2022), p. 36. DOI: 10.3390/galaxies10010036. arXiv: 2202.00847 [gr-qc].

[87] E. Capote et al. "Advanced LIGO detector performance in the fourth observing run." In: *Phys. Rev. D* 111.6 (2025), p. 062002. DOI: 10.1103/PhysRevD.111.062002. arXiv: 2411.14607 [gr-qc].

[88] Salvatore Capozziello, P. A. Gonzalez, Emmanuel N. Saridakis, and Yerko Vasquez. "Exact charged black-hole solutions in D-dimensional f(T) gravity: torsion vs curvature analysis." In: *JHEP* 02 (2013), p. 039. DOI: 10.1007/JHEP02(2013)039. arXiv: 1210.1098 [hep-th].

[89] Vitor Cardoso, Kyriakos Destounis, Francisco Duque, Rodrigo Panosso Macedo, and Andrea Maselli. "Black holes in galaxies: Environmental impact on gravitational-wave generation and propagation." In: *Phys. Rev. D* 105.6 (2022), p. L061501. DOI: 10.1103/PhysRevD.105.L061501. arXiv: 2109.00005 [gr-qc].

[90] Bernard J. Carr and S. W. Hawking. "Black holes in the early Universe." In: *Mon. Not. Roy. Astron. Soc.* 168 (1974), pp. 399–415. DOI: 10.1093/mnras/168.2.399.

[91] Bernard Carr, Kazunori Kohri, Yuuiti Sendouda, and Jun'ichi Yokoyama. "Constraints on primordial black holes." In: *Rept. Prog. Phys.* 84.11 (2021), p. 116902. DOI: 10.1088/1361-6633/ac1e31. arXiv: 2002.12778 [astro-ph.CO].

[92] Bernard Carr and Florian Kuhnel. "Primordial Black Holes as Dark Matter: Recent Developments." In: *Ann. Rev. Nucl. Part. Sci.* 70 (2020), pp. 355–394. DOI: 10.1146/annurev-nucl-050520-125911. arXiv: 2006.02838 [astro-ph.CO].

[93] Gregorio Carullo, Danny Laghi, Nathan K. Johnson-McDaniel, Walter Del Pozzo, Oscar J. C. Dias, Mahdi Godazgar, and Jorge E. Santos. "Constraints on Kerr-Newman black holes from merger-ringdown gravitational-wave observations." In: *Phys. Rev. D* 105.6 (2022), p. 062009. DOI: 10.1103/PhysRevD.105.062009. arXiv: 2109.13961 [gr-qc].

[94] Sumanta Chakraborty, Kabir Chakravarti, Sukanta Bose, and Soumitra SenGupta. "Signatures of extra dimensions in gravitational waves from black hole quasinormal modes." In: *Phys. Rev. D* 97.10 (2018), p. 104053. DOI: 10.1103/PhysRevD.97.104053. arXiv: 1710.05188 [gr-qc].

[95] Sumanta Chakraborty and Soumitra SenGupta. "Solar system constraints on alternative gravity theories." In: *Phys. Rev. D* 89.2 (2014), p. 026003. DOI: 10.1103/PhysRevD.89.026003. arXiv: 1208.1433 [gr-qc].

[96] Sumanta Chakraborty and Soumitra SenGupta. "Strong gravitational lensing — A probe for extra dimensions and Kalb-Ramond field." In: *JCAP* 07 (2017), p. 045. DOI: 10.1088/1475-7516/2017/07/045. arXiv: 1611.06936 [gr-qc].

[97] Kabir Chakravarti, Sumanta Chakraborty, Khun Sang Phukon, Sukanta Bose, and Soumitra SenGupta. "Constraining extra-spatial dimensions with observations of GW170817." In: *Class. Quant. Grav.* 37.10 (2020), p. 105004. DOI: 10.1088/1361-6382/ab8355. arXiv: 1903.10159 [gr-qc].

[98] Andrew Chamblin, Harvey S. Reall, Hisa-aki Shinkai, and Tetsuya Shiromizu. "Charged brane world black holes." In: *Phys. Rev. D* 63 (2001), p. 064015. DOI: 10.1103/PhysRevD.63.064015. arXiv: hep-th/0008177.

[99] K. Chang and S. Refsdal. "Flux variations of QSO 0957+561 A, B and image splitting by stars near the light path." In: *Nature* 282 (1979), pp. 561–564. DOI: 10.1038/282561a0.

[100] Saifon Chaturantabut and Danny C. Sorensen. "Nonlinear Model Reduction via Discrete Empirical Interpolation." In: *SIAM Journal on Scientific Computing* 32.5 (Jan. 2010), pp. 2737–2764. ISSN: 1095-7197. DOI: 10.1137/090766498. URL: http://dx.doi.org/10.1137/090766498.

[101] K. Chatziioannou, T. Dent, M. Fishbach, F. Ohme, M. Pürrer, V. Raymond, and J. Veitch. "Compact binary coalescences: gravitational-wave astronomy with ground-based detectors." In: (Sept. 2024). arXiv: 2409.02037 [gr-qc].

[102] Mark H. Y. Cheung, Joseph Gais, Otto A. Hannuksela, and Tjonnie G. F. Li. "Stellar-mass microlensing of gravitational waves." In: *Mon. Not. Roy. Astron. Soc.* 503.3 (2021), pp. 3326–3336. DOI: 10.1093/mnras/stab579. arXiv: 2012.07800 [astro-ph.HE].

[103] Mark Ho-Yeuk Cheung, Ken K. Y. Ng, Miguel Zumalacárregui, and Emanuele Berti. "Probing minihalo lenses with diffracted gravitational waves." In: *Phys. Rev. D* 109.12 (2024), p. 124020. DOI: 10.1103/PhysRevD.109.124020. arXiv: 2403.13876 [gr-qc].

[104] Pierre Christian, Salvatore Vitale, and Abraham Loeb. "Detecting Stellar Lensing of Gravitational Waves with Ground-Based Observatories." In: *Phys. Rev. D* 98.10 (2018), p. 103022. DOI: 10.1103/PhysRevD.98.103022. arXiv: 1802.02586 [astro-ph.HE].

[105] Adrian Ka-Wai Chung and Tjonnie Guang Feng Li. "Lensing of gravitational waves as a novel probe of graviton mass." In: *Phys. Rev. D* 104.12 (2021), p. 124060. DOI: 10.1103/PhysRevD.104.124060. arXiv: 2106.09630 [gr-qc].

[106] Sebastien Clesse and Juan García-Bellido. "The clustering of massive Primordial Black Holes as Dark Matter: measuring their mass distribution with Advanced LIGO." In: *Phys. Dark Univ.* 15 (2017), pp. 142–147. DOI: 10.1016/j.dark.2016.10.002. arXiv: 1603.05234 [astro-ph.CO].

[107] Douglas Clowe, Marusa Bradac, Anthony H. Gonzalez, Maxim Markevitch, Scott W. Randall, Christine Jones, and Dennis Zaritsky. "A direct empirical proof of the existence of dark matter." In: *Astrophys. J. Lett.* 648 (2006), pp. L109–L113. DOI: 10.1086/508162. arXiv: astro-ph/0608407.

[108] Thomas E. Collett and David Bacon. "Testing the speed of gravitational waves over cosmological distances with strong gravitational lensing." In: *Phys. Rev. Lett.* 118.9 (2017), p. 091101. DOI: 10.1103/PhysRevLett.118.091101. arXiv: 1602.05882 [astro-ph.HE].

[109] Neil J. Cornish. "Heterodyned likelihood for rapid gravitational wave parameter inference." In: *Phys. Rev. D* 104.10 (2021), p. 104054. DOI: 10.1103/PhysRevD.104.104054. arXiv: 2109.02728 [gr-qc].

[110] Neil Cornish, Laura Sampson, Nicolas Yunes, and Frans Pretorius. "Gravitational Wave Tests of General Relativity with the Parameterized Post-Einsteinian Framework." In: *Phys. Rev. D* 84 (2011), p. 062003. DOI: 10.1103/PhysRevD.84.062003. arXiv: 1105.2088 [gr-qc].

[111] Roberto Cotesta, Sylvain Marsat, and Michael Pürrer. "Frequency domain reduced order model of aligned-spin effective-one-body waveforms with higher-order modes." In: *Phys. Rev. D* 101.12 (2020), p. 124040. DOI: 10.1103/PhysRevD.101.124040. arXiv: 2003.12079 [gr-qc].

[112] D. A. Coulter et al. "Swope Supernova Survey 2017a (SSS17a), the Optical Counterpart to a Gravitational Wave Source." In: *Science* 358 (2017), p. 1556. DOI: 10.1126/science.aap9811. arXiv: 1710.05452 [astro-ph.HE].

[113] P. S. Cowperthwaite et al. "The Electromagnetic Counterpart of the Binary Neutron Star Merger LIGO/Virgo GW170817. II. UV, Optical, and Near-infrared Light Curves and Comparison to Kilonova Models." In: *Astrophys. J. Lett.* 848.2 (2017), p. L17. DOI: 10.3847/2041-8213/aa8fc7. arXiv: 1710.05840 [astro-ph.HE].

[114] Jolien D. E. Creighton and Warren G. Anderson. *Gravitational-Wave Physics and Astronomy: An Introduction to Theory, Experiment and Data Analysis*. Wiley, Sept. 2011. ISBN: 9783527636037. DOI: 10.1002/9783527636037. URL: http://dx.doi.org/10.1002/9783527636037.

[115] Elena Cuoco et al. "Enhancing Gravitational-Wave Science with Machine Learning." In: *Mach. Learn. Sci. Tech.* 2.1 (2021), p. 011002. DOI: 10.1088/2632-2153/abb93a. arXiv: 2005.03745 [astro-ph.HE].

[116] Curt Cutler and Eanna E. Flanagan. "Gravitational waves from merging compact binaries: How accurately can one extract the binary's parameters from the inspiral wave form?" In: *Phys. Rev. D* 49 (1994), pp. 2658–2697. DOI: 10.1103/PhysRevD.49.2658. arXiv: gr-qc/9402014.

[117] Curt Cutler and Daniel E. Holz. "Ultra-high precision cosmology from gravitational waves." In: *Phys. Rev. D* 80 (2009), p. 104009. DOI: 10.1103/PhysRevD.80.104009. arXiv: 0906.3752 [astro-ph.CO].

[118] Naresh Dadhich, Roy Maartens, Philippos Papadopoulos, and Vahid Rezania. "Black holes on the brane." In: *Phys. Lett. B* 487 (2000), pp. 1–6. DOI: 10.1016/S0370-2693(00)00798-X. arXiv: hep-th/0003061.

[119] Liang Dai, Shun-Sheng Li, Barak Zackay, Shude Mao, and Youjun Lu. "Detecting Lensing-Induced Diffraction in Astrophysical Gravitational Waves." In: *Phys. Rev. D* 98.10 (2018), p. 104029. DOI: 10.1103/PhysRevD.98.104029. arXiv: 1810.00003 [gr-qc].

[120] Liang Dai and Tejaswi Venumadhav. "On the waveforms of gravitationally lensed gravitational waves." In: (Feb. 2017). arXiv: 1702.04724 [gr-qc].

[121] J. M. Diego, O. A. Hannuksela, P. L. Kelly, T. Broadhurst, K. Kim, T. G. F. Li, G. F. Smoot, and G. Pagano. "Observational signatures of microlensing in gravitational waves at LIGO/Virgo frequencies." In: *Astron. Astrophys.* 627 (2019), A130. DOI: 10.1051/0004-6361/201935490. arXiv: 1903.04513 [astro-ph.CO].

[122] Benedikt Diemer. "COLOSSUS: A python toolkit for cosmology, large-scale structure, and dark matter halos." In: *Astrophys. J. Suppl.* 239.2 (2018), p. 35. DOI: 10.3847/1538-4365/aaee8c. arXiv: 1712.04512 [astro-ph.CO].

[123] M. R. Drout et al. "Light Curves of the Neutron Star Merger GW170817/SSS17a: Implications for R-Process Nucleosynthesis." In: *Science* 358 (2017), pp. 1570–1574. DOI: 10.1126/science.aaq0049. arXiv: 1710.05443 [astro-ph.HE].

[124] F. W. Dyson, A. S. Eddington, and C. Davidson. "A Determination of the Deflection of Light by the Sun's Gravitational Field, from Observations Made at the Total Eclipse of May 29, 1919." In: *Phil. Trans. Roy. Soc. Lond. A* 220 (1920), pp. 291–333. DOI: 10.1098/rsta.1920.0009.

[125] D. M. Eardley and W. H. Press. "Astrophysical processes near black holes." In: *Ann. Rev. Astron. Astrophys.* 13 (1975), pp. 381–422. DOI: 10.1146/annurev.aa.13.090175.002121.

[126] Kazunari Eda, Yousuke Itoh, Sachiko Kuroyanagi, and Joseph Silk. "New Probe of Dark-Matter Properties: Gravitational Waves from an Intermediate-Mass Black Hole Embedded in a Dark-Matter Minispike." In: *Phys. Rev. Lett.* 110.22 (2013), p. 221101. DOI: 10.1103/PhysRevLett.110.221101. arXiv: 1301.5971 [gr-qc].

[127] Albert Einstein. "Approximative Integration of the Field Equations of Gravitation." In: *Sitzungsber. Preuss. Akad. Wiss. Berlin (Math. Phys.)* 1916 (1916), pp. 688–696.

[128] Albert Einstein. "Über Gravitationswellen." In: *Sitzungsber. Preuss. Akad. Wiss. Berlin (Math. Phys.)* 1918 (1918), pp. 154–167.

[129] Ernesto F. Eiroa, Gustavo E. Romero, and Diego F. Torres. "Reissner-Nordstrom black hole lensing." In: *Phys. Rev. D* 66 (2002), p. 024010. DOI: 10.1103/PhysRevD.66.024010. arXiv: gr-qc/0203049.

[130] Ernesto F. Eiroa and Carlos M. Sendra. "Strong deflection lensing by charged black holes in scalar–tensor gravity." In: *Eur. Phys. J. C* 74.11 (2014), p. 3171. DOI: 10.1140/epjc/s10052-014-3171-1. arXiv: 1408.3390 [gr-qc].

[131] Ernesto F. Eiroa and Diego F. Torres. "Strong field limit analysis of gravitational retro lensing." In: *Phys. Rev. D* 69 (2004), p. 063004. DOI: 10.1103/PhysRevD.69.063004. arXiv: gr-qc/0311013.

[132] Matthew Evans et al. "A Horizon Study for Cosmic Explorer: Science, Observatories, and Community." In: (Sept. 2021). arXiv: 2109.09882 [astro-ph.IM].

[133] P. A. Evans et al. "Swift and NuSTAR observations of GW170817: detection of a blue kilonova." In: *Science* 358 (2017), p. 1565. DOI: 10.1126/science.aap9580. arXiv: 1710.05437 [astro-ph.HE].

[134] Jose María Ezquiaga, Daniel E. Holz, Wayne Hu, Macarena Lagos, and Robert M. Wald. "Phase effects from strong gravitational lensing of gravitational waves." In: *Phys. Rev. D* 103.6 (2021), p. 064047. DOI: 10.1103/PhysRevD.103.064047. arXiv: 2008.12814 [gr-qc].

[135] Jose María Ezquiaga, Wayne Hu, and Rico K. L. Lo. "Identifying strongly lensed gravitational waves through their phase consistency." In: *Phys. Rev. D* 108.10 (2023), p. 103520. DOI: 10.1103/PhysRevD.108.103520. arXiv: 2308.06616 [astro-ph.CO].

[136] Xi-Long Fan, Kai Liao, Marek Biesiada, Aleksandra Piorkowska-Kurpas, and Zong-Hong Zhu. "Speed of Gravitational Waves from Strongly Lensed Gravitational Waves and Electromagnetic Signals." In: *Phys. Rev. Lett.* 118.9 (2017), p. 091102. DOI: 10.1103/PhysRevLett.118.091102. arXiv: 1612.04095 [gr-qc].

[137] Stephen M. Feeney, Hiranya V. Peiris, Andrew R. Williamson, Samaya M. Nissanke, Daniel J. Mortlock, Justin Alsing, and Dan Scolnic. "Prospects for resolving the Hubble constant tension with standard sirens." In: *Phys. Rev. Lett.* 122.6 (2019), p. 061105. DOI: 10.1103/PhysRevLett.122.061105. arXiv: 1802.03404 [astro-ph.CO].

[138] Job Feldbrugge, Ue-Li Pen, and Neil Turok. "Oscillatory path integrals for radio astronomy." In: *Annals Phys.* 451 (2023), p. 169255. DOI: 10.1016/j.aop.2023.169255. arXiv: 1909.04632 [astro-ph.HE].

[139] Justin C. Feng, Sumanta Chakraborty, and Vitor Cardoso. "Shielding a charged black hole." In: *Phys. Rev. D* 107.4 (2023), p. 044050. DOI: 10.1103/PhysRevD.107.044050. arXiv: 2211.05261 [gr-qc].

[140] Scott E. Field, Chad R. Galley, Frank Herrmann, Jan S. Hesthaven, Evan Ochsner, and Manuel Tiglio. "Reduced basis catalogs for gravitational wave templates." In: *Phys. Rev. Lett.* 106 (2011), p. 221102. DOI: 10.1103/PhysRevLett.106.221102. arXiv: 1101.3765 [gr-qc].

[141] Scott E. Field, Chad R. Galley, Jan S. Hesthaven, Jason Kaye, and Manuel Tiglio. "Fast prediction and evaluation of gravitational waveforms using surrogate models." In: *Phys. Rev. X* 4.3 (2014), p. 031006. DOI: 10.1103/PhysRevX.4.031006. arXiv: 1308.3565 [gr-qc].

[142] Andreas Finke, Stefano Foffa, Francesco Iacovelli, Michele Maggiore, and Michele Mancarella. "Cosmology with LIGO/Virgo dark sirens: Hubble parameter and modified gravitational wave propagation." In: *JCAP* 08 (2021), p. 026. DOI: 10.1088/1475-7516/2021/08/026. arXiv: 2101.12660 [astro-ph.CO].

[143] Andreas Finke, Stefano Foffa, Francesco Iacovelli, Michele Maggiore, and Michele Mancarella. "Probing modified gravitational wave propagation with strongly lensed coalescing binaries." In: *Phys. Rev. D* 104.8 (2021), p. 084057. DOI: 10.1103/PhysRevD.104.084057. arXiv: 2107.05046 [gr-qc].

[144] Eanna E. Flanagan and Scott A. Hughes. "The Basics of gravitational wave theory." In: *New J. Phys.* 7 (2005), p. 204. DOI: 10.1088/1367-2630/7/1/204. arXiv: gr-qc/0501041.

[145] Joan Fontbuté, Tomas Andrade, Raimon Luna, Juan Calderón Bustillo, Gonzalo Morrás, Santiago Jaraba, Juan García-Bellido, and Germán López Izquierdo. "Numerical-relativity surrogate model for hyperbolic encounters of black holes: Challenges in parameter estimation." In: *Phys. Rev. D* 111.4 (2025), p. 044024. DOI: 10.1103/PhysRevD.111.044024. arXiv: 2409.16742 [gr-qc].

[146] Bhooshan Gadre, Michael Pürrer, Scott E. Field, Serguei Ossokine, and Vijay Varma. "Fully precessing higher-mode surrogate model of effective-one-body waveforms." In: *Phys. Rev. D* 110.12 (2024), p. 124038. DOI: 10.1103/PhysRevD.110.124038. arXiv: 2203.00381 [gr-qc].

[147] Jonathan R. Gair, Michele Vallisneri, Shane L. Larson, and John G. Baker. "Testing General Relativity with Low-Frequency, Space-Based Gravitational-Wave Detectors." In: *Living Rev. Rel.* 16 (2013), p. 7. DOI: 10.12942/lrr-2013-7. arXiv: 1212.5575 [gr-qc].

[148] B. Scott Gaudi. "Microlensing Surveys for Exoplanets." In: *Annual Review of Astronomy and Astrophysics* 50.1 (Sept. 2012), pp. 411–453. ISSN: 1545-4282. DOI: 10.1146/annurev-astro-081811-125518. URL: http://dx.doi.org/10.1146/annurev-astro-081811-125518.

[149] Davide Gerosa, François Hébert, and Leo C. Stein. "Black-hole kicks from numerical-relativity surrogate models." In: *Phys. Rev. D* 97.10 (2018), p. 104049. DOI: 10.1103/PhysRevD.97.104049. arXiv: 1802.04276 [gr-qc].

[150] A. Goldstein et al. "An Ordinary Short Gamma-Ray Burst with Extraordinary Implications: Fermi-GBM Detection of GRB 170817A." In: *Astrophys. J. Lett.* 848.2 (2017), p. L14. DOI: 10.3847/2041-8213/aa8f41. arXiv: 1710.05446 [astro-ph.HE].

[151] Srashti Goyal, Harikrishnan D., Shasvath J. Kapadia, and Parameswaran Ajith. "Rapid identification of strongly lensed gravitational-wave events with machine learning." In: *Phys. Rev. D* 104.12 (2021), p. 124057. DOI: 10.1103/PhysRevD.104.124057. arXiv: 2106.12466 [gr-qc].

[152] Srashti Goyal, K. Haris, Ajit Kumar Mehta, and Parameswaran Ajith. "Testing the nature of gravitational-wave polarizations using strongly lensed signals." In: *Phys. Rev. D* 103.2 (2021), p. 024038. DOI: 10.1103/PhysRevD.103.024038. arXiv: 2008.07060 [gr-qc].

[153] Srashti Goyal, Aditya Vijaykumar, Jose Maria Ezquiaga, and Miguel Zumalacarregui. "Probing lens-induced gravitational-wave birefringence as a test of general relativity." In: *Phys. Rev. D* 108.2 (2023), p. 024052. DOI: 10.1103/PhysRevD.108.024052. arXiv: 2301.04826 [gr-qc].

[154] Rachel Gray et al. "Cosmological inference using gravitational wave standard sirens: A mock data analysis." In: *Phys. Rev. D* 101.12 (2020), p. 122001. DOI: 10.1103/PhysRevD.101.122001. arXiv: 1908.06050 [gr-qc].

[155] Gianfranco Grillo and James Cordes. "Wave asymptotics and their application to astrophysical plasma lensing." In: (Oct. 2018). arXiv: 1810.09058 [astro-ph.CO].

[156] Hua-Peng Gu, Hai-Tian Wang, and Lijing Shao. "Constraints on charged black holes from merger-ringdown signals in GWTC-3 and prospects for the Einstein Telescope." In: *Phys. Rev. D* 109.2 (2024), p. 024058. DOI: 10.1103/PhysRevD.109.024058. arXiv: 2310.10447 [gr-qc].

[157] Alec Gunny, Dylan Rankin, Jeffrey Krupa, Muhammed Saleem, Tri Nguyen, Michael Coughlin, Philip Harris, Erik Katsavounidis, Steven Timm, and Burt Holzman. "Hardware-accelerated Inference for Real-Time Gravitational-Wave Astronomy." In: *Nature Astron.* 6.5 (2022), pp. 529–536. DOI: 10.1038/s41550-022-01651-w. arXiv: 2108.12430 [gr-qc].

[158] Xiao Guo and Youjun Lu. "Convergence and Efficiency of Different Methods to Compute the Diffraction Integral for Gravitational Lensing of Gravitational Waves." In: *Phys. Rev. D* 102.12 (2020), p. 124076. DOI: 10.1103/PhysRevD.102.124076. arXiv: 2012.03474 [gr-qc].

[159] Pawan Kumar Gupta, Thomas F. M. Spieksma, Peter T. H. Pang, Gideon Koekoek, and Chris Van Den Broeck. "Bounding dark charges on binary black holes using gravitational waves." In: *Phys. Rev. D* 104.6 (2021), p. 063041. DOI: 10.1103/PhysRevD.104.063041. arXiv: 2107.12111 [gr-qc].

[160] O. A. Hannuksela, K. Haris, K. K. Y. Ng, S. Kumar, A. K. Mehta, D. Keitel, T. G. F. Li, and P. Ajith. "Search for gravitational lensing signatures in LIGO-Virgo binary black hole events." In: *Astrophys. J. Lett.* 874.1 (2019), p. L2. DOI: 10.3847/2041-8213/ab0c0f. arXiv: 1901.02674 [gr-qc].

[161] Otto A. Hannuksela, Thomas E. Collett, Mesut Çalışkan, and Tjonnie G. F. Li. "Localizing merging black holes with sub-arcsecond precision using gravitational-wave lensing." In: *Mon. Not. Roy. Astron. Soc.* 498.3 (2020), pp. 3395–3402. DOI: 10.1093/mnras/staa2577. arXiv: 2004.13811 [astro-ph.HE].

[162] K. Haris, Ajit Kumar Mehta, Sumit Kumar, Tejaswi Venumadhav, and Parameswaran Ajith. "Identifying strongly lensed gravitational wave signals from binary black hole mergers." In: (July 2018). arXiv: 1807.07062 [gr-qc].

[163] T. Harko and M. K. Mak. "Vacuum solutions of the gravitational field equations in the brane world model." In: *Phys. Rev. D* 69 (2004), p. 064020. DOI: 10.1103/PhysRevD.69.064020. arXiv: gr-qc/0401049.

[164] Charles R. Harris et al. "Array programming with NumPy." In: *Nature* 585.7825 (2020), pp. 357–362. DOI: 10.1038/s41586-020-2649-2. arXiv: 2006.10256 [cs.MS].

[165] R. w. Hellings and G. s. Downs. "Upper limits on the isotropic gravitational radiation background from pulsar timing analysis." In: *Astrophys. J. Lett.* 265 (1983), pp. L39–L42. DOI: 10.1086/183954.

[166] Jan S. Hesthaven, Benjamin Stamm, and Shun Zhang. "Efficient greedy algorithms for high-dimensional parameter spaces with applications to empirical interpolation and reduced basis methods." In: *ESAIM: Mathematical Modelling and Numerical Analysis* 48.1 (Jan. 2014), pp. 259–283. ISSN: 1290-3841. DOI: 10.1051/m2an/2013100. URL: http://dx.doi.org/10.1051/m2an/2013100.

[167] S. Hild et al. "Sensitivity Studies for Third-Generation Gravitational Wave Observatories." In: *Class. Quant. Grav.* 28 (2011), p. 094013. DOI: 10.1088/0264-9381/28/9/094013. arXiv: 1012.0908 [gr-qc].

[168] Christopher M. Hirata, Daniel E. Holz, and Curt Cutler. "Reducing the weak lensing noise for the gravitational wave Hubble diagram using the non-Gaussianity of the magnification distribution." In: *Phys. Rev. D* 81 (2010), p. 124046. DOI: 10.1103/PhysRevD.81.124046. arXiv: 1004.3988 [astro-ph.CO].

[169] Daniel E. Holz and Eric V. Linder. "Safety in numbers: Gravitational lensing degradation of the luminosity distance-redshift relation." In: *Astrophys. J.* 631 (2005), pp. 678–688. DOI: 10.1086/432085. arXiv: astro-ph/0412173.

[170] Wayne Hu and Scott Dodelson. "Cosmic Microwave Background Anisotropies." In: *Ann. Rev. Astron. Astrophys.* 40 (2002), pp. 171–216. DOI: 10.1146/annurev.astro.40.060401.093926. arXiv: astro-ph/0110414.

[171] Wen-Rui Hu and Yue-Liang Wu. "The Taiji Program in Space for gravitational wave physics and the nature of gravity." In: *Natl. Sci. Rev.* 4.5 (2017), pp. 685–686. DOI: 10.1093/nsr/nwx116.

[172] Lorenzo Iorio and Emmanuel N. Saridakis. "Solar system constraints on f(T) gravity." In: *Mon. Not. Roy. Astron. Soc.* 427 (2012), p. 1555. DOI: 10.1111/j.1365-2966.2012.21995.x. arXiv: 1203.5781 [gr-qc].

[173] Maximiliano Isi, Will M. Farr, Matthew Giesler, Mark A. Scheel, and Saul A. Teukolsky. "Testing the Black-Hole Area Law with GW150914." In: *Phys. Rev. Lett.* 127.1 (2021), p. 011103. DOI: 10.1103/PhysRevLett.127.011103. arXiv: 2012.04486 [gr-qc].

[174] Maximiliano Isi and Alan J. Weinstein. "Probing gravitational wave polarizations with signals from compact binary coalescences." In: (Oct. 2017). arXiv: 1710.03794 [gr-qc].

[175] Tousif Islam, Scott E. Field, Scott A. Hughes, Gaurav Khanna, Vijay Varma, Matthew Giesler, Mark A. Scheel, Lawrence E. Kidder, and Harald P. Pfeiffer. "Surrogate model for gravitational wave signals from nonspinning, comparable-to large-mass-ratio black hole binaries built on black hole perturbation theory waveforms calibrated to numerical relativity." In: *Phys. Rev. D* 106.10 (2022), p. 104025. DOI: 10.1103/PhysRevD.106.104025. arXiv: 2204.01972 [gr-qc].

[176] Tousif Islam, Scott E. Field, and Gaurav Khanna. "Remnant black hole properties from numerical-relativity-informed perturbation theory and implications for waveform modeling." In: *Phys. Rev. D* 108.6 (2023), p. 064048. DOI: 10.1103/PhysRevD.108.064048. arXiv: 2301.07215 [gr-qc].

[177] Tousif Islam, Vijay Varma, Jackie Lodman, Scott E. Field, Gaurav Khanna, Mark A. Scheel, Harald P. Pfeiffer, Davide Gerosa, and Lawrence E. Kidder. "Eccentric binary black hole surrogate models for the gravitational waveform and remnant properties: comparable mass, nonspinning case." In: *Phys. Rev. D* 103.6 (2021), p. 064022. DOI: 10.1103/PhysRevD.103.064022. arXiv: 2101.11798 [gr-qc].

[178] John David Jackson. *Classical Electrodynamics*. Wiley, 1998. ISBN: 978-0-471-30932-1.

[179] Souvik Jana, Shasvath J. Kapadia, Tejaswi Venumadhav, and Parameswaran Ajith. "Cosmography Using Strongly Lensed Gravitational Waves from Binary Black Holes." In: *Phys. Rev. Lett.* 130.26 (2023), p. 261401. DOI: 10.1103/PhysRevLett.130.261401. arXiv: 2211.12212 [astro-ph.CO].

[180] Souvik Jana, Shasvath J. Kapadia, Tejaswi Venumadhav, Surhud More, and Parameswaran Ajith. "Probing the nature of dark matter using strongly lensed gravitational waves from binary black holes." In: (Aug. 2024). arXiv: 2408.05290 [astro-ph.CO].

[181] Gemma Janssen et al. "Gravitational wave astronomy with the SKA." In: *PoS* AASKA14 (2015). Ed. by Tyler L. Bourke et al., p. 037. DOI: 10.22323/1.215.0037. arXiv: 1501.00127 [astro-ph.IM].

[182] F. Jenet et al. "The North American Nanohertz Observatory for Gravitational Waves." In: (Sept. 2009). arXiv: 0909.1058 [astro-ph.IM].

[183] Nathan K. Johnson-Mcdaniel, Arunava Mukherjee, Rahul Kashyap, Parameswaran Ajith, Walter Del Pozzo, and Salvatore Vitale. "Constraining black hole mimickers with gravitational wave observations." In: *Phys. Rev. D* 102 (2020), p. 123010. DOI: 10.1103/PhysRevD.102.123010. arXiv: 1804.08026 [gr-qc].

[184] Dylan L. Jow, Ue-Li Pen, and Job Feldbrugge. "Regimes in astrophysical lensing: refractive optics, diffractive optics, and the Fresnel scale." In: *Mon. Not. Roy. Astron. Soc.* 525.2 (2023), pp. 2107–2124. DOI: 10.1093/mnras/stad2332. arXiv: 2204.12004 [astro-ph.HE].

[185] Daniel Kasen, Brian Metzger, Jennifer Barnes, Eliot Quataert, and Enrico Ramirez-Ruiz. "Origin of the heavy elements in binary neutron-star mergers from a gravitational wave event." In: *Nature* 551 (2017), p. 80. DOI: 10.1038/nature24453. arXiv: 1710.05463 [astro-ph.HE].

[186] M. M. Kasliwal et al. "Illuminating Gravitational Waves: A Concordant Picture of Photons from a Neutron Star Merger." In: *Science* 358 (2017), p. 1559. DOI: 10.1126/science.aap9455. arXiv: 1710.05436 [astro-ph.HE].

[187] Seiji Kawamura et al. "Current status of space gravitational wave antenna DECIGO and B-DECIGO." In: *PTEP* 2021.5 (2021), 05A105. DOI: 10.1093/ptep/ptab019. arXiv: 2006.13545 [gr-qc].

[188] Charles R. Keeton. "A catalog of mass models for gravitational lensing." In: (Feb. 2001). arXiv: astro-ph/0102341.

[189] Sebastian Khan and Rhys Green. "Gravitational-wave surrogate models powered by artificial neural networks." In: *Phys. Rev. D* 103.6 (2021), p. 064015. DOI: 10.1103/PhysRevD.103.064015. arXiv: 2008.12932 [gr-qc].

[190] Jean-Paul Kneib and Priyamvada Natarajan. "Cluster Lenses." In: *Astron. Astrophys. Rev.* 19 (2011), p. 47. DOI: 10.1007/s00159-011-0047-3. arXiv: 1202.0185 [astro-ph.CO].

[191] Christopher S. Kochanek. "The implications of lenses for galaxy structure." In: *The Astrophysical Journal* 373 (June 1991), p. 354. ISSN: 1538-4357. DOI: 10.1086/170057. URL: http://dx.doi.org/10.1086/170057.

[192] Kostas D. Kokkotas and Bernd G. Schmidt. "Quasinormal modes of stars and black holes." In: *Living Rev. Rel.* 2 (1999), p. 2. DOI: 10.12942/lrr-1999-2. arXiv: gr-qc/9909058.

[193] Robert Kormann, Peter Schneider, and Matthias Bartelmann. "Isothermal elliptical gravitational lens models." In: *Astronomy and Astrophysics* 284 (1994), pp. 285–299.

[194] Savvas M. Koushiappas and Abraham Loeb. "Maximum redshift of gravitational wave merger events." In: *Phys. Rev. Lett.* 119.22 (2017), p. 221104. DOI: 10.1103/PhysRevLett.119.221104. arXiv: 1708.07380 [astro-ph.CO].

[195] Michael Kramer and David J. Champion. "The European Pulsar Timing Array and the Large European Array for Pulsars." In: *Class. Quant. Grav.* 30 (2013), p. 224009. DOI: 10.1088/0264-9381/30/22/224009.

[196] Koutarou Kyutoku, Masaru Shibata, and Keisuke Taniguchi. "Coalescence of black hole–neutron star binaries." In: *Living Rev. Rel.* 24.1 (2021), p. 5. DOI: 10.1007/s41114-021-00033-4. arXiv: 2110.06218 [astro-ph.HE].

[197] Kwun-Hang Lai, Otto A. Hannuksela, Antonio Herrera-Martín, Jose M. Diego, Tom Broadhurst, and Tjonnie G. F. Li. "Discovering intermediate-mass black hole lenses through gravitational wave lensing." In: *Phys. Rev. D* 98.8 (2018), p. 083005. DOI: 10.1103/PhysRevD.98.083005. arXiv: 1801.07840 [gr-qc].

[198] Calvin Leung, Dylan Jow, Prasenjit Saha, Liang Dai, Masamune Oguri, and Léon V. E. Koopmans. "Wave Optics, Interference, and Decoherence in Strong Gravitational Lensing." In: *Space Sci. Rev.* 221.2 (2025), p. 29. DOI: 10.1007/s11214-025-01157-7. arXiv: 2304.01202 [astro-ph.HE].

[199] Steven L. Liebling and Carlos Palenzuela. "Dynamical boson stars." In: *Living Rev. Rel.* 26.1 (2023), p. 1. DOI: 10.1007/s41114-023-00043-4. arXiv: 1202.5809 [gr-qc].

[200] Rico K. L. Lo and Ignacio Magana Hernandez. "Bayesian statistical framework for identifying strongly lensed gravitational-wave signals." In: *Phys. Rev. D* 107.12 (2023), p. 123015. DOI: 10.1103/PhysRevD.107.123015. arXiv: 2104.09339 [gr-qc].

[201] Joshua C. Long, Hilton W. Chan, Allison B. Churnside, Eric A. Gulbis, Michael C. M. Varney, and John C. Price. "Upper limits to submillimeter-range forces from extra space-time dimensions." In: *Nature* 421 (2003), pp. 922–925. DOI: 10.1038/nature01432. arXiv: hep-ph/0210004.

[202] Jun Luo et al. "TianQin: a space-borne gravitational wave detector." In: *Class. Quant. Grav.* 33.3 (2016), p. 035010. DOI: 10.1088/0264-9381/33/3/035010. arXiv: 1512.02076 [astro-ph.IM].

[203] Caio F. B. Macedo, Paolo Pani, Vitor Cardoso, and Luís C. B. Crispino. "Into the lair: gravitational-wave signatures of dark matter." In: *Astrophys. J.* 774 (2013), p. 48. DOI: 10.1088/0004-637X/774/1/48. arXiv: 1302.2646 [gr-qc].

[204] Jean-Pierre Macquart. "Scattering of gravitational radiation: Second order moments of the wave amplitude." In: *Astron. Astrophys.* 422 (2004), pp. 761–775. DOI: 10.1051/0004-6361:20034512. arXiv: astro-ph/0402661.

[205] Yvon Maday, Ngoc Cuong Nguyen, Anthony T. Patera, and S. H. Pau. "A general multipurpose interpolation procedure: the magic points." In: *Communications on Pure and Applied Analysis* 8.1 (2009), pp. 383–404. ISSN: 1553-5258. DOI: 10.3934/cpaa.2009.8.383. URL: http://dx.doi.org/10.3934/cpaa.2009.8.383.

[206] Hideki Maeda and Naresh Dadhich. "Matter without matter: Novel Kaluza-Klein spacetime in Einstein-Gauss-Bonnet gravity." In: *Phys. Rev. D* 75 (2007), p. 044007. DOI: 10.1103/PhysRevD.75.044007. arXiv: hep-th/0611188.

[207] Sourabh Magare, Shasvath J. Kapadia, Anupreeta More, Mukesh Kumar Singh, Parameswaran Ajith, and A. N. Ramprakash. "Gear Up for the Action Replay: Leveraging Lensing for Enhanced Gravitational-wave Early Warning." In: *Astrophys. J. Lett.* 955.2 (2023), p. L31. DOI: 10.3847/2041-8213/acf668. arXiv: 2302.02916 [astro-ph.HE].

[208] Michele Maggiore. *Gravitational Waves. Vol. 1: Theory and Experiments*. Oxford University Press, 2007. ISBN: 978-0-19-171766-6, 978-0-19-852074-0. DOI: 10.1093/acprof:oso/9780198570745.001.0001.

[209] Michele Maggiore et al. "Science Case for the Einstein Telescope." In: *JCAP* 03 (2020), p. 050. DOI: 10.1088/1475-7516/2020/03/050. arXiv: 1912.02622 [astro-ph.CO].

[210] Michele Mancarella, Edwin Genoud-Prachex, and Michele Maggiore. "Cosmology and modified gravitational wave propagation from binary black hole population models." In: *Phys. Rev. D* 105.6 (2022), p. 064030. DOI: 10.1103/PhysRevD.105.064030. arXiv: 2112.05728 [gr-qc].

[211] R. N. Manchester. "The International Pulsar Timing Array." In: *Class. Quant. Grav.* 30 (2013), p. 224010. DOI: 10.1088/0264-9381/30/22/224010. arXiv: 1309.7392 [astro-ph.IM].

[212] R. N. Manchester et al. "The Parkes Pulsar Timing Array Project." In: *Publ. Astron. Soc. Austral.* 30 (2013), p. 17. DOI: 10.1017/pasa.2012.017. arXiv: 1210.6130 [astro-ph.IM].

[213] Michela Mapelli. "Formation Channels of Single and Binary Stellar-Mass Black Holes." In: 2021. DOI: 10.1007/978-981-15-4702-7_16-1. arXiv: 2106.00699 [astro-ph.HE].

[214] Ben Margalit and Brian D. Metzger. "Constraining the Maximum Mass of Neutron Stars From Multi-Messenger Observations of GW170817." In: *Astrophys. J. Lett.* 850.2 (2017), p. L19. DOI: 10.3847/2041-8213/aa991c. arXiv: 1710.05938 [astro-ph.HE].

[215] Andrea Maselli, Leonardo Gualtieri, Paolo Pani, Luigi Stella, and Valeria Ferrari. "Testing Gravity with Quasi Periodic Oscillations from accreting Black Holes: the Case of the Einstein-Dilaton-Gauss-Bonnet Theory." In: *Astrophys. J.* 801.2 (2015), p. 115. DOI: 10.1088/0004-637X/801/2/115. arXiv: 1412.3473 [astro-ph.HE].

[216] M. Masuda and M. Sasaki. "Limits on non-standard forces in the submicrometer range." In: *Phys. Rev. Lett.* 102 (2009), p. 171101. DOI: 10.1103/PhysRevLett.102.171101. arXiv: 0904.1834 [hep-ex].

[217] Norihito Matsunaga and Kazuhiro Yamamoto. "The finite source size effect and the wave optics in gravitational lensing." In: *JCAP* 01 (2006), p. 023. DOI: 10.1088/1475-7516/2006/01/023. arXiv: astro-ph/0601701.

[218] Pawel O. Mazur and Emil Mottola. "Gravitational Condensate Stars: An Alternative to Black Holes." In: *Universe* 9.2 (2023), p. 88. DOI: 10.3390/universe9020088. arXiv: gr-qc/0109035.

[219] Paul J. McMillan. "The mass distribution and gravitational potential of the Milky Way." In: *Mon. Not. Roy. Astron. Soc.* 465.1 (2016), pp. 76–94. DOI: 10.1093/mnras/stw2759. arXiv: 1608.00971 [astro-ph.GA].

[220] Ashish Kumar Meena and J. S. Bagla. "Gravitational lensing of gravitational waves: wave nature and prospects for detection." In: *Mon. Not. Roy. Astron. Soc.* 492.1 (2020), pp. 1127–1134. DOI: 10.1093/mnras/stz3509. arXiv: 1903.11809 [astro-ph.CO].

[221] Ajit Kumar Mehta, Seth Olsen, Digvijay Wadekar, Javier Roulet, Tejaswi Venumadhav, Jonathan Mushkin, Barak Zackay, and Matias Zaldarriaga. "New binary black hole mergers in the LIGO-Virgo O3b data." In: *Phys. Rev. D* 111.2 (2025), p. 024049. DOI: 10.1103/PhysRevD.111.024049. arXiv: 2311.06061 [gr-qc].

[222] Akash K. Mishra, Gregorio Carullo, and Sumanta Chakraborty. "Bounds on tidal charges from gravitational-wave ringdown observations." In: (Nov. 2023). arXiv: 2311.03556 [gr-qc].

[223] Akash K. Mishra, Abhirup Ghosh, and Sumanta Chakraborty. "Constraining extra dimensions using observations of black hole quasi-normal modes." In: *Eur. Phys. J. C* 82.9 (2022), p. 820. DOI: 10.1140/epjc/s10052-022-10788-x. arXiv: 2106.05558 [gr-qc].

[224] Anuj Mishra, Ashish Kumar Meena, Anupreeta More, and Sukanta Bose. "Exploring the Impact of Microlensing on Gravitational Wave Signals: Biases, Population Characteristics, and Prospects for Detection." In: (June 2023). arXiv: 2306.11479 [astro-ph.CO].

[225] Anuj Mishra, Ashish Kumar Meena, Anupreeta More, Sukanta Bose, and Jasjeet Singh Bagla. "Gravitational lensing of gravitational waves: effect of microlens population in lensing galaxies." In: *Mon. Not. Roy. Astron. Soc.* 508.4 (2021), pp. 4869–4886. DOI: 10.1093/mnras/stab2875. arXiv: 2102.03946 [astro-ph.CO].

[226] Charles W. Misner, K. S. Thorne, and J. A. Wheeler. *Gravitation*. San Francisco: W. H. Freeman, 1973. ISBN: 978-0-7167-0344-0, 978-0-691-17779-3.

[227] Soichiro Morisaki. "Accelerating parameter estimation of gravitational waves from compact binary coalescence using adaptive frequency resolutions." In: *Phys. Rev. D* 104.4 (2021), p. 044062. DOI: 10.1103/PhysRevD.104.044062. arXiv: 2104.07813 [gr-qc].

[228] Andrew J. Moylan, David E. McClelland, Susan M. Scott, Antony C. Searle, and G. V. Bicknell. "Numerical wave optics and the lensing of gravitational waves by globular clusters." In: *11th Marcel Grossmann Meeting on General Relativity*. Oct. 2007, pp. 807–823. DOI: 10.1142/9789812834300_0038. arXiv: 0710.3140 [gr-qc].

[229] Sajal Mukherjee and Sumanta Chakraborty. "Horndeski theories confront the Gravity Probe B experiment." In: *Phys. Rev. D* 97.12 (2018), p. 124007. DOI: 10.1103/PhysRevD.97.124007. arXiv: 1712.00562 [gr-qc].

[230] Suvodip Mukherjee, Alex Krolewski, Benjamin D. Wandelt, and Joseph Silk. "Cross-correlating dark sirens and galaxies: constraints on H_0 from GWTC-3 of LIGO-Virgo-KAGRA." In: *Astrophys. J.* 975.2 (2024), p. 189. DOI: 10.3847/1538-4357/ad7d90. arXiv: 2203.03643 [astro-ph.CO].

[231] Suvodip Mukherjee, Benjamin D. Wandelt, Samaya M. Nissanke, and Alessandra Silvestri. "Accurate precision Cosmology with redshift unknown gravitational wave sources." In: *Phys. Rev. D* 103.4 (2021), p. 043520. DOI: 10.1103/PhysRevD.103.043520. arXiv: 2007.02943 [astro-ph.CO].

[232] Suvodip Mukherjee, Benjamin D. Wandelt, and Joseph Silk. "Probing the theory of gravity with gravitational lensing of gravitational waves and galaxy surveys." In: *Mon. Not. Roy. Astron. Soc.* 494.2 (2020), pp. 1956–1970. DOI: 10.1093/mnras/staa827. arXiv: 1908.08951 [astro-ph.CO].

[233] Takahiro T. Nakamura. "Gravitational lensing of gravitational waves from inspiraling binaries by a point mass lens." In: *Phys. Rev. Lett.* 80 (1998), pp. 1138–1141. DOI: 10.1103/PhysRevLett.80.1138.

[234] Takahiro T. Nakamura and Shuji Deguchi. "Wave Optics in Gravitational Lensing." In: *Prog. Theor. Phys. Suppl.* 133 (1999), pp. 137–153. DOI: 10.1143/ptps.133.137.

[235] Ramesh Narayan and Matthias Bartelmann. "Lectures on gravitational lensing." In: *13th Jerusalem Winter School in Theoretical Physics: Formation of Structure in the Universe*. June 1996. arXiv: astro-ph/9606001.

[236] Harsh Narola, Justin Janquart, Leïla Haegel, K. Haris, Otto A. Hannuksela, and Chris Van Den Broeck. "How well can modified gravitational wave propagation be constrained with strong lensing?" In: *Phys. Rev. D* 109.8 (2024), p. 084064. DOI: 10.1103/PhysRevD.109.084064. arXiv: 2308.01709 [gr-qc].

[237] Julio F. Navarro, Carlos S. Frenk, and Simon D. M. White. "The Structure of cold dark matter halos." In: *Astrophys. J.* 462 (1996), pp. 563–575. DOI: 10.1086/177173. arXiv: astro-ph/9508025.

[238] Julio F. Navarro, Carlos S. Frenk, and Simon D. M. White. "A Universal density profile from hierarchical clustering." In: *Astrophys. J.* 490 (1997), pp. 493–508. DOI: 10.1086/304888. arXiv: astro-ph/9611107.

[239] Ken K. Y. Ng, Kaze W. K. Wong, Tom Broadhurst, and Tjonnie G. F. Li. "Precise LIGO Lensing Rate Predictions for Binary Black Holes." In: *Phys. Rev. D* 97.2 (2018), p. 023012. DOI: 10.1103/PhysRevD.97.023012. arXiv: 1703.06319 [astro-ph.CO].

[240] Alex Nitz et al. *gwastro/pycbc: v2.0.4 release of PyCBC*. Version v2.0.4. June 2022. DOI: 10.5281/zenodo.6646669. URL: https://doi.org/10.5281/zenodo.6646669.

[241] Alexander H. Nitz, Sumit Kumar, Yi-Fan Wang, Shilpa Kastha, Shichao Wu, Marlin Schäfer, Rahul Dhurkunde, and Collin D. Capano. "4-OGC: Catalog of Gravitational Waves from Compact Binary Mergers." In: *Astrophys. J.* 946.2 (2023), p. 59. DOI: 10.3847/1538-4357/aca591. arXiv: 2112.06878 [astro-ph.HE].

[242] Masamune Oguri. "Effect of gravitational lensing on the distribution of gravitational waves from distant binary black hole mergers." In: *Mon. Not. Roy. Astron. Soc.* 480.3 (2018), pp. 3842–3855. DOI: 10.1093/mnras/sty2145. arXiv: 1807.02584 [astro-ph.CO].

[243] Masamune Oguri and Ryuichi Takahashi. "Probing Dark Low-mass Halos and Primordial Black Holes with Frequency-dependent Gravitational Lensing Dispersions of Gravitational Waves." In: *Astrophys. J.* 901.1 (2020), p. 58. DOI: 10.3847/1538-4357/abafab. arXiv: 2007.01936 [astro-ph.CO].

[244] Seth Olsen, Tejaswi Venumadhav, Jonathan Mushkin, Javier Roulet, Barak Zackay, and Matias Zaldarriaga. "New binary black hole mergers in the LIGO-Virgo O3a data." In: *Phys. Rev. D* 106.4 (2022), p. 043009. DOI: 10.1103/PhysRevD.106.043009. arXiv: 2201.02252 [astro-ph.HE].

[245] Giulia Pagano, Otto A. Hannuksela, and Tjonnie G. F. Li. "lensingGW: a Python package for lensing of gravitational waves." In: *Astron. Astrophys.* 643 (2020), A167. DOI: 10.1051/0004-6361/202038730. arXiv: 2006.12879 [astro-ph.CO].

[246] Kris Pardo, Maya Fishbach, Daniel E. Holz, and David N. Spergel. "Limits on the number of spacetime dimensions from GW170817." In: *JCAP* 07 (2018), p. 048. DOI: 10.1088/1475-7516/2018/07/048. arXiv: 1801.08160 [gr-qc].

[247] P. C. Peters. "Index of refraction for scalar, electromagnetic, and gravitational waves in weak gravitational fields." In: *Phys. Rev. D* 9 (1974), pp. 2207–2218. DOI: 10.1103/PhysRevD.9.2207.

[248] P. C. Peters and J. Mathews. "Gravitational radiation from point masses in a Keplerian orbit." In: *Phys. Rev.* 131 (1963), pp. 435–439. DOI: 10.1103/PhysRev.131.435.

[249] E. Pian et al. "Spectroscopic identification of r-process nucleosynthesis in a double neutron star merger." In: *Nature* 551 (2017), pp. 67–70. DOI: 10.1038/nature24298. arXiv: 1710.05858 [astro-ph.HE].

[250] Mauro Pieroni, Angelo Ricciardone, and Enrico Barausse. "Detectability and parameter estimation of stellar origin black hole binaries with next generation gravitational wave detectors." In: *Sci. Rep.* 12.1 (2022), p. 17940. DOI: 10.1038/s41598-022-19540-7. arXiv: 2203.12586 [astro-ph.CO].

[251] D. Marín Pina, M. Orselli, and D. Pica. "Event horizon of a charged black hole binary merger." In: *Phys. Rev. D* 106.8 (2022), p. 084012. DOI: 10.1103/PhysRevD.106.084012. arXiv: 2204.08841 [gr-qc].

[252] Cailin Plunkett, Sophie Hourihane, and Katerina Chatziioannou. "Concurrent estimation of noise and compact-binary signal parameters in gravitational-wave data." In: *Phys. Rev. D* 106.10 (2022), p. 104021. DOI: 10.1103/PhysRevD.106.104021. arXiv: 2208.02291 [gr-qc].

[253] Geraint Pratten et al. "Computationally efficient models for the dominant and subdominant harmonic modes of precessing binary black holes." In: *Phys. Rev. D* 103.10 (2021), p. 104056. DOI: 10.1103/PhysRevD.103.104056. arXiv: 2004.06503 [gr-qc].

[254] M. Punturo et al. "The Einstein Telescope: A third-generation gravitational wave observatory." In: *Class. Quant. Grav.* 27 (2010). Ed. by Fulvio Ricci, p. 194002. DOI: 10.1088/0264-9381/27/19/194002.

[255] Michael Pürrer. "Frequency domain reduced order models for gravitational waves from aligned-spin compact binaries." In: *Class. Quant. Grav.* 31.19 (2014), p. 195010. DOI: 10.1088/0264-9381/31/19/195010. arXiv: 1402.4146 [gr-qc].

[256] Michael Pürrer. "Frequency domain reduced order model of aligned-spin effective-one-body waveforms with generic mass-ratios and spins." In: *Phys. Rev. D* 93.6 (2016), p. 064041. DOI: 10.1103/PhysRevD.93.064041. arXiv: 1512.02248 [gr-qc].

[257] Michael Pürrer and Carl-Johan Haster. "Gravitational waveform accuracy requirements for future ground-based detectors." In: *Phys. Rev. Res.* 2.2 (2020), p. 023151. DOI: 10.1103/PhysRevResearch.2.023151. arXiv: 1912.10055 [gr-qc].

[258] S. Refsdal. "On the possibility of determining Hubble's parameter and the masses of galaxies from the gravitational lens effect." In: *Mon. Not. Roy. Astron. Soc.* 128 (1964), p. 307.

[259] Katie Rink, Ritesh Bachhar, Tousif Islam, Nur E. M. Rifat, Kevin Gonzalez-Quesada, Scott E. Field, Gaurav Khanna, Scott A. Hughes, and Vijay Varma. "Gravitational wave surrogate model for spinning, intermediate mass ratio binaries based on perturbation theory and numerical relativity." In: *Phys. Rev. D* 110.12 (2024), p. 124069. DOI: 10.1103/PhysRevD.110.124069. arXiv: 2407.18319 [gr-qc].

[260] Leszek Roszkowski, Enrico Maria Sessolo, and Sebastian Trojanowski. "WIMP dark matter candidates and searches—current status and future prospects." In: *Rept. Prog. Phys.* 81.6 (2018), p. 066201. DOI: 10.1088/1361-6633/aab913. arXiv: 1707.06277 [hep-ph].

[261] M. Saleem et al. "The science case for LIGO-India." In: *Class. Quant. Grav.* 39.2 (2022), p. 025004. DOI: 10.1088/1361-6382/ac3b99. arXiv: 2105.01716 [gr-qc].

[262] Misao Sasaki, Teruaki Suyama, Takahiro Tanaka, and Shuichiro Yokoyama. "Primordial Black Hole Scenario for the Gravitational-Wave Event GW150914." In: *Phys. Rev. Lett.* 117.6 (2016). [Erratum: Phys.Rev.Lett. 121, 059901 (2018)], p. 061101. DOI: 10.1103/PhysRevLett.117.061101. arXiv: 1603.08338 [astro-ph.CO].

[263] B. S. Sathyaprakash and B. F. Schutz. "Physics, Astrophysics and Cosmology with Gravitational Waves." In: *Living Rev. Rel.* 12 (2009), p. 2. DOI: 10.12942/lrr-2009-2. arXiv: 0903.0338 [gr-qc].

[264] B. S. Sathyaprakash et al. "Extreme Gravity and Fundamental Physics." In: (Mar. 2019). arXiv: 1903.09221 [astro-ph.HE].

[265] Peter Schneider, Jürgen Ehlers, and Emilio E. Falco. *Gravitational Lenses*. Astronomy and Astrophysics Library. Springer, 1992. ISBN: 978-3-540-66506-9, 978-3-662-03758-4. DOI: 10.1007/978-3-662-03758-4.

[266] Bernard F. Schutz. "Determining the Hubble Constant from Gravitational Wave Observations." In: *Nature* 323 (1986), pp. 310–311. DOI: 10.1038/323310a0.

[267] Yannis K. Semertzidis and SungWoo Youn. "Axion dark matter: How to see it?" In: *Sci. Adv.* 8.8 (2022), abm9928. DOI: 10.1126/sciadv.abm9928. arXiv: 2104.14831 [hep-ph].

[268] Eungwang Seo, Xikai Shan, Justin Janquart, Otto A. Hannuksela, Martin A. Hendry, and Bin Hu. "Residual test to search for microlensing signatures in strongly lensed gravitational wave signals." In: (Mar. 2025). arXiv: 2503.02186 [gr-qc].

[269] Pau Amaro Seoane et al. "Astrophysics with the Laser Interferometer Space Antenna." In: *Living Rev. Rel.* 26.1 (2023), p. 2. DOI: 10.1007/s41114-022-00041-y. arXiv: 2203.06016 [gr-qc].

[270] Xikai Shan, Guoliang Li, Xuechun Chen, Wenwen Zheng, and Wen Zhao. "Wave effect of gravitational waves intersected with a microlens field: A new algorithm and supplementary study." In: *Sci. China Phys. Mech. Astron.* 66.3 (2023), p. 239511. DOI: 10.1007/s11433-022-1985-3. arXiv: 2208.13566 [astro-ph.CO].

[271] Tetsuya Shiromizu, Kei-ichi Maeda, and Misao Sasaki. "The Einstein equation on the 3-brane world." In: *Phys. Rev. D* 62 (2000), p. 024012. DOI: 10.1103/PhysRevD.62.024012. arXiv: gr-qc/9910076.

[272] Mukesh Kumar Singh, Shasvath J. Kapadia, Soummyadip Basak, Parameswaran Ajith, and Shriharsh P. Tendulkar. "Associating fast radio bursts with compact binary mergers via gravitational lensing." In: *Mon. Not. Roy. Astron. Soc.* 527.2 (2023), pp. 4234–4243. DOI: 10.1093/mnras/stad3376. arXiv: 2304.02879 [astro-ph.HE].

[273] M. Soares-Santos et al. "The Electromagnetic Counterpart of the Binary Neutron Star Merger LIGO/Virgo GW170817. I. Discovery of the Optical Counterpart Using the Dark Energy Camera." In: *Astrophys. J. Lett.* 848.2 (2017), p. L16. DOI: 10.3847/2041-8213/aa9059. arXiv: 1710.05459 [astro-ph.HE].

[274] Yoshiaki Sofue and Vera Rubin. "Rotation curves of spiral galaxies." In: *Ann. Rev. Astron. Astrophys.* 39 (2001), pp. 137–174. DOI: 10.1146/annurev.astro.39.1.137. arXiv: astro-ph/0010594.

[275] Volker Springel et al. "Simulating the joint evolution of quasars, galaxies and their large-scale distribution." In: *Nature* 435 (2005), pp. 629–636. DOI: 10.1038/nature03597. arXiv: astro-ph/0504097.

[276] Zdeněk Stuchlík and Andrea Kotrlová. "Orbital resonances in discs around braneworld Kerr black holes." In: *Gen. Rel. Grav.* 41 (2009), pp. 1305–1343. DOI: 10.1007/s10714-008-0709-2. arXiv: 0812.5066 [astro-ph].

[277] A. O. Sushkov, W. J. Kim, D. A. R. Dalvit, and S. K. Lamoreaux. "New Experimental Limits on Non-Newtonian Forces in the Micrometer Range." In: *Phys. Rev. Lett.* 107 (2011), p. 171101. DOI: 10.1103/PhysRevLett.107.171101. arXiv: 1108.2547 [quant-ph].

[278] Ryuichi Takahashi. "Quasigeometrical optics approximation in gravitational lensing." In: *Astron. Astrophys.* 423 (2004), pp. 787–792. DOI: 10.1051/0004-6361:20040212. arXiv: astro-ph/0402165.

[279] Ryuichi Takahashi and Takashi Nakamura. "Wave effects in gravitational lensing of gravitational waves from chirping binaries." In: *Astrophys. J.* 595 (2003), pp. 1039–1051. DOI: 10.1086/377430. arXiv: astro-ph/0305055.

[280] Giovanni Tambalo, Miguel Zumalacárregui, Liang Dai, and Mark Ho-Yeuk Cheung. "Lensing of gravitational waves: Efficient wave-optics methods and validation with symmetric lenses." In: *Phys. Rev. D* 108.4 (2023), p. 043527. DOI: 10.1103/PhysRevD.108.043527. arXiv: 2210.05658 [gr-qc].

[281] J. H. Taylor and J. M. Weisberg. "A new test of general relativity - Gravitational radiation and the binary pulsar PSR 1913+16." In: *The Astrophysical Journal* 253 (Feb. 1982), p. 908. ISSN: 1538-4357. DOI: 10.1086/159690. URL: http://dx.doi.org/10.1086/159690.

[282] Max Tegmark et al. "Cosmological parameters from SDSS and WMAP." In: *Phys. Rev. D* 69 (2004), p. 103501. DOI: 10.1103/PhysRevD.69.103501. arXiv: astro-ph/0310723.

[283] Rodrigo Tenorio, David Keitel, and Alicia M. Sintes. "Search Methods for Continuous Gravitational-Wave Signals from Unknown Sources in the Advanced-Detector Era." In: *Universe* 7.12 (2021), p. 474. DOI: 10.3390/universe7120474. arXiv: 2111.12575 [gr-qc].

[284] Lucy M. Thomas, Geraint Pratten, and Patricia Schmidt. "Accelerating multimodal gravitational waveforms from precessing compact binaries with artificial neural networks." In: *Phys. Rev. D* 106.10 (2022), p. 104029. DOI: 10.1103/PhysRevD.106.104029. arXiv: 2205.14066 [gr-qc].

[285] Manuel Tiglio and Aarón Villanueva. "Reduced order and surrogate models for gravitational waves." In: *Living Rev. Rel.* 25.1 (2022), p. 2. DOI: 10.1007/s41114-022-00035-w. arXiv: 2101.11608 [gr-qc].

[286] Bobir Toshmatov, Zdeněk Stuchlík, Jan Schee, and Bobomurat Ahmedov. "Quasinormal frequencies of black hole in the braneworld." In: *Phys. Rev. D* 93.12 (2016), p. 124017. DOI: 10.1103/PhysRevD.93.124017. arXiv: 1605.02058 [gr-qc].

[287] Tommaso Treu. "Strong Lensing by Galaxies." In: *Annual Review of Astronomy and Astrophysics* 48.1 (Aug. 2010), pp. 87–125. ISSN: 1545-4282. DOI: 10.1146/annurev-astro-081309-130924. URL: http://dx.doi.org/10.1146/annurev-astro-081309-130924.

[288] Tommaso Treu, Sherry H. Suyu, and Philip J. Marshall. "Strong lensing time-delay cosmography in the 2020s." In: *Astron. Astrophys. Rev.* 30.1 (2022), p. 8. DOI: 10.1007/s00159-022-00145-y. arXiv: 2210.15794 [astro-ph.CO].

[289] Andrew Ulmer and Jeremy Goodman. "Femtolensing: Beyond the semiclassical approximation." In: *Astrophys. J.* 442 (1995), p. 67. DOI: 10.1086/175422. arXiv: astro-ph/9406042.

[290] C. S. Unnikrishnan. "IndIGO and LIGO-India: Scope and plans for gravitational wave research and precision metrology in India." In: *Int. J. Mod. Phys. D* 22 (2013), p. 1341010. DOI: 10.1142/S0218271813410101. arXiv: 1510.06059 [physics.ins-det].

[291] Sunny Vagnozzi et al. "Horizon-scale tests of gravity theories and fundamental physics from the Event Horizon Telescope image of Sagittarius A." In: *Class. Quant. Grav.* 40.16 (2023), p. 165007. DOI: 10.1088/1361-6382/acd97b. arXiv: 2205.07787 [gr-qc].

[292] Stefano Valenti, David J. Sand, Sheng Yang, Enrico Cappellaro, Leonardo Tartaglia, Alessandra Corsi, Saurabh W. Jha, Daniel E. Reichart, Joshua Haislip, and Vladimir Kouprianov. "The discovery of the electromagnetic counterpart of GW170817: kilonova AT 2017gfo/DLT17ck." In: *Astrophys. J. Lett.* 848.2 (2017), p. L24. DOI: 10.3847/2041-8213/aa8edf. arXiv: 1710.05854 [astro-ph.HE].

[293] Michele Vallisneri. "Use and abuse of the Fisher information matrix in the assessment of gravitational-wave parameter-estimation prospects." In: *Phys. Rev. D* 77 (2008), p. 042001. DOI: 10.1103/PhysRevD.77.042001. arXiv: gr-qc/0703086.

[294] Michele Vallisneri. "Testing general relativity with gravitational waves: a reality check." In: *Phys. Rev. D* 86 (2012), p. 082001. DOI: 10.1103/PhysRevD.86.082001. arXiv: 1207.4759 [gr-qc].

[295] Vijay Varma, Scott E. Field, Mark A. Scheel, Jonathan Blackman, Davide Gerosa, Leo C. Stein, Lawrence E. Kidder, and Harald P. Pfeiffer. "Surrogate models for precessing binary black hole simulations with unequal masses." In: *Phys. Rev. Research.* 1 (2019), p. 033015. DOI: 10.1103/PhysRevResearch.1.033015. arXiv: 1905.09300 [gr-qc].

[296] Vijay Varma, Davide Gerosa, Leo C. Stein, François Hébert, and Hao Zhang. "High-accuracy mass, spin, and recoil predictions of generic black-hole merger remnants." In: *Phys. Rev. Lett.* 122.1 (2019), p. 011101. DOI: 10.1103/PhysRevLett.122.011101. arXiv: 1809.09125 [gr-qc].

[297] Pablo Villanueva-Domingo, Olga Mena, and Sergio Palomares-Ruiz. "A brief review on primordial black holes as dark matter." In: *Front. Astron. Space Sci.* 8 (2021), p. 87. DOI: 10.3389/fspas.2021.681084. arXiv: 2103.12087 [astro-ph.CO].

[298] Hector Villarrubia-Rojo, Stefano Savastano, Miguel Zumalacárregui, Lyla Choi, Srashti Goyal, Liang Dai, and Giovanni Tambalo. "Gravitational lensing of waves: Novel methods for wave-optics phenomena." In: *Phys. Rev. D* 111.10 (2025), p. 103539. DOI: 10.1103/PhysRevD.111.103539. arXiv: 2409.04606 [gr-qc].

[299] C. V. Vishveshwara. "Scattering of Gravitational Radiation by a Schwarzschild Black-hole." In: *Nature* 227 (1970), pp. 936–938. DOI: 10.1038/227936a0.

[300] Digvijay Wadekar, Javier Roulet, Tejaswi Venumadhav, Ajit Kumar Mehta, Barak Zackay, Jonathan Mushkin, Seth Olsen, and Matias Zaldarriaga. "New black hole mergers in the LIGO-Virgo O3 data from a gravitational wave search including higher-order harmonics." In: (Dec. 2023). arXiv: 2312.06631 [gr-qc].

[301] Yun Wang, Albert Stebbins, and Edwin L. Turner. "Gravitational lensing of gravitational waves from merging neutron star binaries." In: *Phys. Rev. Lett.* 77 (1996), pp. 2875–2878. DOI: 10.1103/PhysRevLett.77.2875. arXiv: astro-ph/9605140.

[302] Darach Watson et al. "Identification of strontium in the merger of two neutron stars." In: *Nature* 574.7779 (2019), pp. 497–500. DOI: 10.1038/s41586-019-1676-3. arXiv: 1910.10510 [astro-ph.HE].

[303] J. Weber. "Detection and Generation of Gravitational Waves." In: *Phys. Rev.* 117 (1960), pp. 306–313. DOI: 10.1103/PhysRev.117.306.

[304] Steven Weinberg. *Gravitation and Cosmology: Principles and Applications of the General Theory of Relativity*. New York: John Wiley and Sons, 1972. ISBN: 978-0-471-92567-5, 978-0-471-92567-5.

[305] Joel M. Weisberg and Joseph H. Taylor. "Relativistic binary pulsar B1913+16: Thirty years of observations and analysis." In: *ASP Conf. Ser.* 328 (2005), p. 25. arXiv: astro-ph/0407149.

[306] K. Wette et al. "Searching for gravitational waves from Cassiopeia A with LIGO." In: *Class. Quant. Grav.* 25 (2008). Ed. by Susan M. Scott and David E. McClelland, p. 235011. DOI: 10.1088/0264-9381/25/23/235011. arXiv: 0802.3332 [gr-qc].

[307] A. Renske A. C. Wierda, Ewoud Wempe, Otto A. Hannuksela, L. éon V. E. Koopmans, and Chris Van Den Broeck. "Beyond the Detector Horizon: Forecasting Gravitational-Wave Strong Lensing." In: *Astrophys. J.* 921.2 (2021), p. 154. DOI: 10.3847/1538-4357/ac1bb4. arXiv: 2106.06303 [astro-ph.HE].

[308] Mick Wright and Martin Hendry. "Gravelamps: Gravitational Wave Lensing Mass Profile Model Selection." In: (Dec. 2021). DOI: 10.3847/1538-4357/ac7ec2. arXiv: 2112.07012 [astro-ph.HE].

[309] Fei Xu, Jose Maria Ezquiaga, and Daniel E. Holz. "Please Repeat: Strong Lensing of Gravitational Waves as a Probe of Compact Binary and Galaxy Populations." In: *Astrophys. J.* 929.1 (2022), p. 9. DOI: 10.3847/1538-4357/ac58f8. arXiv: 2105.14390 [astro-ph.CO].

[310] Shan-Qing Yang, Bi-Fu Zhan, Qing-Lan Wang, Cheng-Gang Shao, Liang-Cheng Tu, Wen-Hai Tan, and Jun Luo. "Test of the Gravitational Inverse Square Law at Millimeter Ranges." In: *Phys. Rev. Lett.* 108 (2012), p. 081101. DOI: 10.1103/PhysRevLett.108.081101.

[311] Hirotaka Yarimoto and Masamune Oguri. "Born approximation in wave optics of gravitational lensing revisited." In: *Phys. Rev. D* 111.8 (2025), p. 083541. DOI: 10.1103/PhysRevD.111.083541. arXiv: 2412.07272 [astro-ph.CO].

[312] Jooheon Yoo, Vijay Varma, Matthew Giesler, Mark A. Scheel, Carl-Johan Haster, Harald P. Pfeiffer, Lawrence E. Kidder, and Michael Boyle. "Targeted large mass ratio numerical relativity surrogate waveform model for GW190814." In: *Phys. Rev. D* 106.4 (2022), p. 044001. DOI: 10.1103/PhysRevD.106.044001. arXiv: 2203.10109 [gr-qc].

[313] Jooheon Yoo et al. "Numerical relativity surrogate model with memory effects and post-Newtonian hybridization." In: *Phys. Rev. D* 108.6 (2023), p. 064027. DOI: 10.1103/PhysRevD.108.064027. arXiv: 2306.03148 [gr-qc].

[314] Nicolás Yunes and Xavier Siemens. "Gravitational-Wave Tests of General Relativity with Ground-Based Detectors and Pulsar Timing-Arrays." In: *Living Rev. Rel.* 16 (2013), p. 9. DOI: 10.12942/lrr-2013-9. arXiv: 1304.3473 [gr-qc].

[315] Barak Zackay, Liang Dai, and Tejaswi Venumadhav. "Relative Binning and Fast Likelihood Evaluation for Gravitational Wave Parameter Estimation." In: (June 2018). arXiv: 1806.08792 [astro-ph.IM].

[316] Mark Zimmermann and Eugene Szedenits. "Gravitational waves from rotating and precessing rigid bodies: Simple models and applications to pulsars." In: *Phys. Rev. D* 20 (2 1979), pp. 351–355. DOI: 10.1103/PhysRevD.20.351. URL: https://link.aps.org/doi/10.1103/PhysRevD.20.351.